Annual Report on Major Results and Progress of Fusion Research and Development Directorate of JAEA from April 1, 2006 to March 31, 2007

Fusion Research and Development Directorate

Japan Atomic Energy Agency
Naka-shi, Ibaraki-ken

(Received June 25, 2008)

This annual report provides an overview of major results and progress on research and development (R&D) activities at Fusion Research and Development Directorate of Japan Atomic Energy Agency (JAEA) from April 1, 2006 to March 31, 2007, including those performed in collaboration with other research establishments of JAEA, research institutes, and universities.

In JT-60, as a result of ferritic steel tiles (FSTs) installation to reduce the troidal field ripple and the application of the real time current profile control, high boot strap current fraction (~0.7) has successfully been sustained about 8 s. In addition, the conceptual design of JT-60SA, which was placed as a combined project of JA-EU Satellite Tokamak Programme under the Broader Approach Programme and JAEA's programme for national use, was progressed.

In theoretical and analytical researches, studies on ITB events and their triggers, plasma shape effect on edge stability and driven magnetic island evolution in rotating plasmas were progressed. In the NEXT project, computer simulations of the plasma turbulence were progressed.

In fusion reactor technologies, R&Ds for ITER and fusion DEMO plants have been carried out. For ITER, a steady state operation of the 170GHz gyrotoron up to 10min with 0.82MW was demonstrated. Also current density of the neutral beam injector has been extended to 146A/m^2 at 0.84MeV. In the ITER Test Blanket Module (TBM), designs and R&Ds of Water and Helium Cooled Solid Breeder TBMs including tritium breeder/multiplier materials were progressed. Tritium processing technology for breeding blankets and neutronics integral experiments with a blanket mockup were also progressed. For ITER and DEMO blankets, studies on neutron irradiation effects and ion irradiation effects on F82H steel characteristics were continued using HFIR, TIARA and so on. In the IFMIF program, transitional activities to EVEDA were continued.

In the ITER Program, under the framework of the ITER Transitional Arrangements, the Design and R&D Tasks (ITA Tasks) have been carried out by the Participant Teams along the work plan. In FY 2006, JAEA has performed seventy-four ITA Tasks and has completed fifty-nine Tasks. In addition, the provisional activity for the establishment of Japan Domestic Agency has been performed. For “Broader Approach (BA)”, the site of BA activity has been decided in Rokkasho (the ex-ITER candidate site).

Finally, in fusion reactor design studies, a reactor concept of SlimCS was progressed from the view point of maintenance scheme.

Keywords; Fusion Research, Fusion Technology, JT-60, JT-60SA, ITER, Broader Approach, IFMIF, Fusion Power, DEMO, Fusion Reactor

---

Editors: Suzuki, S., Ishii, Y., Sukegawa, A., Iwai, Y., Nakamura, H., Sugie, T.

Contents

I. JT-60 Program

1. Experimental Results and Analyses

The JT-60U tokamak project has addressed major physics and technological issues for burning plasma development in ITER and for steady-state high-b operation development towards JT-60SA and DEMO reactors. The fusion research has to establish an efficient control of the self-regulating plasmas for achieving a high integrated performance. Toward this goal, in particular, the mechanisms determining the plasma rotation profile and effects of the rotation on transport and stability are the central research issues. Reduction of the toroidal field ripple by installing ferritic steel tiles in JT-60U (installed in 2005) reduced the fast ion losses and resultant counter plasma rotation drive. By combining this newly achieved freedom of rotation with co-, counter- and perpendicular NBs, JT-60U has been promoting an integrated research project focusing on the plasma rotation covering transport, stability, pedestal, and steady state operation.

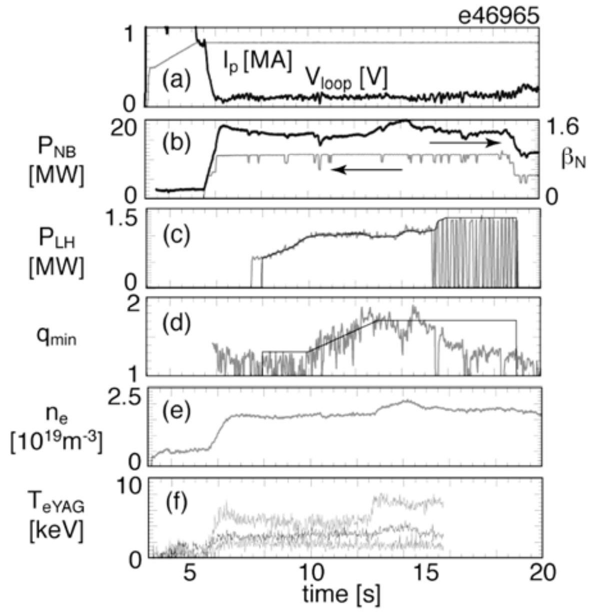

Fig.I.1.1-1 Typical waveforms of the real time q_{min} control. in the fourth box (d), temporal evolutions of the reference and the measured q_{min} are indicated. As shown, q_{min} is well controlled up to ~16 s when the notching of the LH power started. It is seen in the temporal evolution of T_e that T_e near the center increased rapidly suggesting formation of ITB.

1.1 Extended Plasma Regimes

Application of the real time current profile control was extended to higher β_N plasmas. Control of the minimum in the q profile (q_{min}) was successfully demonstrated [1.1-1]. Pursue of a plasma with high bootstrap current fraction (f_{BS}) had been continued [1.1-2, 1.1-3]. Duration of sustainment of high f_{BS}, about 70%, was extended to about 8 s. A plasma sustained fully by the bootstrap current was confirmed by the loop voltage profile analysis. Current ramp up solely by the bootstrap current was also demonstrated.

1.1.1 Real Time Current Profile Control

Real time current profile control by using both real time evaluation of the q profile from the MSE diagnostics and real time control on the LHCD system had been extended to higher performance plasmas. It was demonstrated that in a plasma with higher β_N. The control was applied to high-β_p mode plasma (I_p = 0.8 MA, B_t = 2.5 T, q_{95} = 5.9) having initial q_{min} of about 1.2. The plasma having the normalized beta β_N of about 1.3-1.6 was by 11 MW of NB heating. Real time control of the q_{min} was successfully demonstrated in the plasma as shown in Fig.I.1.1-1. The reference q_{min} was increased from 1.3 to 1.7 taking 3 s, the actual q_{min} followed the reference and reached 1.7. When the q_{min} was controlled at the fixed value of 1.7, the central electron temperature (r/a < 0.3), the line averaged electron density and stored energy started increasing, which shows formation of an internal transport barrier (ITB). The application of the real-time control changed the q profile and lead to the change in confinement. Due to the resulting increase in the electron temperature and the pressure, central Ohmic current and bootstrap current increased, leading to decrease in q_{min}. However, the decrease in q_{min} was recovered by the increase in P_{LH} by the control, here P_{LH} is the LH power. The real-time q_{min} control was demonstrated in such a self-regulated plasma, where the pressure and the current profiles are linked through the bootstrap current.

1.1.2 Off-axis NBCD

Capability of off-axis NBCD had been assessed, in plasmas with I_p = 0.8 MA and 1.2 MA at B_t = 3.8 T [1.1-1]. In both cases, a well localized NB driven current profile was confirmed for the first time. The total amount of the driven current estimated from the MSE measurement almost agreed with calculations by the ACCOME code in both cases. However, the measured j_{NB} (ρ) was more off-axis that that in the calculations.

1.1.3 Plasmas with Very High Bootstrap Current Fraction

In a previous campaign, sustainment of high f_{BS} of 75% for 7.4 s was demonstrated [1.1-4]. It had been tried to extend this period, and finally duration of high f_{BS} sustainment, though f_{BS} is a litter lower in this case (~70%), was extended to 8 s. Furthermore, a self-sustained state driven by the bootstrap current was achieved. A loop voltage profile of nearly zero or slightly negative across the cross section was maintained for 0.2 s with a constant OH primary current. In this discharge, of the total I_p of 543 kA, the calculated beam driven current was -35 kA and the inductive current was -5 kA. In the newly implemented constant plasma surface flux feedback mode, which ensures no net flux input to the plasma, a steady I_p ramp-up at a rate of 10 kA/s was achieved for 0.5 s. These results provide the evidence of bootstrap overdrive.

References

1.1-1 Suzuki, T., *et al.*, *Proc. 21st Int. Conf. on Fusion Energy 2006 (Chengdu, 2006)* CD-ROM file EX/6-4.

1.1-2 Sakamoto, Y., *et al.*, *Proc. 21st Int. Conf. on Fusion Energy 2006 (Chengdu, 2006)* CD-ROM file EX/P1-10.

1.1-3 Takase, Y., *et al.*, *Proc. 21st Int. Conf. on Fusion Energy 2006 (Chengdu, 2006)* CD-ROM file EX/1-4.

1.1-4 Sakamoto, Y., *et al.*, *Nucl. Fusion* **45,** 574 (2005).

1.2 Heat, Particle and Rotation Transport

1.2.1 Controllability of large bootstrap current fraction plasmas

The large bootstrap current fraction of $f_{BS} \geq 0.7$ is required in a steady-state tokamak fusion reactor to reduce a circulating power for non-inductive current drivers. In the large f_{BS} plasma, the current and pressure profiles are strongly linked to each other. A control scheme for such self-regulating large f_{BS} plasmas with the strong parameter linkage has been developed in the reversed shear (RS) plasmas with $f_{BS} \sim 0.7$ [1.2-1]. The large f_{BS} RS plasma was frequently terminated by the disruption or the collapse when the minimum value of the safety factor (q_{min}) passed through integer values during the current profile relaxation towards a steady-state profile. In order to avoid the disruption or the collapse, the pressure gradient at the internal transport barrier (ITB) should decrease at $q_{min} \sim$ integer. It has been demonstrated that the steep pressure gradient at the ITB can be reduced by the control of the toroidal rotation profile [1.2-2]. However, it was difficult to adjust the timing of the rotation control using the pre-programmed setting, because the timing of $q_{min} \sim$ integer depends on the time evolution of the plasma current profile. The time evolution of the plasma current profile is affected by an initial current profile, an onset of ITB formation, an ITB structure and so on. In order to establish the effective pressure profile control at $q_{min} \sim$ integer through the rotation control, a real time control logic was newly installed based on the real time calculation of q_{min} using MSE diagnostics [1.2-3]. In this logic, the counter (ctr) neutral beam injection (NBI) is stopped automatically when q_{min} is close to the integer value.

In order to optimize the control logic, the response of q_{min} to the change in the ion temperature gradient at the ITB was first investigated. The strong response was observed in the large f_{BS} (~ 0.7) plasma compared with the $f_{BS} \sim 0.5$ plasma when the ion temperature gradient at the ITB was changed by controlling the toroidal rotation as shown in Fig. I.1.2-1. The strong response

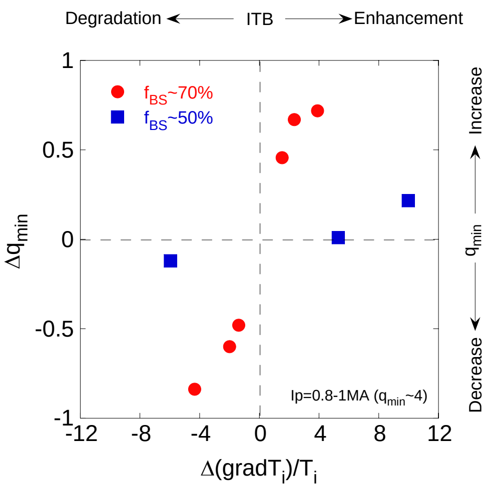

Fig. I.1.2-1 Change in q_{min} plotted against change in inverse scale length of ion temperature at ITB. Closed circles denote in the case of $f_{BS} \sim 0.7$. Closed squares denote in the case of $f_{BS} \sim 0.5$.

indicates the strong linkage between the pressure and current profiles in the large f_{BS} plasma. Based on this result, the duration for the stop of ctr-NBI was set to be 0.8 s. Note that q_{min} was not measured during the stop of the ctr-NBI, because the ctr-NBI is diagnostic beam for MSE. Therefore, the duration was set as a pre-programmed value. In the case of the long duration, the degraded ITB was not recovered due to the large change of current profile even when the ctr-NBI was injected again after q_{min} passed through the integer value. In the case of the short duration, the changes in the pressure gradient at the ITB and the current profile were not sufficient to avoid the disruption and the collapse.

By optimizing this new real time control scheme, the pressure profile was controlled with the good reproducibility just before q_{min} ~ integer in which the disruption or the collapse occurred frequently. As the result, the weak RS plasma with f_{BS} ~ 0.7 was successfully sustained for ~ 8 s, which corresponds to $3\tau_R$. Here, τ_R is the current diffusion time. Typical waveforms of the long sustainment of the RS plasma with the large f_{BS} using the newly installed real time control logic are shown in Fig. I.1.2-2 (a), where $I_p = 0.8$ MA, $B_T = 3.4$ T, q_{95} ~ 8.5, $\kappa = 1.6$, $\delta = 0.4$. Using the feedback control of the stored energy by the perpendicular NBIs, β_N ~ 1.5 (β_p ~ 2.1) was maintained. In this plasma, ctr-NBI was turned off for 0.8 s when q_{min} was in the range of 3.7 - 4.1 as setting. The value of q_{min} decreased in time and was below 4.1 at t ~ 7 s as shown in this figure. Then ctr-NBI turned off for 0.8 s. During this phase, the toroidal rotation started to change towards the co-direction, and then the electron pressure at the ITB was reduced and recovered as shown in the figure. Behavior of the ion temperature was similar to that of the electron pressure profile. The reduction of the pressure gradient at the ITB in this period led to the avoidance of the collapse at q_{min} ~ 4. High confinement of H_{89} ~ 2.6 (HH_{98y2} ~ 1.8) was obtained in this plasma, and f_{BS} ~ 0.7 was sustained for ~ 8 s.

In the later 3 s, the q profile became flat, as shown in figure I.1.2-2 (b), with keeping the good ITB and seems to be almost unchangeable. The temporal evolution of the radial profile of the time averaged internal loop voltage is shown in Fig. I.1.2-2 (c), which was evaluated from the equilibrium reconstruction using the MSE measurement. The profile of the internal loop voltage was flattened in time, indicating the plasma approached the stationary condition. However, the electron pressure continued to increase slightly at the core region and then collapse occurred at t ~ 13.3 s.

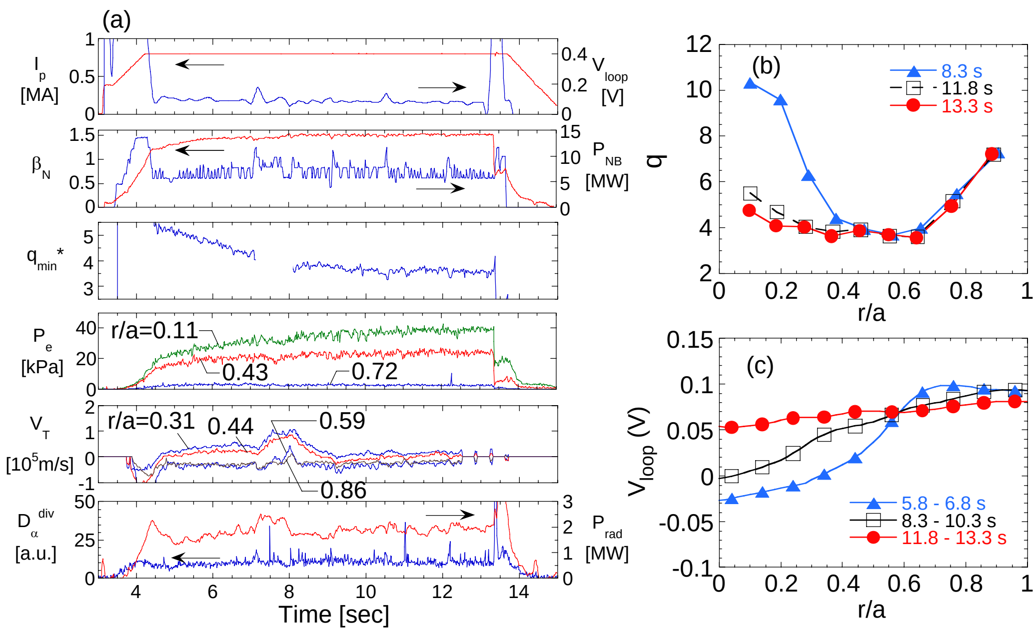

Fig. I.1.2-2. Typical discharge of long sustainment of reversed shear plasma with large f_{BS} (~ 0.7) using newly installed real time control logic. (a) Waveforms of the discharge. First panel : plasma current (I_p) and loop voltage (V_{loop}). Second panel : normalized beta (β_N) and neutral beam heating power (P_{NB}). Third panel : q_{min} estimated in real-time. Fourth panel : electron pressure at r/a = 0.11, 0.43 and 0.72. Fifth panel : toroidal rotation at r/a = 0.31, 0.4, 0.59 and 0.86. Bottom panel : D_α emission intensity from the divertor (D_α^{div}) and radiation loss (P_{rad}). (b) Temporal evolution of q profile. (c) Temporal evolution of inductive field profile.

Since the value of q_{min} was just above 3.6, this collapse can be attributed to the evolution of pressure profile. Effective pressure profile control is required instead of the global parameter control such as the control of the stored energy even after the current profile approaches to the steady-state so as to demonstrate the long steady sustainment of high f_{BS} plasmas.

1.2.2 Observation on Decoupling of Electron Heat Transport and Long-Spatial-Scale Density Fluctuations in Reversed Shear Plasma

In the reversed shear plasma, the suppression of long-spatial-scale density fluctuations with a wave number of the order of 1 cm^{-1} was observed in the ITB a region, after a cold pulse was induced by the shallow pellet injection at the plasma edge. Particle and power balance analysis with fully recovered temperature profiles after the cold pulse propagation indicated that the particle and the ion heat transport is coupled with the long-spatial-scale density fluctuations, while the electron heat transport is not coupled with them [1.2-4]. Transient response of the electron heat transport during the cold pulse propagation was investigated for better understanding of the relation between the electron heat transport and long-spatial-scale density fluctuations [1.2-5].

Figures I.1.2-3 (a) and (b) show the time evolution of the integrated power of the high frequency component (|f| > 200 kHz) of the O-mode reflectometer signal ($P_{refl.}^{H}$) and the electron temperature (T_e), respectively. The edge T_e at r/a ~ 0.85 was sharply dropped by the ablation of the pellet cloud at t = 6.32 s. The cold pulse induced by the pellet ablation propagated from the outside of the ITB into the ITB region. When the cold pulse propagated to the position of r/a = 0.54 in the ITB region at t = 6.325 s, $P_{refl.}^{H}$ was drastically reduced with a fast time scale (< 5 ms), indicating the reduction of the density fluctuation. At this timing, T_e outside the ITB (r/a = 0.6-0.85) was decreased by the cold pulse propagation, while T_e in the ITB region (r/a < 0.54) was not changed due to the slower propagation speed of the cold pulse in the ITB region. Thus, the T_e gradient became large in the outer ITB portion (r/a = 0.54-0.64). The value of T_e at r/a = 0.54 largely decreased after the density fluctuation reduction, and the ITB structure seems to be destroyed in the outer ITB portion at t = 6.35 s as shown in Fig. I.1.2-3 (c).

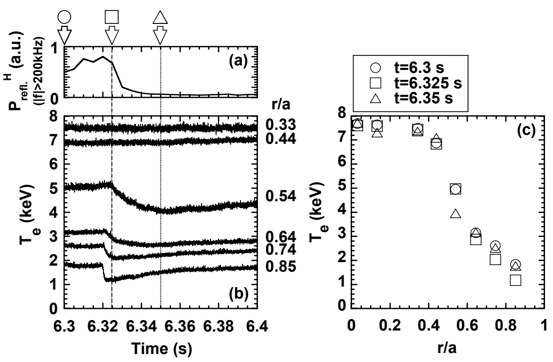

Fig. I.1.2-3 (a) Time behavior of the integrated power of the high frequency component (|f|>200 kHz) of the O-mode reflectometer signal. (b) Time evolution of the electron temperature. (c) Circles, squares and triangles show the electron temperature profile before the pellet injection, at the timing for reduction of the density fluctuation level and at the timing for maximum electron temperature reduction (r/a = 0.54), respectively. Timings are shown in (a) by the same symbols.

The transient T_e response until 20 ms after the pellet injection (Δt = +20 ms) was simulated using 2 different models on χ_e. Here, Δt = 0 ms corresponds to t = 6.32 s. In the first case (power balance χ_e case), χ_e profile was assumed identical to the power balance χ_e at t = 6.3 s. In the second case (adjusted model χ_e case), the time evolution of χ_e was adjusted in order to reproduce the T_e time behavior by introducing a χ_e model depending on T_e and T_e gradient (∇T_e). The χ_e profile used in the power balance χ_e case is shown by the solid line in Fig. I.1.2-4 (a). Time behavior of the calculated T_e for the power balance χ_e case is shown in Fig. I.1.2-4 (b). In the outside of the ITB, the calculated T_e agreed well the measured one. The cold pulse did not propagate into the inner portion of ITB (r/a < 0.44) in the simulated time scale, which was consistent with the measurements. However, at r/a = 0.54 in the ITB region, the reduction of the calculated T_e was remarkably smaller than the measured one. The power balance χ_e cannot reproduce the measured T_e time evolution in the ITB region. In order to reproduce the time evolution of T_e, strong T_e dependence of χ_e was assumed as $\chi_e \propto T_e^{-2.3}$ in the outer ITB portion (r/a = 0.54-0.62). Weak negative T_e dependence of χ_e was also assumed as $\chi_e \propto T_e^{-0.5}$ outside the ITB (r/a > 0.63). Furthermore, in the inner ITB portion (r/a = 0.3-0.5), it was assumed that χ_e is inversely proportional to ∇T_e as $\chi_e \propto \nabla T_e^{-1}$. The χ_e profiles at Δt = +10 ms and +20 ms after the pellet injection are shown by dashed and dotted lines,

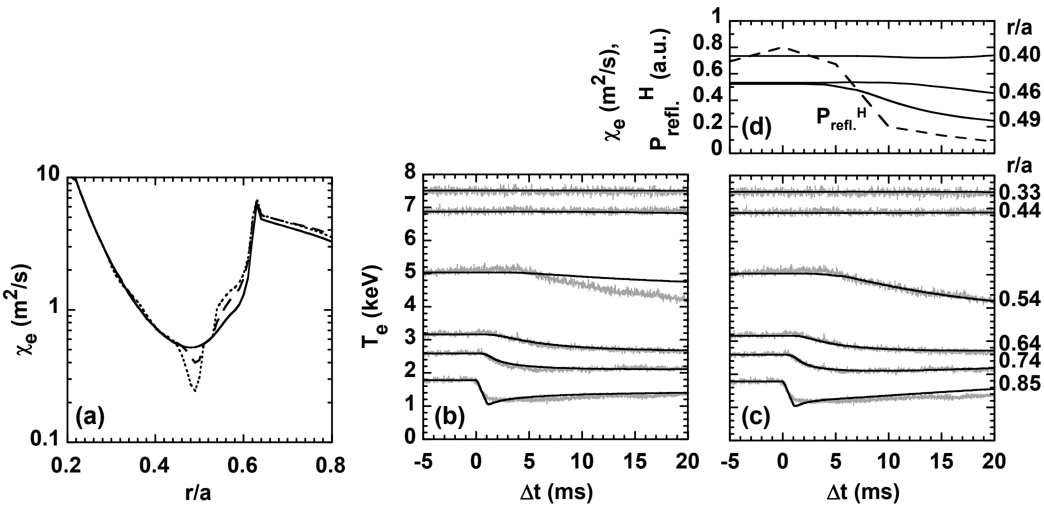

Fig. I.1.2-4 (a) The solid line indicates the χ_e profile used for the power balance χ_e case and for a period before the pellet injection in the adjusted model χ_e case. Dashed and dotted lines indicate the χ_e profiles at Δt = +10 ms and +20 ms after the pellet injection, respectively, used for the adjusted model χ_e case. Comparison of time behavior of the electron temperature between simulation (black) and measurement (gray) (b) for the power balance χ_e case and (c) for the adjusted model χ_e case, respectively. Corresponding radial positions are indicated in the right hand side. (d) Time evolutions of χ_e (solid lines) for the adjusted model χ_e case (corresponding radial positions are indicated in the right hand side.) and time integrated power of high frequency component (|f|>200kHz) of the O-mode reflectometer signal (dashed line). The $\tilde{n}/n$ starts to decrease at Δt = +5 ms.

respectively, in Fig. I.1.2-4 (a). In this case, the value of χ_e decreased in the inner ITB portion and increased in the outer ITB portion depending on the T_e profile change. At Δt = +20 ms, χ_e decreased by a factor of 2 in the inner ITB portion and increased by a factor of 1.5 in the outer ITB portion. The time behavior of the calculated T_e well agreed with the measurement, as shown in Fig. I.1.2-4 (c). Figure I.1.2-4 (d) shows time evolution of χ_e together with the time evolution of $P_{refl.}^{H}$, which represents the $\tilde{n}/n$ level in the range of k ~ 1 cm^{-1}. The value of $P_{refl.}^{H}$ decreases by 80% of its total reduction during Δt = 0 ~ +20 ms within 5 ms, while χ_e decreases by 40% at r/a = 0.49 and only 2% at r/a = 0.46 (around the cut-off layer) within 5 ms. The time scale of the χ_e reduction (~ 15 ms) is larger than that of the $\tilde{n}/n$ reduction (< 5 ms) and is similar to that the T_e profile change. The different time scales for the reductions of χ_e and $\tilde{n}/n$ indicated the decoupling of the electron heat transport and the long-spatial-scale density fluctuations. In addition, the increase in χ_e for the outer ITB portion also supported the decoupling. This result was consistent with the power balance analysis result with fully recovered temperature profiles.

1.2.3 Effects of ripple loss of fast ions on toroidal rotation

It is now widely recognized that a plasma rotation profile plays critical roles in determining the transport and the MHD stability in tokamak plasmas. In particular, for the operation of self-regulating systems, such as burning high beta plasmas, integrated plasma control schemes including the rotation profile from the edge pedestal to the core plasma regimes are required. Towards this goal, the physics basis on the driving mechanism of the plasma rotation and on the momentum transport has to be constructed [1.2-6]. The JT-60U plasmas heated with near-perpendicular neutral beam injection (perp-NBI) exhibit a ctr-rotation in the toroidal direction [1.2-7]. An inward electric field induced by a ripple loss of fast ions was considered as a candidate for the ctr-rotation in the peripheral region, because JT-60U had large toroidal field ripple. In order to reduce the toroidal field ripple, ferritic steel tiles (FSTs) have been installed inside the JT-60U vacuum vessel on the low field side [1.2-8]. Effects of the ripple loss of fast ions on the toroidal rotation velocity (V_t) have been investigated based on data with and without FSTs.

The increase in the co-rotation in the large volume (*Vol.*) configuration was observed by installing FSTs as shown in Fig. I.1.2-5 even with the similar temperature and density profiles. The ratio of ripple loss power to the input power on this discharge (I_p = 1.23 MA, B_T = 2.6 T, q_{95} = 4.1, *Vol.* = 77 m^3) reduced by installing FSTs from ~ 4% to ~ 1% for co-NBIs and from ~ 30% to ~ 10% for perp-NBIs, respectively. The magnitude of ctr-rotation increased with increasing the ripple loss power in the peripheral region. The ctr-rotation with perp-NBIs reduced by installing FSTs as a consequence of the reduction in the ripple losses. The driving mechanism of the ctr-rotation and the location of the driving source with the perp-NBI were investigated using the OFMC code and a beam perturbation experiment (I_p = 0.87 MA, B_T = 3.8 T, q_{95} = 8.2, *Vol.* = 72 m^3). In the perp-NBI modulation experiment, the large modulation amplitude and the small phase delay were observed in the peripheral region (0.7 < r/a < 0.9). From this result, the location of the driving source of the ctr-rotation was recognized in the peripheral region and this location agreed with the region where fast ion losses mainly take place in the OFMC code calculation.

The toroidal rotation profile in the core region was also discussed from the viewpoint of a moment transport by means of data from the beam perturbation experiment. The toroidal momentum diffusivity χ_ϕ and

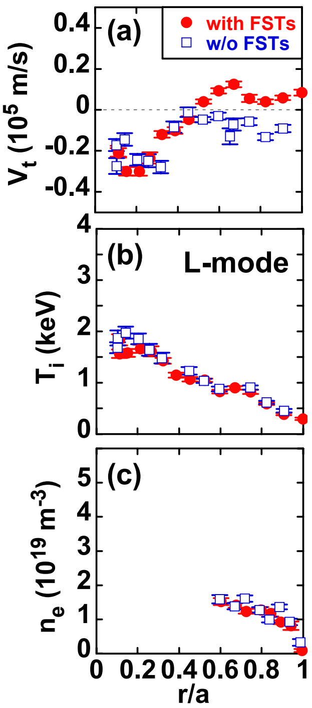

Fig. I.1.2-5 Profiles of (a) toroidal rotation, (b) ion temperature and (c) electron density with (closed circles) and without (open squares) FSTs.

the convection velocity V_{conv} in the core region (0.2 < r/a < 0.65) were evaluated from the transient momentum transport analysis using the radial profiles of the amplitude of the modulated part of V_t (V_{t0}) and of the phase delay of V_{t0}. The toroidal momentum diffusivity χ_ϕ was comparable to the ion thermal diffusivity, and V_{conv} is about 5 m/s (inward direction) at r/a ~ 0.5 in this plasma as shown in Fig. I.1.2-6. In addition, the non-perturbative V_t profile in the core region can be almost reproduced by using χ_ϕ and V_{conv} evaluated from the perturbative V_t.

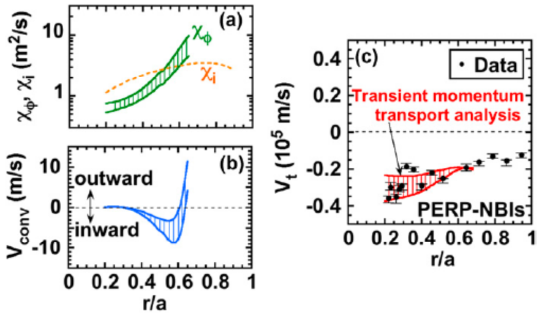

Fig. I.1.2-6 Profiles of (a) the toroidal momentum diffusivity (χ_ϕ : solid lines) and the ion thermal diffusivity (χ_i : dotted line) and (b) the convection velocity (V_{conv}) obtained from beam perturbation techniques in the L-mode plasma. (c) Comparison of reproduced non-perturbative toroidal rotation profile using the evaluated χ_ϕ and V_{conv} (solid lines) and experimental data (closed circles) with perp-NBIs.

References

1.2-1 Sakamoto, Y., et al., Proc. 21st Int. Conf. on Fusion Energy 2006 (Chengdu, 2006) CD-ROM file EX/P1-10

1.2-2 Sakamoto, Y., et al., Nucl. Fusion **45**, 574 (2005).

1.2-3 Suzuki, T., et al., Proc. 21st Int. Conf. on Fusion Energy 2006 (Chengdu, 2006) CD-ROM file EX/6-4

1.2-4 Takenaga, H., et al., Plasma Phys. Control. Fusion **48**, A401 (2006).

1.2-5 Takenaga, H., *et al., Plasma Phys. Control. Fusion* **49**, 525 (2007).

1.2-6 Yoshida, M., *et al., Plasma Phys. Control. Fusion* **48**, 1673 (2006).

1.2-7 Koide, Y., *et al., Plasma Phys. Control. Nucl. Fusion Research* **1**, 777 (1993).

1.2-8 Shinohara, K., *et al.,* in Fusion Energy 2006 (Proc. 21st Int. Conf. Chengdu, 2006) (Vienna: IAEA) CD-ROM file FT/P5-32

1.3 MHD Instabilities and Control

1.3.1 Stabilization of the Neoclassical Tearing Mode

In a fusion reactor such as ITER, the plasma operation with a high fraction of bootstrap current is expected to reduce the need for externally driven current. In such plasmas, however, neoclassical tearing modes (NTMs) would be excited. Since NTMs degrade plasma performance and sometimes cause a disruption, it is critically important to establish a scenario to control NTMs.

(1) Control of Growth of Neoclassical Tearing Mode by Central Co-ECCD

We investigated the possibility of the control of a 3/2 NTM by the electron cyclotron current drive (ECCD) at plasma central region in the same direction as the existing plasma current (co-ECCD) [1.3-1]. Since the co-ECCD decreases the safety factor in the central regime, the scale length of the current profile will decrease at the mode rational surface, which will act to stabilize the according to the modified Rutherford equation. In addition, since the co-ECCD will enhance sawtooth oscillations as previously demonstrated in JT-60U [1.3-2], some effect s are sawtooth oscillations, stabilizing or destabilizing the effect on an NTM, is expected.

In experiments, the behavior of a 3/2 NTM for no ECCD, 2-unit ECCD, and 4-unit ECCD was compared (Fig. I.1.3-1). Plasma parameters were as follows: plasma current I_p=1.5 MA, toroidal field B_t= 3.7 T, safety factor at 95% of flux surface q_{95}=3.9. Without ECCD, a 3/2 NTM appeared at β_N~1.6 (β_p=1.2) by the neutral beam injection with ~20 MW, and no sawteeth was observed throughout the discharge. For 2-unit ECCD (EC-driven current I_{EC}~70 kA), sawteeth appeared soon after ECCD, and a 3/2 NTM appeared at similar time as no ECCD case. While the growth rate of the 3/2 NTM for the 2-unit ECCD was twice as large as that for no-ECCD, the mode amplitude saturated at similar level. For 4-unit ECCD (I_{EC}~130 kA), the growth of a 3/2 NTM was suppressed and the mode amplitude was kept ~1/5 of the other cases. The mode amplitude was kept low even after the EC wave was turned off, and sustained for more than 10 times energy confinement time. In both 2-unit ECCD and 4-unit ECCD cases, the 3/2 NTM was not triggered by a sawtooth crash. Frequency spectrum of magnetic perturbations for the 4-unit ECCD showed that the mode frequency of the 3/2 NTM was modulated by a sawtooth crash while such a modulation was not observed for the 2-unit ECCD case. This suggests that a sawtooth crash could affect the 3/2 NTM. The value of β_N for the 4-unit was 6% higher than that for the 2-unit ECCD case, showing that it can be another candidate for the NTM control.

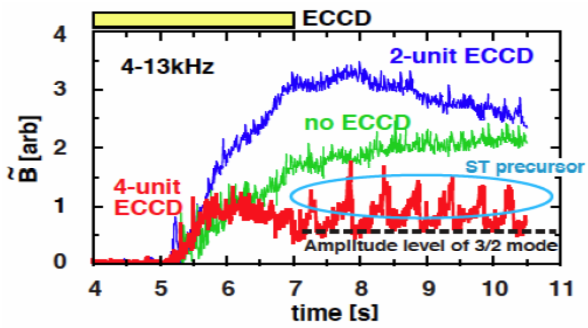

Fig. I.1.3-1 Temporal evolution of magnetic perturbation in a frequency range of 5.5 to 13 kHz for cases of no ECCD, 2-unit ECCD, and 4-unit ECCD.

(2) Active Control of Neoclassical Tearing Modes toward Stationary High-Beta Plasmas

In previous JT-60U experiments, an m/n=3/2 NTM was completely stabilized by using a real-time NTM stabilization system, where the detection of the mode location and the optimization of the injection angle of the EC wave were performed in real time. Also, a preemptive NTM stabilization, where the EC wave was injected to the anticipated mode location before the mode onset, was shown to be effective. In addition, a high-beta plasma with the normalized β_N~3 was sustained for 5 times longer than the energy confinement time by suppressing NTMs.

Effects of the central co-ECCD on an m/n=3/2 NTM were investigated. Since the central co-ECCD modifies a current profile and also destabilizes sawtooth oscillations, the co-ECCD can affect the behavior of the 3/2 NTM. In experiments, the growth of a 3/2 NTM found to be suppressed by the central co-ECCD with the amount of ~10% of the plasma current. This result demonstrates the possibility of a coexistence of sawtooth oscillations and a small-amplitude 3/2 NTM.

Stabilization of an m/n=2/1 NTM by ECCD at the mode rational surface was also performed. In particular, effects of the ECCD location on the stabilization were investigated in detail. A complete stabilization was achieved when the misalignment of the ECCD location was less than about half of the full island width (~5 cm). Also the mode amplitude found to increase when the misalignment was comparable to the island width. After the finer tuning of the ECCD location, a 2/1 NTM has been completely stabilized only with one gyrotron power (~0.6 MW). The ratio of the EC-driven current density to the bootstrap current density at the mode rational surface, j_{EC}/j_{BS}, which is a measurement of the efficiency of the NTM stabilization, was as low as ~0.5.

Simulation of the stabilization of an m/n=2/1 NTM was performed using the TOPICS code combined with the modified Rutherford equation (Fig. I.1.3-2) [1.3-4].

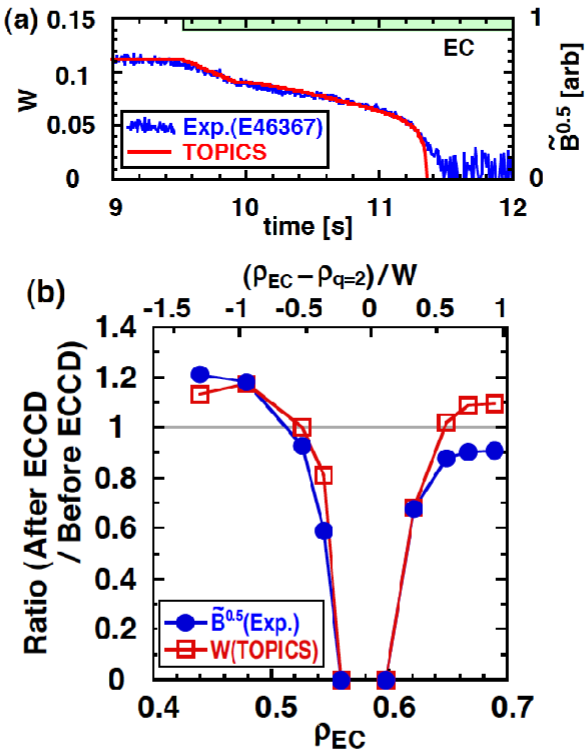

Fig. I.1.3-2 (a) Temporal evolution of island width from TOPICS simulation (W) and magnetic perturbation from an NTM experiment (~$B^{0.5}$), (b) comparison between W and ~$B^{0.5}$ at t = 11.5 s, both of which are normalized by the values at t = 9.5 s (just before ECCD).

The undermined coefficients in the modified Rutherford equation were determined by comparing with experimental results. The TOPICS simulations were found to well reproduce the stabilization and destabilization of a 2/1 NTM observed in JT-60U experiments with the same set of coefficients in the modified Rutherford equation. The TOPICS simulation also predicted that the ECCD width has a strong effect on NTM stabilization.

1.3.2 Resistive Wall Mode

To realize an economical fusion reactor, the stabilization of the low-n kink-ballooning mode is necessary. The growth rate of the external kink-ballooning mode can be reduced with a close-fitting conducting wall, and the resulting mode, the so-called resistive-wall mode (RWM), has a growth time corresponding to the time constant of the relaxation of the wall current.

(1) Effects of plasma-wall separation on the stability of resistive wall modes

It is predicted that the RWM stability, in particular the growth rate, strongly depends on the plasma-wall separation. Therefore, to clarify the effect of the plasma-wall separation on the RWM stability, we have performed current-driven RWM experiments in the JT-60U ohmic plasmas [1.3-4]. In ohmic discharges, since a MHD stability is determined by only q-profile, the behavior of the MHD instability can be purely interpreted. In the experiment, the plasma was placed near the outer wall, and the plasma current was ramped up so as to destabilize the current-driven RWM. When the edge safety factor q_{eff}, which is q-value at about 97% of minor radius, was just below 3, a thermal collapse occurred due to an instability with a clear m/n = 3/1 mode structure. The growth time of this instability is about 10 ms which is the order of the skin time of the JT-60U wall τ_w = 10 ms. Therefore, the instability has been identified as a current-driven RWM.

To investigate the effects of the plasma-wall separation on the RWM, the plasma-wall separation was changed from shot to shot, and the clearance feedback control was utilized to keep the plasma-wall separation constant in a shot. In consequence, it is found that the growth rate has the strong dependence on the wall position as shown in Fig. I.1.3-3. Thus, the growth rate became smaller with decreasing the plasma-wall separation. Additionally, the observed growth rates have been compared with the AEOLUS-FT code, which is based on the resistive MHD equations with a resistive wall, and the model of the RWM dispersion relation. According to the AEOLUS-FT calculations, an m/n = 3/1 kink mode and an m/n = 2/1 tearing mode are unstable together under these experimental conditions. The dependence of the observed growth rate on the wall position is in qualitative agreement with an m/n = 3/1 kink branch, in contrast, it is quite different from an m/n

= 2/1 tearing branch. However, in this comparison, the absolute value of the observed growth rates is about a factor 10 smaller than the dispersion relation with τ_w = 10 ms. Taking into account the time scale of the equilibrium evolution, the observed growth rate could be smaller than a liner growth rate [1.3-5]. Actually, the reevaluated growth rates are consistent with the RWM dispersion relation with τ_w = 10 ms. This point is required to investigate in future work.

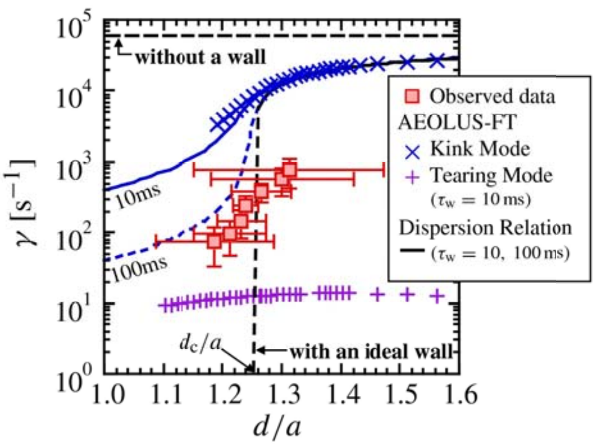

Fig. I.1.3-3 Dependence of growth rates on wall position. Thick lines show a dispersion relation with τ_w = 5, 10, 20, 50, 100 and 200 ms. Growth rates with an ideal wall and without a wall are also shown. Crosses and plusses are the growth rates of kink and tearing branches calculated by the AEOLUS-FT code in the τ_w = 10 ms and q_{surf} = 2.9 case. Squzares and diamonds indicate the experimentally obtained and re-evaluated growth rates.

(2) Identification of a Low Plasma-Rotation Threshold for Stabilization of the Resistive-Wall Mode

There are two different procedures for stabilizing RWM. The first is the feedback control stabilization using externally applied non-axisymmetric magnetic fields with coils in order to compensate for the diffusion of flux. The second is stabilization of RWM by the toroidal plasma rotation. Both theories and experiments imply that the critical rotation velocity is around 1%–2% of the Alfven velocity. The most significant problem in the previous experiment is that the investigation of the critical rotation is performed with the magnetic braking by adding an asymmetric magnetic field, the so-called error field. It has been pointed out that the error field plays a very important role in the destabilization of RWM and should be substantially reduced near the limit for the ideal mode without a wall, the so-called "no-wall limit". Since RWM stability itself is affected by the error field, which is the origin of magnetic braking, we should not use the magnetic braking in the investigation of critical rotation.

For investigating the critical rotation, we employ a weak reversed magnetic shear plasma with I_p = 0.9 MA and B_t = 1.58 T [1.3-6]. Internal inductance of this plasma is decreased to l_i = 0.8 to reduce the no-wall limit. The clearance between the plasma surface and the first wall on the outer midplane is d_0 = 20 cm, which is equivalent to a ratio of the radius of the first wall to the plasma minor radius of d/a = 1.2. A very low rotation threshold was obtained in the JT-60U in an investigation of the critical rotation for stabilizing RWM by controlling the toroidal plasma rotation with changing the combination of tangential neutral beams (NBs) without magnetic braking. The observed critical rotation is V_t ~20 km/s and corresponds to 0.3% of the Alfven velocity at the q=2 surface, much smaller than the previous prediction with the magnetic braking as shown in Fig. I.1.3-4. This low critical rotation does not increase as the beta *value* increases toward the ideal wall limit. Also an ITER relevant low rotation (~ 0.4% of the Alfven velocity) stabilization of RWM is demonstrated for 50 times the skin time of the first wall. These results indicate that for large plasmas such as in future fusion reactors with the low rotation, the requirement of the additional feedback control system for stabilizing RWM is much reduced.

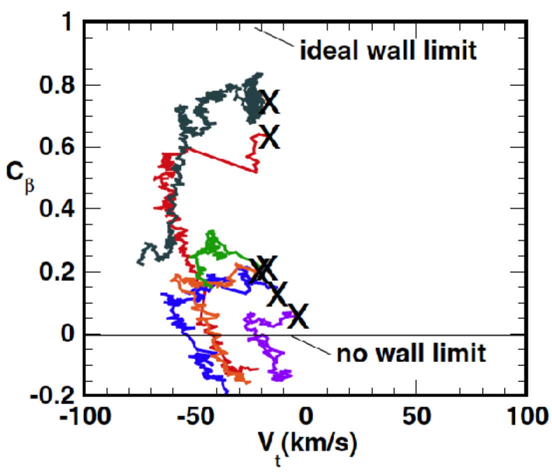

Fig. I.1.3-4 Trajectories of the C_β versus toroidal rotation at q = 2. The crosses denote the onset points of RWM.

1.3.3 Confinement Degradation and Transport of Energetic Ions Due to RSAEs and TAEs in Weak Shear Plasmas

Alpha particles play an important role in the plasma heating in burning plasmas. However, a high alpha particle pressure gradient can induce Magnetohydrodynamics (MHD) instabilities such as Alfvén Eigenmodes (AEs) (toroidicity-induced AEs (TAEs)) or Energetic particle modes (EPMs). These MHD instabilities can cause the enhanced transport of alpha particles from the core region of the plasma, which could degrade the performance of burning plasmas. Moreover, lost alpha particles could also damage the first walls. Thus, the understanding of the alpha particle transport due to these instabilities is an important research issue for ITER. Then, several kinds of AEs and EPMs have been predicted theoretically and observed experimentally and their effects on energetic ions have been studied in several Tokamaks, ST and Helical devices. Recently, another type of AEs, in which the frequency is largely swept with the time scale of a few hundreds millisecond and then saturates as the minimum value of the safety factor (q_{min}) decreases, have been extensively studied. These frequency behavior can be explained by reversed-shear induced AEs (RSAEs) [1.3-7] and its transition to TAEs. Confinement degradation of energetic ions due to these AEs has been confirmed from the measurements of the total neutron rate as shown in Fig. I.1.3-5 [1.3-8]. In order to investigate the radial transport of energetic ions due to these modes, the line-integrated neutron emission profile are measured using a large neutron collimator array [1.3-9] and compared with the calculated value by a classical theory using a transport code TOPICS. As a result, it is found for the first time that energetic ions are transported from the core region of the plasma due to these AEs as shown in Fig. I.1.3-6. Further, changes in the energy distribution and the flux of the charge exchange (CX) neutral particle are measured [1.3-10] in order to investigate the energetic ion transport in the velocity space. The changes in the energy distribution of CX neutral fluxes suggest the radial transport is due to the resonance interaction between energetic ions and AEs. Thus, the results of the measurements of neutron emission profile and CX neutral particle flux indicate that the radial transport of energetic ions is induced by the resonance interaction between energetic ions and AEs.

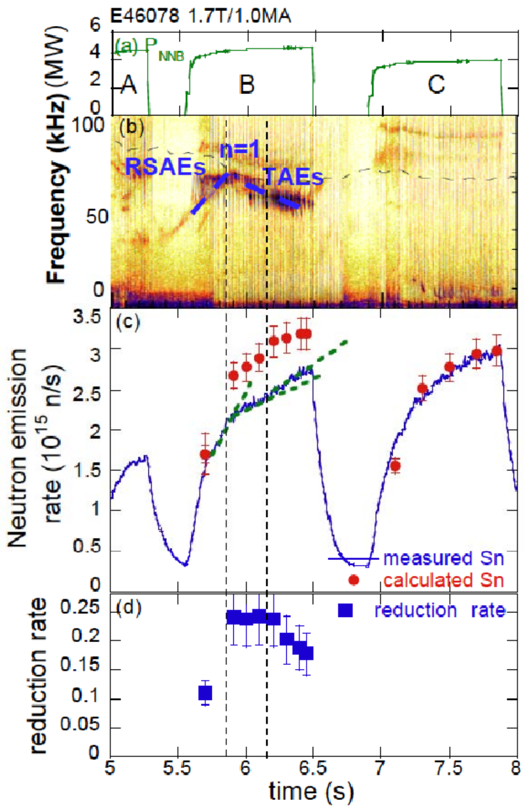

Fig. I.1.3-5 Time traces of (a) the injection power of NNB, (b) the frequency spectrum of magnetic fluctuation, (c) the measured neutron emission rate (solid line) and the calculated one using the OFMC code (circles) and (d) the reduction rate of neutron emission rate (ΔSn/Sn) in E46078 shot.

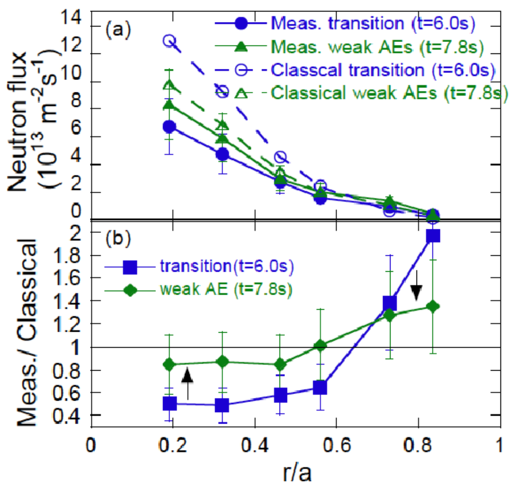

Fig. I.1.3-6 (a) Line-integrated neutron signals of measurement (Meas.) in the transition phase (closed circle), w/o AEs (closed triangle) and that predicted by classical theory (Classical) in the transition phase (open circle), with weak AEs (open triangle). (b) Ratio of Meas. to Classical in transition phase (square) and with weak AEs (diamond)

References
1.3-1 Isayama, A., *et al., Plasma Fusion Res*. **1**, 030 (2006).
1.3-2 Isayama, A., *et al., Plasma Fusion Res*. SERIES **5**, 324 (2002).
1.3-3 Isayama, A., *et al., Nucl. Fusion* **47**, 773 (2007)
1.3-4 Matsunaga, G., *et al., Plasma Phys. Control. Fusion* **49**, 95 (2007)
1.3-5 Callen, J.D., *et al., Phys. Plasmas* **6**, 2963(1999)
1.3-6 Takechi, M., *et al.*, *Phys. Rev. Lett*. **98** (2007) 055002.
1.3-7 Takechi, M. *et al., Physics of Plasamas* **12,** 082509 (2005)
1.3-8 Ishikawa, M., *et al., Nucl. Fusion* 47, 849 (2007)
1.3-9 Ishikawa, M., *et al., Rev. Sci. Instrum*. **73**, 4237 (2002).
1.3-10 Ishikawa, M., *et al., Rev. Sci. Instrum.* **75**, 3963 (2004).

1.4 H-Mode and Pedestal Research

Since the performance of ELMy H-mode plasmas can be determined by the performance of the pedestal plasmas, it is important to understand what physics determine the pedestal performance for the better prediction of pedestal plasmas in ITER. In addition to this, mitigation of the instantaneous ELM heat load should be established to achieve the required lifetime of divertor target plates in ITER. To address these issues, various experiments have been performed. Effects of toroidal field (TF) ripple on the pedestal performance and ELM characteristics were investigated by comparing with and without ferritic steel tiles (FSTs) using various plasma configurations including JET/JT-60U similarity configuration. As a co-toroidal rotation increases, the pedestal pressure tends to increase except for JET/JT-60U similarity configuration. Especially in a large plasma configuration where TF ripple without FSTs was large (~2%), an improvement of the pedestal pressure was observed even at the fixed toroidal rotation indicating distinct effects of the TF ripple. As for the size of type I ELMs, on the other hand, the normalized ELM size to the pedestal stored energy ($\Delta W_{ELM}/W_{ped}$) decreased with increasing the counter rotation in all configurations. The fact that there was a systematic difference in the variation of $\Delta W_{ELM}/W_{ped}$ as a function of toroidal rotation indicated that the plasma configuration itself is one of important parameters to determine the ELM characteristics rather than the TF ripple [1.4-1]. The ELM frequency dependence in the grassy ELM regime (δ>0.5 and q_{95}>6) was investigated in terms of the toroidal rotation at the pedestal and total poloidal beta (β_p). As counter rotation increased, the ELM frequency clearly increased up to ~1400 Hz independent of β_p from 0.84 to 1.88. Even in the no-rotating plasma with balanced-NBIs similar to the ITER condition, a high ELM frequency of ~400 Hz has been observed without a large energy loss (less than 1% of the pedestal stored energy) [1.4-2]. QH-mode experiments as an inter-machine experiment with DIII-D was performed to understand the mechanism of the QH mode transition with co-NBIs. The new CXRS system revealed that similar depth of E_r well of ~40kV/m was observed both in the ELMy phase (just before an ELM) and the QH phase in JT-60U in contrast to DIII-D, where deeper E_r well of ~100kV/m has been observed. By making use of recent improvement of edge diagnostics with the fast time resolution, studies of ELM dynamics have been progressed. Just after a current ramp up, the higher pedestal pressure could be achieved together with larger type I ELMs, which may relate the improvement of the edge stability.

1.4.1 Roles of toroidal rotation at the plasma edge, toroidal field ripple and configuration on ELMs

In the previous experiments, effects of the plasma rotation and the TF ripple on the ELM characteristics have been studied by changing the plasma configurations (δ_{ripple}~0.4% at small V_P~50 m^3, δ_{ripple}~1% at middle V_P~65 m^3, and δ_{ripple}~2% at large V_P~75 m^3). Figure I.1.4-1 shows a relation of $\Delta W_{ELM}/W_{ped}$ with a $V_{T,ped}$ under a P_{SEP}~5-6 MW at each plasma configuration, showing similar slopes in the dependence of $\Delta W_{ELM}/W_{ped}$ on $V_{T,ped}$. A reason for the narrower dynamic range toward the co-direction in the $V_{T,ped}$ for a larger volume configuration is due to an offset toroidal rotation towards the counter-direction at the edge region due to larger losses of fast ions.

The most important point in Fig. I.1.4-1 is a systematic difference in the $\Delta W_{ELM}/W_{ped}$ (in other words, an offset of $\Delta W_{ELM}/W_{ped}$) varying from ~9% (small-volume), ~6% (middle-volume), and ~4% (large-volume) at a given $V_{T,ped}$~-50 km/s, suggesting important roles of other parameters in determining the edge stability, such as TF-ripple, loss of fast ions, and plasma configuration. It should be noted that the pedestal pressure and/or the poloidal beta, $\beta_{p,ped}$, tends to decrease when the plasma volume increases.

However, the decrease in ΔW_{ELM} is larger than that seen in W_{ped}, and hence $\Delta W_{ELM}/W_{ped}$ decreases when the plasma volume or δ_{ripple} increases.

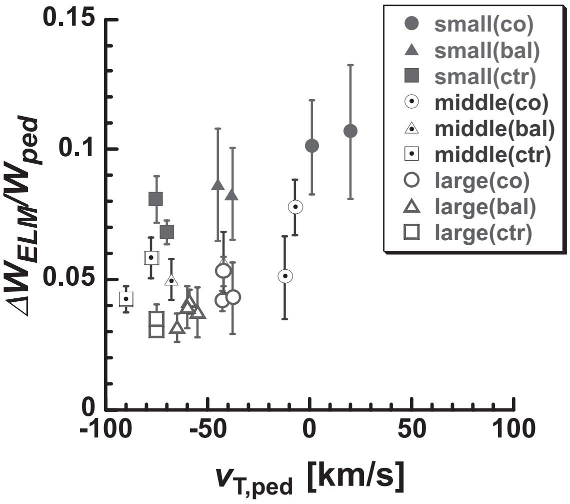

Fig.I.1.4-1 ELM energy loss normalized by the pedestal stored energy, $\Delta W_{ELM}/W_{ped}$, plotted against toroidal rotation at the top of the pedestal, $V_{T,ped}$, in the tangential co-, balanced-, and counter- plus perpendicular-NBI heated plasmas at a P_{SEP}~5-6 MW for three plasma configurations having TF ripples of δ_{ripple}~0.4% (small), 1% (middle), and 2% (large), respectively.

In order to separate a strong linkage among TF-ripple, loss of fast ions and plasma configuration, a comparison between the pre- and the post-FSTs experiments makes it possible to clarify the effects of the reduced TF-ripple on ELMs and the pedestal under the matched plasma configurations eliminating uncertainties in the shaping effect. Figure I.1.4-2 shows that the dependence of $\Delta W_{ELM}/W_{ped}$ on $V_{T,ped}$ is similar between the pre- and the post-FSTs. This is because both the ELM energy loss ΔW_{ELM} and the pedestal stored energy W_{ped} increase as $V_{T,ped}$ increased toward the co-direction, and hence, similar dependences of the normalized ELM energy loss $\Delta W_{ELM}/W_{ped}$ on $V_{T,ped}$ have been observed even after the FSTs installation. So, it is suggested that the role of "configuration" is more important than δ_{ripple} in the appearance of a small type I ELM in a large volume plasma, and the TF-ripple itself and/or losses of fast ions may not be directly related to the normalized ELM energy loss, $\Delta W_{ELM}/W_{ped}$.

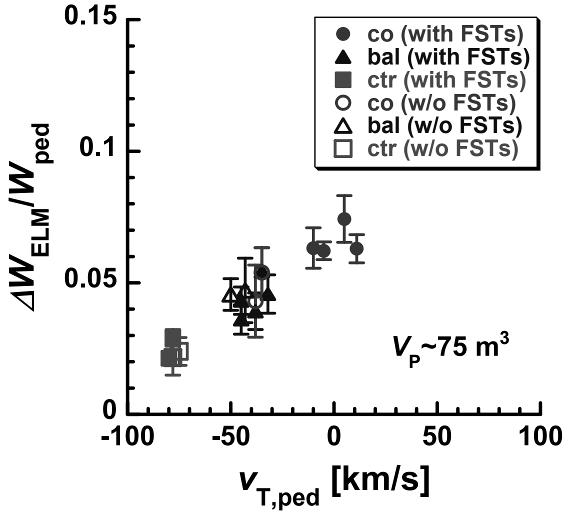

Fig.I.1.4-2 Comparison of pre- and post-FSTs campaigns in terms of the ELM energy loss normalized by the stored energy in the pedestal region, $\Delta W_{ELM}/W_{ped}$, plotted against the toroidal rotation at the top of the pedestal, $V_{T,ped}$, in the tangential co- (circles), balanced- (triangles), and counter- (squares) plus perpendicular-NBI heated plasmas at P_{SEP}~5 MW for the configuration having a large plasma volume (V_P~75 m^3).

1.4.2 ELM frequency dependence on toroidal rotation in the grassy ELM regime

A systematic study of the effect of the level of toroidal plasma rotation at the top of the ion temperature pedestal (T_i^{ped}) on the ELM characteristics in JT-60U has been performed. The level of toroidal plasma rotation has been varied by using different combinations of tangential and perpendicular neutral beam injection (NBI). In the grassy ELM regime at high triangularity (δ) and high safety factor (q), the ELM frequency clearly increased up to ~1400 Hz, when counter (ctr) plasma rotation was increased as shown in Fig. I.1.4-3. The response of the ELM frequency was independent of poloidal beta (β_p) in the range $0.84<\beta_p<1.88$ at $\delta>0.53$. Even in non-rotating plasma with balanced NBIs, a high ELM frequency of ~400 Hz has been observed without large energy loss. When the frequency of the plasma rotation in the co-direction of the plasma current becomes higher than ~1 kHz, type I ELMs with a frequency of ~20 Hz have been observed. The achieved pedestal pressure and plasma confinement were similar both in plasmas with type I ELMs and in plasmas with grassy ELMs. The energy loss due to grassy ELMs was evaluated from the reduction in the electron temperature, and the ratio of the energy loss to the pedestal stored energy was less than 1%.

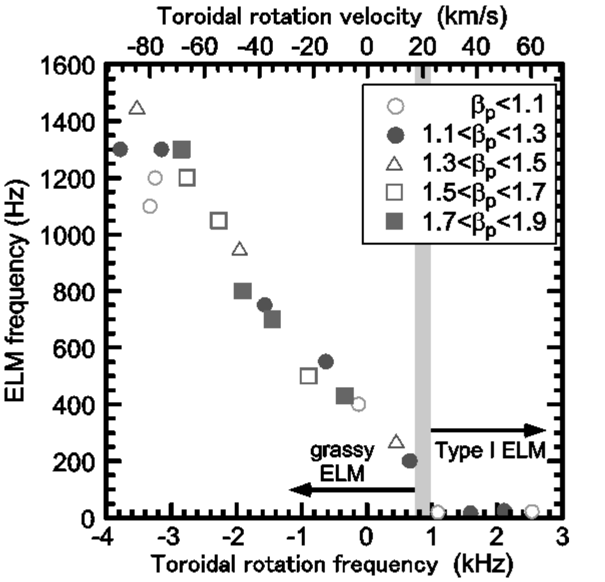

Fig.I.1.4-3 ELM frequency dependence as a function of toroidal rotation frequency measured at the top of T_i pedestal for the different β_p range. Corresponding to the toroidal rotation speed for the typical plasma condition is also shown at upper horizontal axis.

References

1.4-1 Kamiya, K., *et al.*, *Plasma and Fusion Research*, **2**, 005 (2007).

1.4-2 Oyaman, N., *et al.*, *Plasma Phys. Control. Fusion*, **49**, 249 (2007).

1.5 Divertor/SOL Plasmas and Plasma-Wall Interaction

1.5.1 ELM heat and particle fluxes

Studies of ELM plasma propagation in SOL have been progressed both at High- and Low-field-side [1.5-1]. Radial distributions of the ELM plasma was measured with three reciprocating Mach probes (synchronized sampling of 500kHz) in Type-I ELMy H-mode with frequency of 25-50 Hz. Multi (a few to several) peaks were generally observed in the ion saturation current (j_s) during ELM activities ($\tilde{B}_p$). Radial propagation time ($\tau_\perp$) from near-separatrix to the Mach probe location (r) was evaluated from time lag of the first large j_s peak after large $\tilde{B}_p$ start. ELM propagation to the midplane first wall ($\tau_\perp^{mid}$ = 50-90 μs at r^{mid} = 13cm) was faster than the parallel convection time to the outer divertor ($\tau_{//}^{SOL\text{-}LFS}$ ~100 μs), suggesting ELM plasma loading to the first wall. Radial distribution of $\tau_\perp^{mid}$ shows that the velocity ($V_\perp^{mid} = r^{mid}/\tau_\perp^{mid}$) was increased from 0.4-1.5 km/s near separatrix to 1.5-3 km/s at the far SOL, as shown in Fig.I.1.5-1. Here, peak j_s^{mid} distribution was characterized by a wide e-folding length of 7.5 cm.

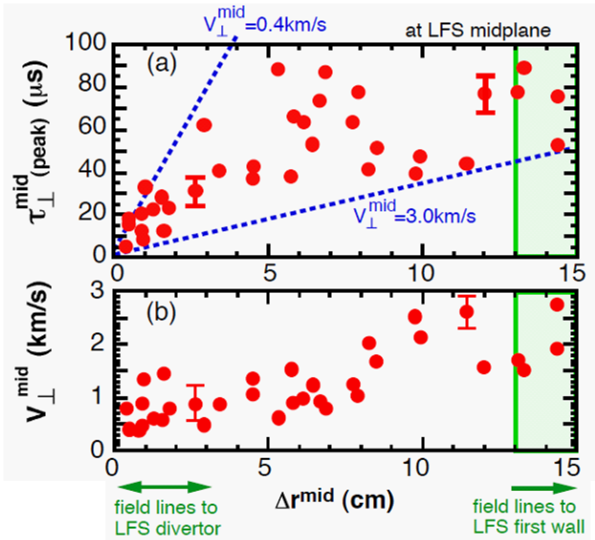

Fig.I.1.5-1 Radial distributions of (a) time delay of the first j_s^{mid} peak, $\tau_\perp^{mid}$*(peak)*, (b) averaged propagation velocity, $V_\perp^{mid}$*(peak)*, at Low-field-side midplane

In the waveform of multi-peak j_s^{mid}, similar characteristics were seen for series of ELM events. Radial scale of ELM filaments was determined from duration of the large j_s^{mid} peak (δt_{pk}^{mid}), 4-10 μs. Corresponding radial scale ($V_\perp^{mid}\delta t_{pk}^{mid}$) was 0.3-1.8 cm near separatrix (r^{mid} < 5 cm) and was increased to be 1 - 4 cm at the far SOL. Deposition image of particle flux to outer baffle and dynamics of the filament-like structure were also measured with new fast TV camera. Different time scales of ELM plasma transport were determined at the HFS SOL. Multi-peak j_s^{mid} was seen, however, short delay (≤ 30 μs) of large j_s^{HFS} was seen only in narrow region near separatrix (Δr^{mid} < 0.4cm). This would cause fast heat and particle transport to the HFS divertor simultaneously to that to the LFS divertor. On the other hand, in the far SOL at HFS, particle flux reached with larger time lag of the parallel convection time from the LFS SOL ($\tau_{//}^{SOL\text{-}LFS}$=250-300 μs).

Fast measurements (20kHz sampling) of low ionization spectral lines such as three HeI, D_α and CII started for study of ELM plasma dynamics at the LFS divertor such as T_e, n_e, neutral and carbon ionization fluxes. Just after ELM event, T_e was increased, then it decreased due to large increase in recycled neutrals. At the same time, carbon yield became lowest.

1.5.2 Particle control in long-pulse discharges

Wall saturation has been investigated in 30s-ELMy H-mode discharges. Wall pumping rate was determined by a particle balance analysis and it decreased with a decay constant of several seconds and then became constant. After a few discharges with a density of 65% of the Greenwald density, the wall-pumping rate became negative, i.e. outgassing. The outgassing rate was correlated mostly with an increase in the tile surface temperature near the outer strike point. Thus, in high density discharges (80% of the Greenwald density), where heat loading to the strike point was largely reduced due to radiation loss, wall-pumping was observed over the long pulse [1.5-2]. The wall-pumping rate became larger than that explained only by the co-deposition of deuterium with carbon.

Divertor-pumping is effective to control the divertor plasma detachment and the main plasma density. Under the wall saturated condition (outgassing), it was found that the wall-pumping rate changed so as to maintain the main plasma density; outgas flux was decreased when the divertor-pumping flux was increased by opening the shutter of the divertor cryopumps. This fact suggests that the wall-pumping can be recovered to some extent (but still negative rate) in several seconds, i.e. dynamically retained changed by external control of the divertor pumping flux [1.5-3].

1.5.3 Spectroscopic study in Divertor

For high density divertor discharges, MARFE appears around the X-point, where the C IV brightness is largely peaked. Measurement of the absolute intensities of C IV lines emitted from this peak, using 2-dimential and wide-wavelength spectrometer system, could determine the population density ratio of the C^{3+} excited levels, and the result was analyzed by a collisional-radiative model [1.5-4]. The result of this analysis is shown in Fig I.1.5-2, indicating that the population densities of the excited levels were composed of the ionizing and the recombining plasma component with an electron temperature of 6.3 eV and an electron density of 7.8 x 10^{20} m^{-3}. By using the collisional-radiative model with these evaluated parameters and the C IV brightness, the line-radiation power was evaluated: the line-radiation power from the ionizing and the recombining plasma component of C^{3+} was, respectively, 60% and 2% of the total radiation power (1.4 MWm^{-2}) measured by a bolometer along the chord at the X-point. It was also found that the volume recombination flux of C^{4+} is larger by two orders of magnitude than the ionization flux of C^{3+}; the volume recombination is a main process to produce C^{3+}, i.e. a main radiator in the X-point MARFE.

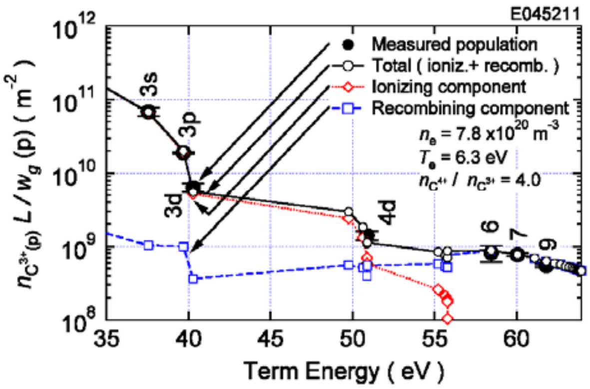

Fig. I.1.5-2 Comparison of measured line-integrated population density and fitted population density, divided by the statistical weight, as a function of term energy of the excited level.

Two-dimensional structure of the volume recombination of deuterium, i.e. D^+ and e^-, was investigated in the partially detached divertor. The deuterium Balmer-series lines (D_α, D_β, ..., D_θ) were measured two-dimensionally with a spatial resolution of ~ 1 cm [1.5-5] and distributions of their emissivities were reconstructed with a tomography technique [1.5-6]. Emissivity ratio of D_β to D_α lines was compared to that calculated by the collisional-radiative model. This ratio could not be explained only by the excitation of the ground state deuterium by electron impact, indicating that the volume recombination contributed to the D_β emission. Fig. I.1.5-3 shows two dimensional distribution of D_β to D_α line ratio, and volume recombination process is dominant above the inner strike point with ~ 8 cm and ~ 4 cm, respectively, in the r- and the z-direction as indicated by the black curve. In this region, the electron density and temperature were evaluated to be ~ 5×10^{20} m^{-3} and < 0.3 eV, respectively, from the ratios of the D_α, D_β, ..., D_θ emissivities.

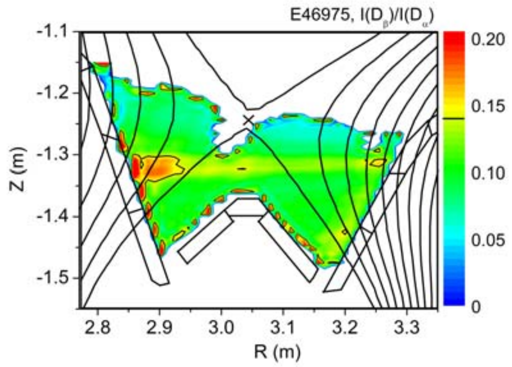

Fig. I.1.5-3 The two-dimesional ratio of the D_β emissivity to the D_α emissivity on the poloidal cross-section. The black contour line corresponds to a ratio of 0.14.

1.5.4 Chemical sputtering study

In the previous work [1.5-7], the chemical sputtering yield was evaluated by using 'Loss-Events/Photon' coefficients measured in PISCES-A. Because, however, the *LEP* coefficients depend on the transport loss of the hydrocarbons, which may depend on devices, the *LEP* coefficients, CH_4, CD_4, C_2H_4 and C_2H_6 loss events per CH, CD and C_2 photon, were recently measured carefully [1.5-8] in many tokamaks. By using these measured *LEP* coefficients, the chemical sputtering yield, reported in [1.5-6], was re-evaluated and is shown in Fig. I.1.5-4. Compared to the chemical sputtering yield in the previous report [1.5-6], the yield itself did not change. But the ion flux dependence of the yield, evaluated by the regression analysis with Y_{chem} $\Gamma_{ion}{}^{\alpha}$, became weaker by 40%; α decreased from ~0.3 to ~0.2.

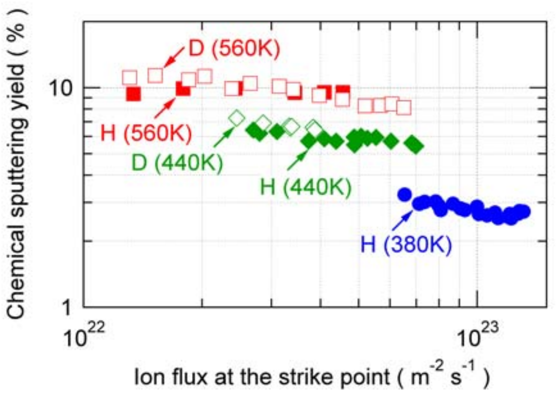

Fig. I.1.5-4 Reevaluated chemical sputtering yield as a function of the ion flux at the strike point.

1.5.5 Study of dust dynamics

Movement and velocity of emission by dusts were measured with a fast visible TV camera (2-6 kHz) from tangential port [1.5-9]. In main SOL, many dusts with various directions were observed, in particularly, in the first NB shot after hard disruptions (large ΔW_{dia}) and overnight (~6 hours) GDC. In divertor, many dusts were produced at HFS, in particular, for high HFS strike-point case: large ELM heat and particle loading on thick deposition layers may enhance producing dusts. Fast velocity of toroidal or/and poloidal movement (0.2-0.5 km/s) was faster than that of radial movement (0.05-0.1km/s). Direction of toroidally moving dusts was mostly towards ion drift (I_p): the direction is consistent with the SOL flow measurement HFS and LFS. It was also found that direction of radial movement at LFS SOL above the divertor changed from inward to outward at ELM occurrence.

1.5.6 Progresses of SOL and divertor code development and simulation study

We have been developed a comprehensive SOL/divertor simulation code system for the interpretation and the prediction on behavior of SOL/divertor plasmas, neutrals and impurities [1.5-10]. The code system consists of (i) the 2D fluid code: SOLDOR, (ii) the neutral Monte-Carlo (MC) code: NEUT2D, and (iii) the impurity MC code: IMPMC. The integration code "SONIC" was almost completed and examined to simulate the SOL and divertor plasmas in JT-60U.

SOLDOR and NEUT2D codes have been applied to analysis of JT-60U experiments and divertor designing of JT-60SA. The X-point MARFE in high density experiments was examined. It was found that transport of carbon ions generated at the private dome are enhanced in the private plasma, causing the large radiation peaking near the X-point. The pumping capability of JT-60SA was evaluated through the simulation. A guideline to enhance the pumping efficiency was obtained in terms of the exhaust slot width and the strike point distance.

Code-code benchmark is one of very important collaboration of divertor/SOL topical group in ITPA (International Tokamak Physics Activity). Benchmark work between SONIC code (SOLDOR and NEUT2D) and SOLPS5.0, which has been used for the ITER divertor designing, started. We applied both codes on a typical L-mode divertor plasma on JT-60U, using each mesh structure and identical input parameters such as input power, plasma edge density, gas puff flux and divertor pumping speed. As a result, electron temperature and density in the SOL and divertor plasmas agreed fairly well.

1.5.7 Tungsten erosion and deposition

Tungsten deposition in the divertor region eroded from the W-tiles installed in the outer divertor (P-8 section) was measured to study tungsten migration [1.5-11]. Poloidal distribution of tungsten surface density at the P-8 toroidal section is plotted in Fig.I.1.5-5, and compared to deposition profile of isotope carbon (^{13}C) (a) and the normal carbon (^{12}C) deposition profile (b).

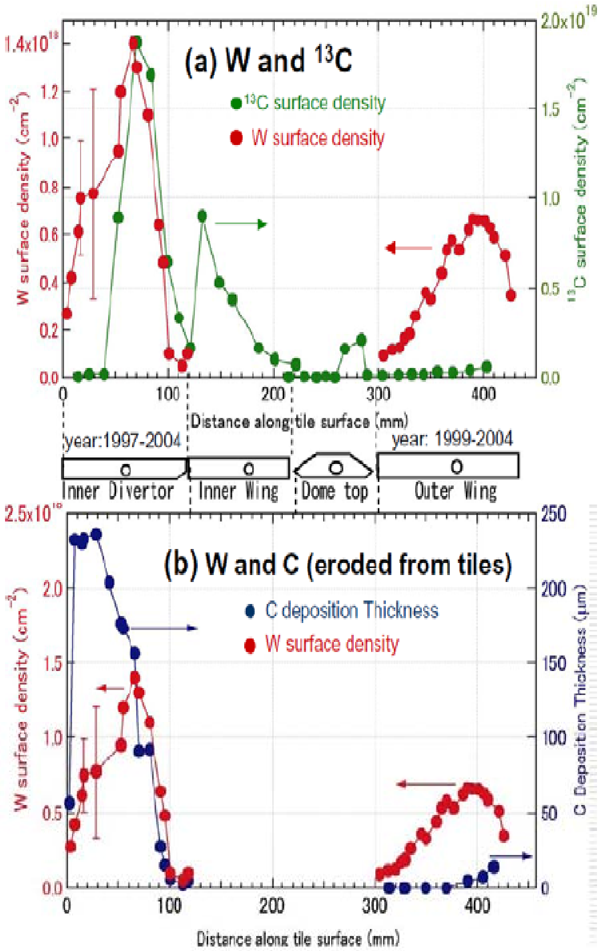

Fig. I.1.5-5. Poloidal distribution of tungsten surface density in cm^{-2} in the divertor region (P-8 toroidal section) with ^{13}C density (a) and C deposition thickness (b).

Here, carbon isotope was used for tracer of the carbon deposition just before machine ventilation in 2004. In the inner divertor tile, the deposition positions of tungsten and ^{13}C are the same, indicating that both elements migrated near separatrix field lines and deposited. This was similar to the results in ASDEX-U [1.5-12]. For normal carbon deposition (sputtered from graphite tiles), carbon ions also migrated in SOL plasmas formed thick deposition layer in the upper side of the inner divertor, see Fig.I.1.5-5 (b).

On the outer wing of the dome tiles, deposition of ^{13}C (puffed from the hole at the outer divertor tiles) and normal carbon deposition was increased near the exhaust slot similar to the case of tungsten deposition. The ratio of the tungsten to the carbon, however, was higher by an order of magnitude on the outer wing than that on the inner divertor. In addition, tungsten deposition on the outer wing at P-5 section is negligibly small compared with that at P-8 section (W-tile area). This suggests that the tungsten deposition on the outer wing tiles is highly localized near the W-tiles. The tungsten deposition could take place by inward drift motion following sputtering and ionization of tungsten atoms from the W-tiles or direct deposition of emitted tungsten atoms by disruption or ELMs etc. without ionization. Similar process could also occur for the carbon deposition.

1.5.8 C-deposition and ^{13}C tracing

Tracing isotope gas ($^{13}CH_4$) was puffed into the outer divertor plasma at P-8 toroidal section SOL plasmas in 2004. After the $^{13}CH_4$ gas puffing experiment, carbon tiles in P-8 and P-5 (toroidally 60^o apart from P-8) toroidal sections were extracted and the toroidal distribution of ^{13}C deposition on the divertor tiles have been investigated [1.5-13, 1.5-14].

Poloidal distribution of ^{13}C deposition density on the outer divertor tiles had a peak near the strike point. At the same time, ^{13}C deposition at the outer strike point was peaked toroidally in the vicinity of $^{13}CH_4$ puffing nozzle with the density of ~10^{21} cm^{-2}. There was a large asymmetry between upstream and downstream sides along the field lines; heavy deposition in downstream side and little deposition in upstream side, suggesting that ^{13}C ions were transported to the downstream by the plasma flow in the divertor region. Poloidal distribution of ^{13}C deposition on the inner divertor tiles were investigated in both P-5 and P-8 toroidal sections, and the depositions were peaked near strike-point but at a private area. Determination of ^{13}C transport through the private flux region (ion or hydrocarbon gas) will be necessary.

The poloidal distribution of ^{13}C on both the inner and the outer dome tiles was similar to the carbon deposition distribution on the outer divertor: ^{13}C influx on the lower side of the dome-wing tiles was larger than that on the dome top. ^{13}C was also deposited on the poloidal side surfaces facing pumping slot on which ionized particles couldn't reach: at 3 mm depth from the plasma-facing surface. These results suggest transport of ^{13}C neutral particles through the private flux region. Small amount of ^{13}C was deposited on the toroidal side surfaces near the dome top, facing to the upstream side.

1.5.9. Hydrogen-isotope retention

The total hydrogen isotope retentions depending on the tile location was investigated [1.5-15]. The hydrogen concentration was generally increased with the thickness of the co-deposited carbon layers, and was roughly classified into two different values. The lowest concentration of 0.02 in (H + D)/C was found in the co-deposited layers on the inner divertor tile, while the highest concentration of 0.13 in (H + D)/C was in the co-deposited layers on the bottom side of outer dome wing tile facing to the pumping slot. The hydrogen isotopes retention of the whole divertor area is roughly estimated to $4x10^{24}$ atoms. Such low H+D retention in JT-60U compared to that in the other tokamaks is largely owing to higher temperature of the PFC tile surfaces.

Hydrogen retention in the codeposited layers on the collector probes under the divertor PFCs were summarized in Fig.I.1.5-6. The maximum D/H ratio of ~3.6 appeared underneath the dome region. The hydrogen (H+D) retention in the layers was $\sim1.4x10^{23}$ atoms/m^2, and H+D/C was large, i.e. ~0.85 (average of two samples: ~0.75). On the other hand, no appreciable co-deposited layer was found on the collector probes installed underneath the outer baffle plate (No.5-10), and the hydrogen retention was almost background level. During the discharges, the temperature of the shadowed area was maintained at ~470 K (operation temperature), which was still low compared with the temperature of the surfaces of PFCs.

(a)

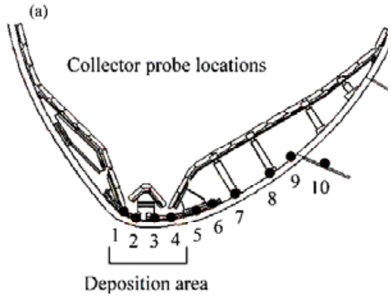

(b)

Collector probe No.	1	2	3	4
H+D (x 10^{22} atoms /m^2)	3.22	14.1	12.6	4.32
D/H ratio	2.80	3.60	1.81	2.62
Dep. Thickness (μm)	—	2.33	1.67	—
C density (g/cm^3)		1.88	1.78	
(H+D)/C		0.64	0.85	

Baking temperature :~420 K

Fig.I.1.5-6 (a) Collector probe locations and (b) results of the collector probe analyses (collector probe samples: 2003-2004).

References

1.5-1 Asakura, N., et al. *, Proc. 21st IAEA Conf., on Fusion Energy 2006 (Chengdu 2006)* CD-ROM file EX9-2.

1.5-2 Nakano T., *et al., Nucl. Fusion* **46**, 626 (2006).

1.5-3 Kubo H., *et al., Proc. 21st IAEA Conf. on Fusion Energy 2006 (Chengdu 2006)* CD-ROM file EX/P4-11.

1.5-4 Nakano T., *et al.*, *Proc. 21st IAEA Conf. on Fusion Energy 2006 (Chengdu 2006)* CD-ROM file EX/P4-19.

1.5-5 Fujimoto K., *et al.*, *Trans. Fusion. Sci. Tech.* **51**, 247 (2007).

1.5-6 Fujimoto K., *et al.*, *Plasma Fusion Res.* "*Modification of Tomography Technique for Two-dimensional Spectroscopic Measurement in JT-60U Divertor Plasmas"*(in press).

1.5-7 Nakano T., *et al.*, *Nucl. Fusion* **42**, 689 (2002).

1.5-8 Nakano, T., *et al., 32nd EPS Plasma Physics Conference (Tarragona, 2005)* CD-ROM file P-5.007.

1.5-9 Asakura, N., *et al., Proc of workshop on Dusts in fusion plasma* (*Warsaw*, 2007).

1.5-10 Kawashima, H., et al., *Plasma Phys. Control. Fusion* **49,** S77-S85 (2007).

1.5-11 Ueda, Y., *et al.*, *J. Nucl. Mater.* **363-365,** 66 (2007).

1.5-12 Krieger, K., *et al., J. Nucl. Mater.* **241-243,** 734 (1997).

1.5-13 Ishimoto, Y., *et al., J. Nucl. Mater.," Transport studies of carbon impurities using 13CH4 gas puffing in JT-60U"* to be published.

1.5-14 Nobuta, Y. et al., *Proc. 34th EPS Plasma. Phys. Conf.,(Warsaw, 2007)* CD-ROM file P024.

1.5-15 Hirohata, Y., et al., *J. Nucl. Mater.*, 363-365 854 (2007).

1.5-16 Masaki, K., et al., *Proc. 21st IAEA Conf., on Fusion Energy 2006 (Chengdu 2006)* CD-ROM file EX/P4-14.

2. Operation and Machine Improvements

2.1 Tokamak Machine

2.1.1 Development of pellet injector using the screw type pellet extruder

In order to extend the operation regime to high density, new pellet injector has been developed for longer duration and high frequency. In the previous pellet injector with a piston type extruder, the frequency and time of injection are limited by extrusion speed and pellet extruder. So, in order to produce pellets continuously, the pellet injector using the screw type extruder has been developed. After the extruder is modified from piston type to screw type, the production of ice rod has been tested. The continuous pellet extrusion up to 330 sec was achieved using the screw extruder. Figure I.2.1-1 shows the photograph of continuous production of pellet. In future, after the design for vacuum and heat insulation the necessary modification for production of good quality ice rod and test will be done.

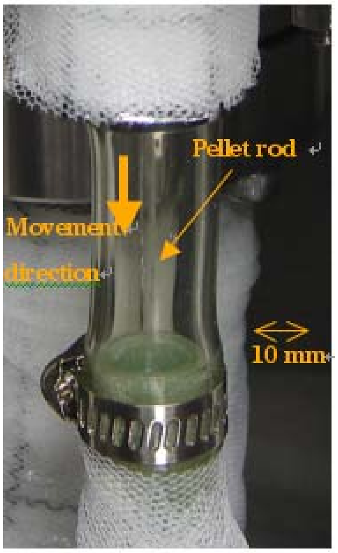

Fig. I.2.1-1 Photograph of pellet injector.

2.1-2 Development of secondary cooling system using the filter

A purpose of the secondary cooling system is removal of the heat in the systems of torus, power supply, heating device etc by circulating water. A floating body is contaminated in the circulating water. In order to remove a floating body in cooling water, a sand filer is used. The floating body attached to the sand in the bath. The sand is washed by much water and medicine periodically (three times per week in JT-60 operation period). The expensive medicine is needed to keep the quality of the water. Since running cost using sand filter is expensive, the new filter method is introduced. The filter is washed automatically in the new method. The schematic diagram of the new method is shown in Fig. I.2.1-2. The filter consists of a screen mesh which is no replacement. When the clog is happened and difference pressure become bigger than the threshold value, the filter is washed. Amount of needed water in the case of screen mesh is one sixth of the water compared with that in the case of sand filter. Moreover, the expensive medicine is not needed; it is expected to reduce the running cost.

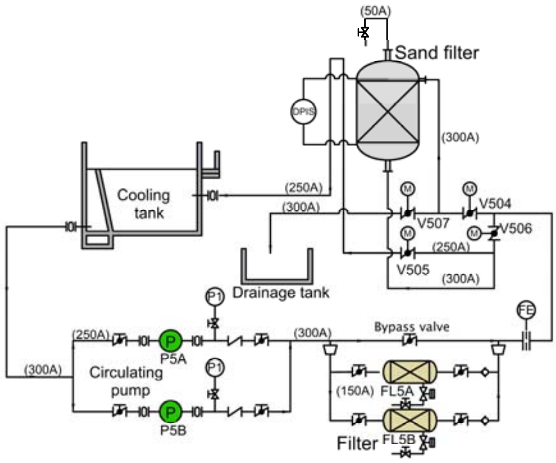

Fig. I.2.1-2 Schematic diagram of the cooling system using the filter.

2.1-3 Dropout of the tiles

The carbon tiles were installed in order to guard the vacuum vessel. The carbon tiles in the divertor outer dome were dropped on 16th June in 2006. The cause of dropout is that heat from plasma flowed the tiles in divertor outer dome. The heat was concentrated to the bolt and nut that is concentrated between the tile and the basement of tile. The nut was melted by the heat flow and the tile was dropped.

The heat per shot was estimated to be 0.12~0.3MJ and the temperature increment is estimated to be 150°C -370°C by taking account of heat ratio between in and out divertor and heat ratio between divertor and dome. Since the temperature can be estimated to be increased to be 1400°C by continuous 3-7 shots, the ferritic steel tiles may be melted.

We take measures against the melting bolt. In order to escape the heat, the carbon sheets will be inserted between tile and the basement that will be made newly. The carbon sheets also give the good heat contact between basement and tile.

The looseness of bolt and melting were checked in all ferritic steel tiles (total 1122 tiles). The looseness of bolt or melting was found in 45 the ferritic steel tiles. Especially many ferritic steel tiles near the horizontal port were found.

2.2 Control System

2.2.1 Real-time feedback control of plasma current using CCS

In the plasma operation, an abnormal plasma shape control occurred during plasma discharge due to abruptly drift error of integral result of magnetic sensors, especially rogowskii coil for plasma current calculation. We have carried out the repetition test to check the drift error phenomenon in integrator. From the impulse noise test result using the noise simulator, the cause of the drift error of integrator is considered the noise from AC power supply line or grounding.

Plasma current is precisely calculated by the line integral of magnetic field along closed line enclosing a plasma on the CCS (Cauchy-Condition Surface) computer system. For the realization of precise plasma current measurement, we have developed a new plasma current calculation formula using the CCS method [2.2-1] in real-time feedback control. High accuracy plasma shape and position control have been achieved using a plasma current of the CCS method in the plasma operation. Therefore, it is possible to measure a plasma current without measurement of rogowskii coil.

2.2.2 Development of the Java-based Human Interfacing System for Remote Experiments

ITER remote experiment is planned to be tested by using JT-60SA at Japanese remote experiment center (REC, Rokkasho-mura, Aomori-ken, Japan) as a part of the ITER-BA project. Functions required for JT-60SA remote experiment are monitoring of discharge sequence status, handling of discharge parameter, checking of experiment data, and monitoring of plant data which is same as the existing JT-60 Human Interfacing System (HIFS). The HIFS is now exclusive to the on-site user in NAKA site due to network safety.

To realize remote experiment of JT-60SA, some functions should be executed from the REC via the Internet. However, the existing JT-60 HIFS functions have been designed only for on-site use for network security reasons. Therefore, we have developed the Java-based HIFS using Java language for remote experiments. Fig. I.2.2-1 shows the HIFS overview for JT-60SA remote experiments. In this system configuration, newly introduced remote experiment server (RES) is connected to the existing JT-60 site-wide LAN, and supervises both of Java application and server application software. A Java application program which is stored in RES is automatically downloaded and executed in users PC when it is selected by user through RES web home page. In this case, a Java application is called as a "Java applet".

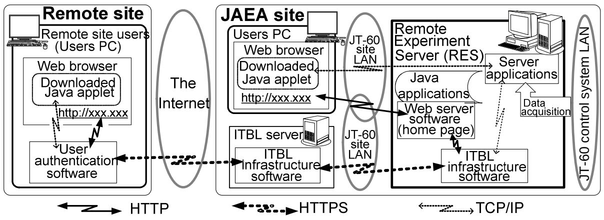

Fig. I.2.2-1 Overview of the HIFS for remote experiment

JT-60 on-site users can use the HIFS for remote experiment by direct access to the web home page of RES from the web browser of individual users PC. The same HIFS environments are provided for the remote site users by connecting to the ITBL server via the Internet. Authentication program installation approval by JAEA is required for the remote site users to connect ITBL (Internet Technology Based Laboratory) server. The combination of Java-based software and ITBL has improved remote site experimental environment to the same level as JT-60 on-site.

New Java-based HIFS was successfully demonstrated in JT-60 remote experiments from Kyoto University in 2006.

2.2.3 Development of the Supervisory Discharge Operation Monitoring System

For safety and efficient operation of a fusion device, appropriate information should be provided to the personnels participating in the experiment. As the first step along this requirement, we have newly developed highlight screens showing the plasma movie, the status of discharge sequence, the discharge schedule, the present status of trouble, etc., on the large (65 inch) monitor TV in front of the central consoles. These screens are automatically switched over according to the timing signal of JT-60 discharge sequence and/or the operator's request. This system is composed of two systems: The new real-time plasma visualization system (RVS) [2.2-2] and the discharge information management system (DIMS). We call this system the supervisory discharge operation monitoring (SDOM) system.

Hardware configuration of SDOM is illustrated in Fig. I.2.2-2. While executing the discharge experiment, the discharge information (highlight screen) which was provided to the personnel related to experiment was outputted by SDOM with the large monitor TV in front of the central consoles. These highlight screens can be seen with the television at the room in addition to the JT-60 central control room.

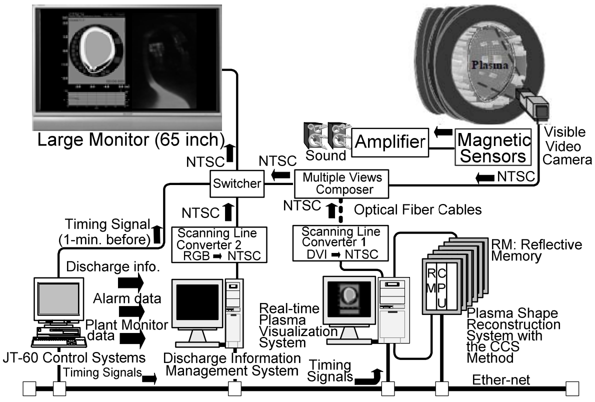

Fig. I.2.2-2 Hardware configuration of the supervisory discharge operation monitoring system

The highlight screens displayed by SDOM have been supported four: (1) the latest discharge parameter and schedule, (2) the JT-60 manager's information, (3) the status of discharge sequence, and (4) the real-time plasma movie. DIMS collects the necessary information from the JT-60 control system, and automatically changes into highlight screens according to the timing signal of JT-60 discharge sequence and/or the session leader's request as shown in Fig. I.2.2-3. This system was developed using the latest JAVA language with only one personal computer. Each element is briefly explained below.

1) The latest discharge parameter and schedule

SDOM shows the highlight screen which is the latest discharge parameter and schedule.

2) The manager's information

If SDOM receives the JT-60 session leader's request, this system outputs the characters which are inputted at the center of screen.

3) The status of discharge sequence

When the “discharge sequence start" signal is received, this system change into the highlight screen which is the status of discharge sequence. This screen is shown until this system receives the "One minute before discharge" signal.

4) The real-time plasma movie

When the switcher receives the “One minute before discharge" signal, it changes into the highlight screen which is the real-time plasma movie. The plasma movie is composed of video camera picture looking at a plasma, plasma shape computer graphic (CG), and magnetic probe signal as a sound channel. A plasma shape CG is calculated in every 1 ms using the shape reconstruction method (the CCS (Cauchy-Condition Surface) method) by the plasma shape reconstruction system.

For the development of the SDOM system, JT-60 is able to execute the experiment on safety and efficient operation, and the physicist can do the latest discharge analysis quickly. Since this system was developed using the JAVA language, it can easily add the function according to the various requests in the future.

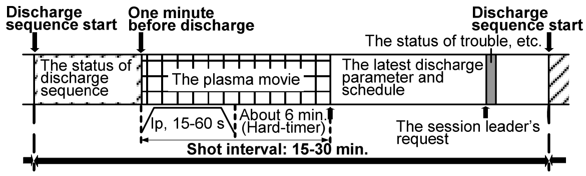

Fig. I.2.2-3The time schedule of the discharge information management system

References

2.2-1 Kurihara, K., *Fusion. Eng. Des.* **51-52**, 1049 (2000).

2.2-2 Sueoka, M., *et al.*, “The Plasma Movie Database System for JT-60,” *Fusion Eng. Des.*, (2007) to be published.

2.3 Power Supply System

2.3.1 Operational Experience

Annual inspections and regular maintenances for the power supply systems have been conducted to maintain availability of high power operations as shown in Table I.2.3-1. In addition, the renewals and maintenances for the power supply systems have also been conducted as measures for the superannuated power supply systems. These renewals and maintenances are shown in Table I.2.3-2. These activities contributed to achieve safe operation of the power supplies.

Table I.2.3-1 Annual inspections and regular maintenances of the power supply systems.

Item	Term
Regular inspection of the Toroidal Field Coil Power Supply(TFPS)	January~ March
Regular inspection of the Poloidal Field Coil Power Supply(PFPS)	January~ February
Regular inspection of the Grounding systems	December~ January
Regular inspection of the Lightning systems	October
Regular inspection of the Power Distribution Systems	October~ November

However, a few troubles of the power supply systems have happened in JT-60 plasma experiment. As an example, trouble of the phase controller for the thyristor converter of the PFPS is mentioned.

In plasma discharge operation on 21st, August, 2006, current unbalance (61D7V) among thyristor converters PSV22A of vertical field coil power supply occurred in initial coil current energizing period. Figure I.2.3-1 shows the circuit configuration of PSV2. 61D7V is to detect current unbalance of 1.09kA in 100ms between 25% of current value measured by DCCT2V for PSV2 total current and measured value by DCCT for PSV22A current. As the reason of the current unbalance, it was found that a print board of digital phase controller to control the timing to trigger thyristor gate of PSV21C had fault in its output pulse for triggering. As the fault caused that PSV21C was operated to output reverse voltage, which was negative voltage to cancel out by chance the positive voltage output by normally operated PSV22A, any current did not flow through PSV21C and PSV22A. The print board in fault was exchanged for a spare print board with checking normal output pulse for triggering. It was found that the data processing ROM on the print board in fault, which is to output pulse for triggering, was damaged by aging deterioration in use.

Table I.2.3-2 Renewals and maintenances as measures for the superannuation of power supply systems.

Item	Term
Change of valves of diode rectifiers cooling system for TFPS	May
Renewal of light guide transmitter/receiver modules of the monitoring system for TFPS	June
Renewal of flow meter for TFPS Motor Generator	February~ March
Inspection and Maintenance of the vacuum current breakers (VCB) for PFPS	March
Change of lubricating oil for the Motor Generator for Additional Heating Facilities	March
Inspection of LRH flow meter for the Power Supply for Additional Heating Facilities	February
Inspection of metal enclosed switchgears (M/C) for TFPS, PFPS and the Power Supply for Additional Heating Facilities	February~ March
Inspection of transformers for TFPS, PFPS and the Power Supply for Additional Heating Facilities	January~ February
Inspection of insulated oil of transformers for TFPS, PFPS and the Power Supply for Additional Heating Facilities	November ~ December

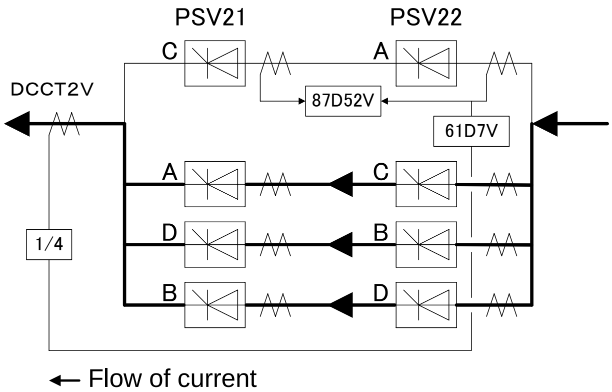

Fig.I.2.3-1 PSV2 circuit configuration

2.3.2 Trouble Report of Thyristor Converter Control in the Long-pulse Operation

In coil energizing operation on 17th, April, 2006, thyristor element failure of thyristor converter PSF1 occurred. The reason of the failure was that the rapid fuse, which is to protect the corresponding thyristor element against over current etc, was blown out. The ratings of rapid fuse are 2100V, 800A and $I^2t=4\times10^6A^2s$, and the circuit configuration of PSF is shown in Fig. I.2.3-2.

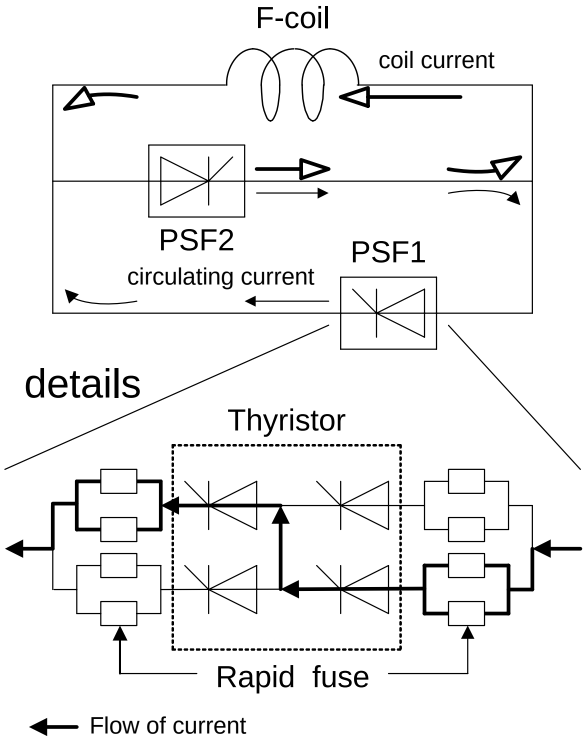

Fig.I.2.3-2 PSF circuit configuration

The current waveform with the PSF1 thyristor element failure is shown in Fig. I.2.3-3. The failure occurred just before current-zero of PSF1 with terminating circulating current control. And also, the enlarged current waveform shows that the current rose again up to 32kA in 90ms and that the rising current included swinging part which had the frequency equal to that of primary side AC voltage of thyristor converter PSF1. As the result, it would be possible that the corresponding thyristor element kept conducting condition whereas PSF1 terminated circulating current control. Therefore, PSF2 was short-circuited equivalently and large current flowed through PSF1 resulting in rapid fuse being blown out. I^2t value of one rapid fuse of PSF1 in the failure is estimated as $7.5\times10^6 A^2s$, which exceeds the rated value of $4\times10^6 A^2s$. Thyristor element kept conducting condition because circulating current control was terminated without sufficient reverse voltage to turn off thyristor. To supply sufficient reverse voltage on thyristor in circulating current control, the current level to terminate circulating current control of PSF has been lowered.

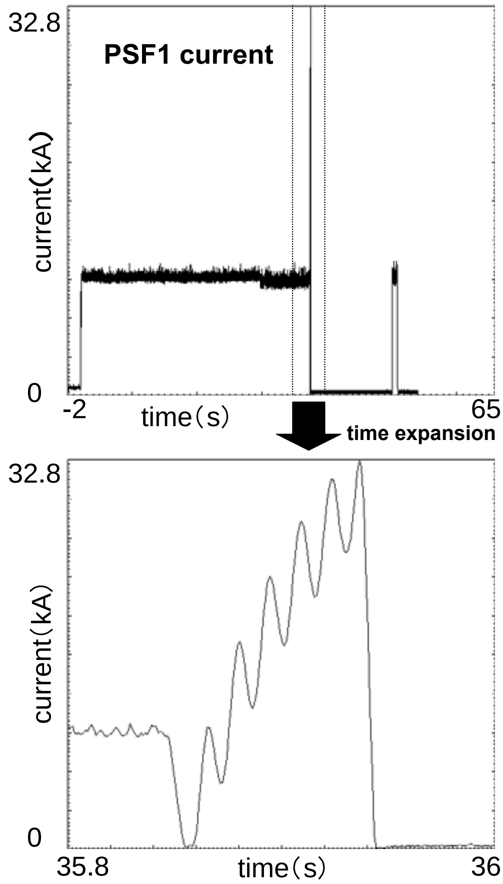

Fig.I.2.3-3 PSF1 current wave pattern

2.4 Neutral Beam Injection System

2.4.1 Long pulse operation of N-NBI system

The negative-ion-based NBI unit was originally designed to inject 10 MW D^0 beams for 10 s using two large negative ion sources, each of which is designed to produce 22 A, 500 keV D^- ion beams. In the campaign of 2006, the beam pulse length is strongly required to be extended up to 30 s in order to study quasi-steady state plasma in JT-60U. The estimation of the power supply capacity indicated that the injected beam power was limited to be < 4 MW for the injection time of 30 s. Under this limitation, a long pulse injection of the neutral beams was carried out by clarifying operational ranges for a stable voltage holding capability and an allowable grid power loading in the JT-60 negative ion source.

To choose the stable acceleration voltage for the long pulse injection, a correlation between the voltage holding capability and a light intensity of cathode luminescence from the Fiber Reinforced Plastic insulator was carefully examined. As the result, the stable voltage holding capability without the beam acceleration was < 420 kV where the light was sufficiently suppressed [2.4-1]. Since the stable acceleration voltage with beam acceleration was 70-80% of that without the beam acceleration, 320kV-340 kV was chosen as the beam acceleration voltage (V_{acc}) .

To attain the beam pulse length of > 30 s, the grid power loading should be reduced to < 1 MW where the surface temperature of the grid is calculated to be lower than the re-crystallization temperature (250 ^{o}C) of the grid material (oxygen-free cooper). The extraction voltage (V_{ext}) and the arc power (P_{arc}) were tuned to minimize the grid power loading while the injection power was maximized. At V_{acc}=320 kV, V_{ext}=5.5 kV and P_{arc}=180 kW, the maximum grid power loading was on the grounded grid, and was allowable level of 650 kW. The D^- ion beams of 30 A were produced with two ion sources and neutralized to 3.2 MW D^0 beams by a gas neutralizer.

The pulse length of 3.2 MW D^0 beam was extended step by step, and finally reached up to 21 s as shown in Fig.I.2.4-1. This is the first long pulse injection of > 20 s in a power range of > 3 MW [2.4-2]. The achieved pulse length was limited by the surface temperature of the beam scraper made of molybdenum without water cooling. The beam pulse length is to be further extended by increasing the interlock level.

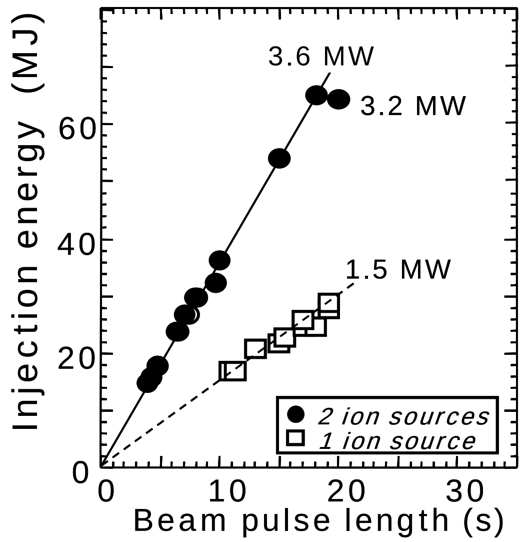

Fig.I.2.4-1 Injection energy as a function of beam pulse length

2.4.2 Operation of P-NBI system

In addition to N-NBI unit, 11 positive-ion-based NBI units, each of which has the capability of 2 MW, 10-s D^0 injections, were modified to achieve the 30-s injection. Four tangential units were upgraded by mainly increasing the capacity of the power supplies so as to extend the injection time from 10 s to 30 s while the beam injection power was kept to be 2 MW. Using these tangential units, 30-s injection was demonstrated at a total injection power of 8 MW. For 7 perpendicular units, injection timing of each unit were optimized to maximize the injection power for the 30-s pulse. In 2006, by using the modified tangential units and the perpendicular units, ~ 800 shots were reliably injected to meet the requirements of plasma physics. This significantly contributed to the study on quasi-steady state plasmas in JT-60U.

2.4.3 Design of the NBI system for JT-60SA

The design studies of the power supplies (1), beamline (2) and magnetic shielding against the stray field (3) for JT-60 SA were progressed.

(1) Power supply

For the power supplies in the P-NBI system, the protective characteristics and the thermal capacity of the power supplies were examined. From the curve of the protective characteristic, the allowable acceleration voltage and current are < 86kV and < 55 A for the 100-s injection, respectively. At these acceleration voltage and current, the injected beam power for one unit is 2 MW, which satisfies the design value of JT-60 SA. The design study on the thermal capacity of the power supply shows that the water cooling breeder resistance of the acceleration power should be upgraded to achieve the 100-s injection at 2 MW.

For the power supplies in the N-NBI system, the inverter capacity for switching of the acceleration power supply is required to be upgraded for 100-s injection. Since the present GTO thyristors are not available due to stop of the manufacturing, a combination of present GTO and a new element is newly designed for 100-s operation. The IEGT (injection enhanced gate transistor), whose performance is reaching in the GTO handling power with lower loss, is a candidate for the new element. The R&D of the combination of GTO and IEGT will be done before the construction of the upgraded N-NBI power supply system. Other power supplies are also modified to upgrade their thermal capacities by attaching additional cooling fans and exchanging the circuit breakers for large ones.

(2) Beamline

The modification of the NBI beamline for JT-60SA was studied by a 3-D Computer Aided Design (CAD). The disassembly of the existing NBI system, the possibility for a 0.6 m downward shift of N-NBI beamline, and possibility for the connection of the existing P-NBI unit with cryostat in JT-60SA were urgently examined in this year.

For the disassembly, while the number of the removed components was minimized, the cost-effective disassembly procedure was proposed. The 0.6 m downward shift of the N-NBI unit can be realized only by newly manufacturing the shorter support structures for the N-NBI beamline. For the connection of the exiting P-NBI unit with cryostat in JT-60SA, the existing beamline of the P-NBI unit can be connected by newly manufacturing shorter drift duct without significant modification of the beamline

(3) Magnetic shielding against stray field

In JT-60SA, the maximum plasma current is designed to be 5.5MA, where the stray magnetic field from the reactor at the exit of the neutralizer cell on the perpendicular P-NBI unit is about 0.1 T. This is about three times larger than that in existing JT-60U. The present NBI system has canceling coils and a double-layer passive shield that is composed of mild steel as an outer layer and μ-metal as an inner one. To reduce the stray field less than ~0.03 mT on the perpendicular P-NBI unit, a canceling coil is additionally designed. It is also designed that the thickness of the outer passive shield is also increased

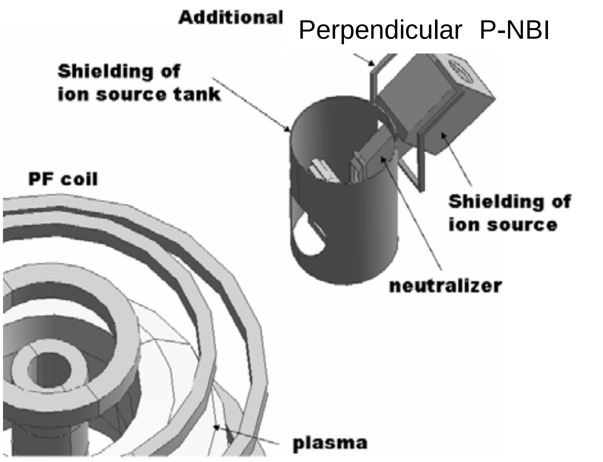

Fig. I.2.4-2 Magnetic shielding of the perpendicular P-NBI

from 2.6 cm to 10 cm. The beam simulation code shows that the beam deflection is about 3 mrad at the exit of the neutralizer cell, which allows the beam transmission to be the same level as that in the present P-NBI unit. The magnetic field at the plasma center, disturbed by magnetic shields of one perpendicular P-NBI unit, is estimated to be about 0.06% of that without the magnetic shields of P-NBI unit.

References

2.4-1 Hanada, M., et al., *IEEE Transactions on Dielectrics and Electrical Insulation*, **14**, 3, 2007

2.4-2 Hanada, M., et al., *Proc. of 21st Int. Conf. on Fusion Energy 2006*, IT/2-3Ra (Chengdu , 2006).

2.4-3 Usui, K., et al., "Study on modification of power supply system for long pulse operation on JT-60 positive ion-based NBI", JAEA-Technology 2007-024, 2007 (in Japanese)

2.4-4 Mogaki, K., et al., "Preliminary design of beamline components for JT-60SA NBI heating system", JAEA-Technology 2007-025, 2007 (in Japanese)

2.4-5 Ikeda Y., et al., *Fus. Eng. Des.*, to be published.

2.5 Radio-Frequency Heating System

Performance of the JT-60U radio-frequency (RF) heating system has been constantly improved to extend the parameter region of experiments such as sustainment of high performance plasmas for a few tens seconds. In FY 2006, major improvements of the JT-60U RF heating system were extension of the pulse duration and high frequency power modulation of the electron cyclotron heating (ECH) system and raising the performance of the lower hybrid (LH) system.

2.5.1 Long-Pulse Operation of the ECH System

Pulse duration of the ECH system is being tried to extend to enhance the plasma performance in the recent experiment campaign in JT-60U focusing on long sustainment of high performance plasmas. Improvements of the gyrotron and developments of advanced operation techniques are keys to extend the ECH pulse. A difficulty to the pulse extension was to keep the oscillation condition against decreasing collector (electron beam) current because of cathode cooling by continuous electron emission. The techniques of controlling heater current and anode voltage during the pulse developed by FY2004 [2.5-1] were refined [2.5-2] and pulse duration of 21 s at 0.4 MW (at gyrotron) has been achieved.

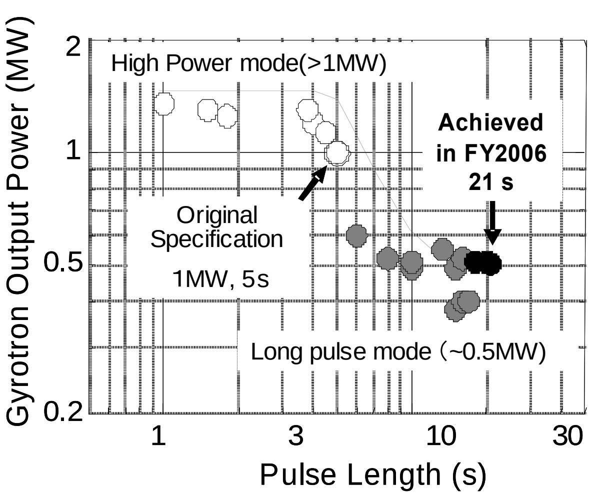

Fig. I.2.5-1 Extension of pulse duration of ECH system

2.5.2 Power modulation test of ECH system

The JT-60U ECH system has a unique feature to realize the power modulation by controlling the anode voltage of the triode gyrotron without chopping the main acceleration voltage. Power modulation operation at relatively low frequencies below 50 Hz was practically used in order to measure heat conductivity of the plasma to investigate plasma confinement. The typical depth of the modulation was 80% at the modulation frequency range of 12.2 Hz to 500 Hz. However in JT-60SA or ITER, higher modulation frequency of ~5 kHz will be required to stabilize neoclassical tearing mode (NTM). As a result of a fine optimization of the anode voltage and impedance of the high voltage circuit, the modulation frequency of 3.5 kHz with the modulation depth of 84 % has been achieved so far in short pulse < 0.06 s. The modulation frequency up to 3 kHz is available in the pulse widths of the practical operation ~ 0.4 s as shown in Fig. I.2.5-2. As a next step, replacement of the parts in the anode voltage divider circuit is planned to achieve higher modulation frequency.

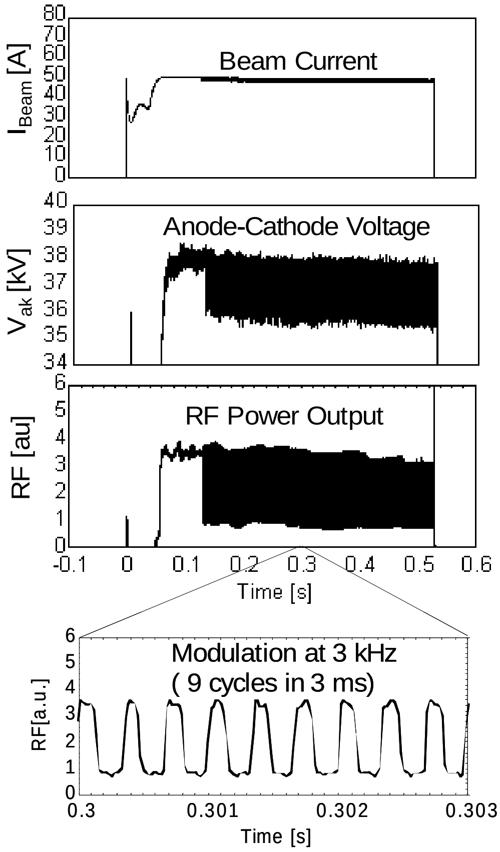

Fig. I.2.5-2 Power modulation at 3 kHz by anode voltage control.

2.5.3 Performance and development of the LH Launcher

LH experiments such as real time control of plasma current profile were performed using LH system, especially with 8-carbon grills around LH launcher mouth since August 2003. After one-year operation, no major damage was observed on the carbon grills itself, on the other hand some base plates as an attachment for the grill were melted. Main cause was malfunction of the arc detector to protect LH antenna mouth at RF breakdowns. Therefore for suppression of damages around LH antenna mouth, checking lump of the arc detector is improved and detecting speed is increased. And a new protection device using CCD-camera is also introduced. The 6-modules without carbon grill are used for LH experiments, stable injections are obtained as 1.1 MW for 20 s (18.64 MJ) in 2006.

On the other hand, to improve insufficient electrical contact along the carbon grill, a new structural carbon grill is developed at a test bench by using "a diffusion bonding method". This new carbon grill is combined with a pedestal made of stainless steel. RF connection point exists between the pedestal and LH launcher mouth. In the RF connection point, a hollow tube type RF contactor has been used instead of a fine spring RF connector, the test module for the new carbon grill shows enough power capability of 0.5 MW - 10 sec at the test bench as shown in Fig. I.2.5-3. This technology will be applicable to the LH launcher in JT-60U.

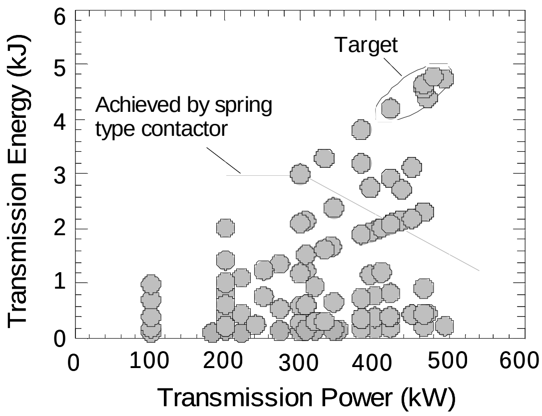

Fig. I.2.5-3 Transmission power test of a new structural carbon grill featuring a “hollow tube type contactor” for LH launcher.

References

2.5-1 Moriyama, S., *et al., Fus. Eng. Des.*, **74**, 343 (2005).

2.5-2 Fujii, T., *et al., J.Phys.: Conference Series*, **25**, 45 (2005) .

2.6 Diagnostics Systems

2.6.1 Modulation CXRS measurement

Profiles of the ion temperature and the plasma rotation have been measured with the significantly high spatial resolution using the new charge exchange spectroscopy (CXRS) system with the space modulation optics, as shown in Fig. I.2.6-1. In this modulation CXRS system, the object lens (f = 20mm) in front of the fiber array is mounted on the Piezo nano-translation stage which has a travel range of 0.5 mm. The observation points are scanned by ± 31mm (corresponding to ± 24mm in radius). The light of the charge exchange line from the other end of the 31ch optical fiber array is led to the entrance of the Czerny-Turner spectrometer with an f = 400mm F2.8 camera lens and a 2160/mm grating. The back illuminated electron multiplying 512 x 512 pixel (16 x 16 μm) CCD camera is used as a detector to achieve a high frame rate, f_{ccd}, up to 400Hz with 16 pixel vertical binning.

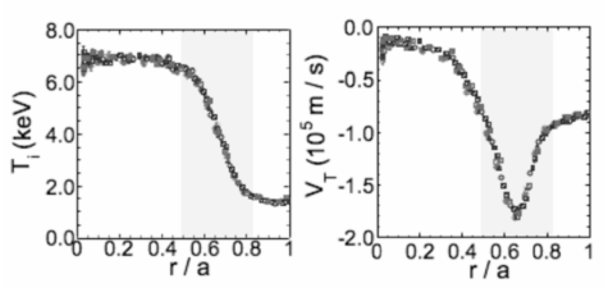

Fig. I.2.6-1 Ion temperature and the plasma rotation profiles, measured by the modulation CXRS system.

The radial points of the measurement can be multiplied by M [$=f_{ccd}$ /(2 f_m)] if the plasma is in the steady state, where f_{ccd} is frame rate of CCD detector of the spectrometer and f_m is a modulation frequency of Piezo stage. By choosing f_{ccd} = 200Hz and f_m = 10Hz, the radial profiles of the ion temperature and the plasma rotation with 310 points are obtained every 50ms.

In order to derive the first and second derivative of the ion temperature from the modulation component of the time evolution of the ion temperature, Fourier analysis technique has been developed [2.6-1]. This technique will provide significant impact in the transport analysis, because the temperature gradient is directly derived. Moreover the radial profiles of the second derivative (curvature) in the region of internal the transport barrier (ITB) are measured with the modulation charge exchange spectroscopy [2.6-2].

2.6.2 Two dimensional spectroscopic measurement of hydrogen emission

In JT-60U divertor plasmas, the deuterium Balmer-series line emission has been measured with a wide-spectral-band spectrometer, which has 92 viewing chords (vertically 60 chords, horizontally 32 chords) with a ~ 1 cm spatial resolution and covers a spectral range of 350 - 800 nm. Two-dimensional spatial distribution of the Balmer line intensities has been reconstructed [2.6-3] using a computer tomography technique (maximum entropy method). It is very important to reduce the false geometric pattern produced in the reconstructed profile as small as possible.

In order to compare the false geometric pattern, (a) the square grid and the experimental view lines (S-E combination), and (b) the parallel grid and the experimental view lines (P-E combination) were applied for the reconstruction of the test profiles. The better results were obtained with the P-E combination than those with the S-E combination. The peak value in the reconstructed profile was 65 % of the test and the normalized error sum of squares, ΔE was 0.50 with the P-E combination, while the peak value was 44 % and ΔE is 0.71 with the S-E combination [2.6-4].

The two dimensional Dγ emission profile, was obtained with the P-E combination for the detached plasma in the inner divertor, as shown in Fig. I.2.6-2.

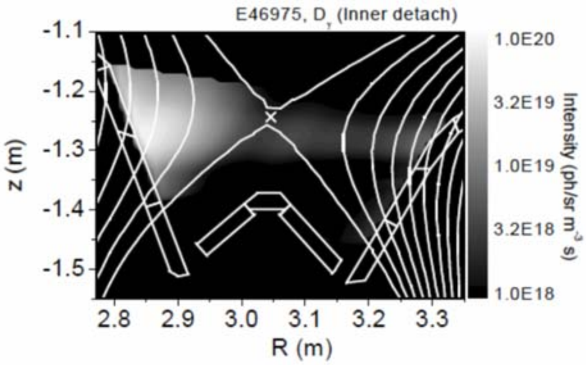

Fig. I.2.6-2 Dγ emission profile reconstructed by the computer tomography with the P-E combination.

2.6.3 Polarization interferometer for Thomson scattering diagnostics

A high-throughput polarization interferometer is being developed to demonstrate the utility of Fourier transform spectroscopy for Thomson scattering diagnostics. Fourier transform spectroscopy is a measurement technique based on measurements of the temporal coherence of a light source. In general, the main advantages of the Fourier spectroscopy are: (1) high throughput optics (i.e. interferometer), (2) improvement of S/N ratio because the interferometer observes the whole wavelength area at the same time. More importantly, for this application, the method can be implemented in a simple and compact.

A prototype of polarization interferometer as the Fourier transform spectrometer was developed as shown in Fig.I.2.6-3. Target T_e and n_e ranges of the prototype polarization interferometer are < 1 keV and > 5×10^{18} m^{-3}, respectively. To compare between the numerical simulation and the experiment, an initial test using a blackbody radiation source was carried out. When the temperature of the blackbody radiation source was changed, the fringe contrast was measured. As a result, the magnitude of the change in fringe contrast agrees with the numerical calculation [2.6-5]. Proof-of-principle tests was carried out in TPE-RX reversed-field pinch (RFP) machine. The electron temperature was successfully measured by the polarization interferometer in TPE-RX PPCD discharges. The temperature of the polarization interferometer nearly agrees with that of the polychromator. The validity of this method was proved for the first time.

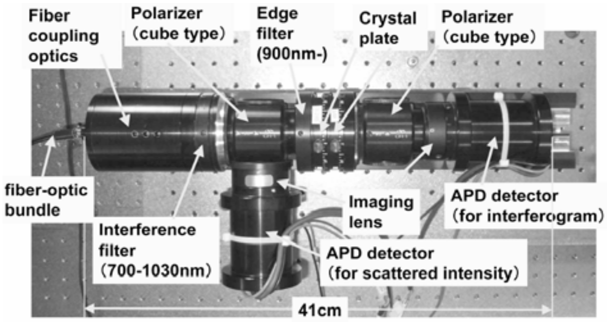

Fig. I.2.6-3 Photograph of the prototype polarization interferometer.

This work is supported in part by Grant-in-Aid for Scientific Researches on Priority Area "Advanced diagnostics for burning plasma" from MEXT (No. 18035016).

2.6.4 Numerical simulation of a lithium ion gun for Zeeman polarimetry on JT-60U

The design target values of the ion gun for Zeeman polarimetry on JT-60U, which will be installed in 2007, are the beam energy of 30 keV, the beam current of 10 mA and the beam divergence angle within 0.13 degrees. The ion gun consists of the ion source, the acceleration electrodes, the electron suppresser, the Einzel lens, the XY deflectors and the neutralizer. Performance of the prototype ion gun has been investigated by using the TriComp beam simulation code (Field Precision), which takes into account of the space charge effects, as shown in Fig. I.2.6-4. Three different initial beam profiles at the ion source are assumed in the simulation, which are peaked, flat and hollow profiles. Each profile is feasible due to the non-uniform beam emission at the ion source, which is caused by the ion source heating characteristics, the extraction field profile, and the coating quality of the b-eucryptite.

The simulation results show the beam loss of 50% caused by the clash to the electrode such as the cathode and the neutralizer. As a whole, the peaked profile has better performance in terms of the beam focusing and efficiency. The beam current about 0.9 mA is obtained at the observation area when the extracted current is 15 mA [2.6-6].

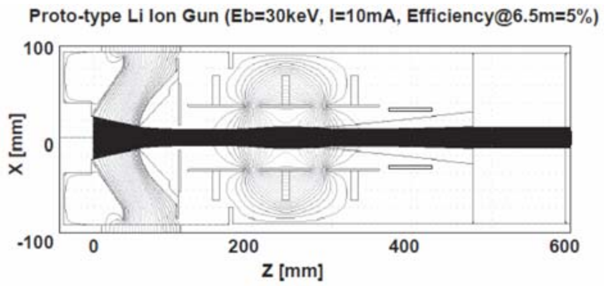

Fig. I.2.6-4 Extraction of Li ion beam.

References

2.6-1 Ida, K., *et al.*, "Measurement of derivative of ion temperature using high spatial resolution charge exchange spectroscopy with space modulation optics, " submitted to *Rev. Sci. Instrum.*

2.6-2 Ida, K., *et al.*, "Transition between internal transport barriers with symmetric and asymmetric curvature of temperature profiles in JT-60U tokamak plasmas, " submitted to *Phys. Rev. Lett.*

2.6-3 Fujimoto, K., *et al.*, *Transactions of Fusion Science and Technology* **51**, 249 (2007).

2.6-4 Fujimoto, K., *et al.,* "Modification of Tomography Technique for Two-dimensional Spectroscopic measurement in JT-60U Divertor Plasmas", to be published in *Plasma Fusion Res. (2007).*

2.6-5 Hatae, T., *et al*., "Development of Polarization Interferometer Based on Fourier Transform Spectroscopy for Thomson Scattering Diagnostics," to be published in *Plasma Fusion Res. (2007).*

2.6-6 Kojima, A., *et al.,* "Numerical Simulation of a High-Brightness Lithium Ion Gun for a Zeeman Polarimetry on JT-60U," to be published in *Plasma Fusion Res. (2007).*

3. Conceptual Design of JT-60SA

3.1 JT-60SA Mission and Program

3.1.1 JT-60SA Project

The JT-60SA project is a combined project of JA-EU Satellite Tokamak Programme under the Broader Approach (BA) Programme and JAEA's programme for national use, with equal exploitation opportunity between the two programmes [3.1-1].

3.1.2 JT-60SA Mission

The mission of the JT-60SA project is to contribute to the early realization of fusion energy by its exploitation to support the exploitation of ITER and research towards DEMO, by addressing key physics issues for ITER and DEMO.

3.1.3 Machine Parameters

A bird's eye view of JT-60SA is shown in Fig. I.3.1-1. Typical parameters of JT-60SA are shown in Table I.3.1-1. The maximum plasma current is 5.5 MA with a relatively low aspect ratio plasma (Rp=3.06 m, A=2.65, κ_{95}=1.76, δ_{95}=0.45) and 3.5 MA for an ITER-shaped plasma (Rp=3.15 m, A=3.1, κ_{95}=1.69, δ_{95}=0.36). Inductive operation with 100s flat top duration will be possible within the total available flux swing of 40 Wb. The heating and current drive system will provide 34 MW of neutral beam injection and 7 MW of ECRF. The divertor target is designed to be water-cooled in order to handle heat fluxes up to15 MW/m^2 for long time durations. An annual neutron budget of $4x10^{21}$ neutrons is foreseen and will be subject to the agreement by the responsible legal authority and local government [3.1-1].

3.1.4 Machine Features

The main features of JT-60SA device are as follows;

- JT-60SA is a fully superconducting tokamak capable of confining break-even equivalent class high-temperature deuterium plasmas.
- JT-60SA allows the exploration of configuration optimization for ITER and DEMO with a wide range of plasma shapes (elongations and triangularities, shape factor $S=q_{95}I_p/(aB_t)$) and aspect ratios ($A=R/a$ down to ~ 2.6) including that of ITER, with the capability to operate in both single and double null configurations.
- JT-60SA allows the exploration of ITER relevant high density plasma regimes well above the H-mode power threshold with 41 MW high power heating, including dominant electron heating by 110&140 GHz ECRF and 500 keV N-NBI.
- JT-60SA allows the study of power and particle handling at 41 MW for 100 s with top and bottom water-cooled divertors compatible with maximum heat flux of 15 MW/m^2.
- JT-60SA allows the exploration of full non-inductive steady-state operation with 10 MW/500 keV tangential

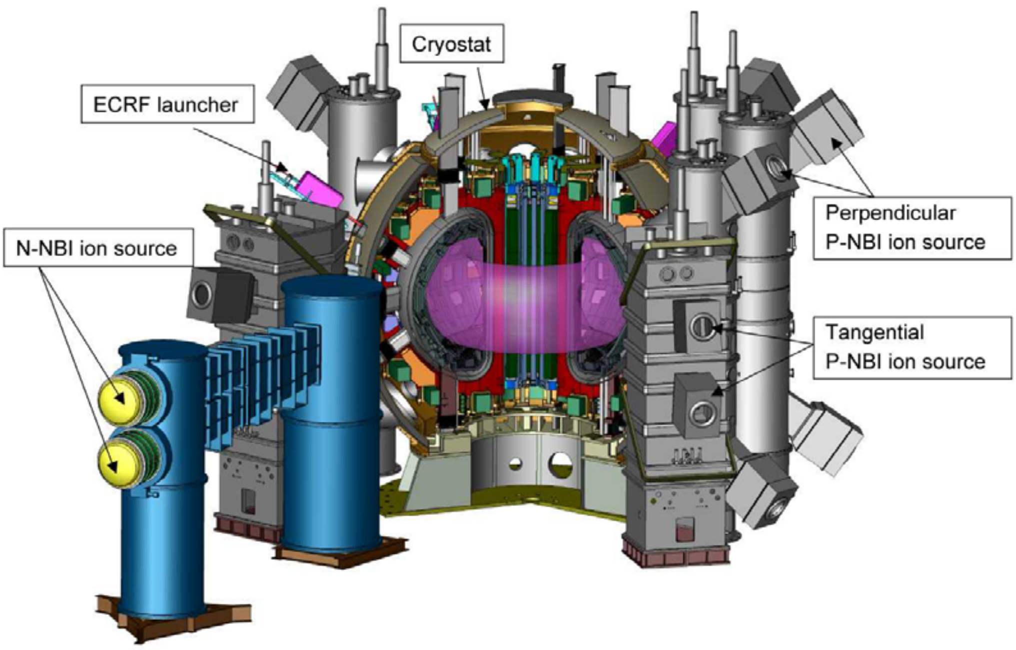

Fig. I.3.1-1 Bird's eye view of JT-60SA tokamak with heating and current drive systems.

NBCD and 7 MW of ECCD.

Table I.3.1-1 Typical Parameters of JT-60SA

Parameter	Low A (DN)	ITER-shape (SN)
Plasma Current, I_p (MA)	5.5	3.5
Toroidal Field, B_t (T)	2.68	2.6
Major Radius (m)	3.06	3.15
Minor Radius (m)	1.15	1.02
Elongation, κ_{95}	1.76	1.69
Triangularity, δ_{95}	0.45	0.36
Aspect Ratio, A	2.66	3.1
Shape Parameter, S	5.5	4.0
Safety Factor, q_{95}	3.1	3.06
Flattop Duration	100 s (including hybrid operation)	
Heating & CD Power	41 MW x 100 s	
NBI	34 MW	
ECRF	7 MW	
Divertor wall load	15 MW/m^2	
Annual neutron yield	4 x 10^{21}	

- JT-60SA allows exploitation of high beta regime with stabilizing shell covered with ferritic plates and internal RWM stabilizing coils and high power H&CD system.
- JT-60SA is equipped with remote handing system to allow maintenance of in-vessel components compatibly with the planned annual neutron yield of 4x10^{21} neutrons/year.

3.1.5 Construction and Operation Schedule

The duration of the Satellite Tokamak Programme will be 10 years, including 3 years for commissioning and operation. The time critical components are the cryostat base and toroidal field coils. Major milestones are start of tokamak assembly in 2011, completion of tokamak assembly early in 2014, and first plasma in 2014.

Reference

3.1-1 Kikuchi, M., et al., *Proc. of the 21st IAEA Fusion Energy Conference (Chengdu, 2006)* CD-ROM file FT/2-5.

3.2 Physics Assessment

Optimization of operational scenarios, such as full current drive (CD) ones, assessment and optimization of MHD controls, for the resistive wall mode (RWM) and the neo-classical tearing mode (NTM), and evaluation of heat/particle handling have progressed [3.1-1, 3.2-1].

3.2.1 Operational Scenario

Optimization of full CD plasmas has progressed [3.1-1, 3.2-1]. A full CD plasma with I_p = 3 MA (B_t = 2.27 T, q_{95} = 5.6, β_N = 3.6, β = 4.2%,. f_{BS} = 0.55) is expected at $\bar{n}_e/n_{GW}$ of 0.58 for H_{H98y2} = 1.33 with total heating power of 41 MW. At this toroidal field, both 110 and 140 GHz ECRF can be absorbed at the second harmonics resonance. Adjusting the injection angles (toroidal and poloidal angles), both 110 and 140 GHz ECRF waves are absorbed at r/a~0.55 and generate EC-driven current of 0.14 MA. A full CD operation with

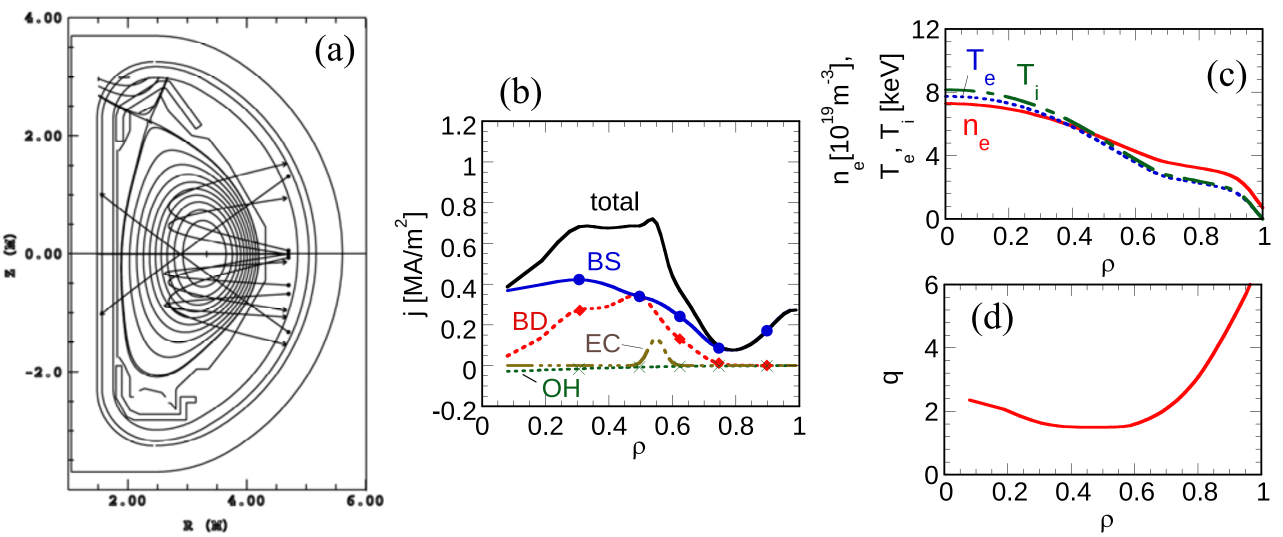

Fig. I.3.2-1 The plasma equilibrium (a), the current profiles (BS, EC, BD, OH and total) (b) and the temperature and the density profiles (c) and the safety factor profile (d) of high density high β_N full-CD plasma.

a higher normalized density of $\bar{n}_e/n_{GW}$ = 0.86 (= 5.0x10^{19} m^{-3}) is expected at I_p = 2.4 MA for H_{H98y2} =1.33 (B_t = 1.82 T, q_{95} = 5.7, β_N = 4.3, β = 4.9%) with 41 MW injection power as well. In this case, the 140 GHz ECRF is absorbed at the third harmonics then does not drive significant current, while the 110 GHz wave is absorbed at the second harmonics resonance. The fraction of the bootstrap current reaches 0.69. The plasma equilibrium, the current profiles (BS, EC, BD, OH and total) and *Te Ti ne* and *q* profiles of this high density high β_N full-CD plasma is shown in Fig. I.3.2-1.

3.2.2 Assessment and Control of MHD

Stabilization of RWM by the sector coils has been analyzed by the VALEN code in collaboration with Columbia University [3.2-1]. The equilibrium parameters are chosen as R_0/a=2.95 m/1.05 m, κ_{95}=1.79, δ_{95} = 0.41, $q_0/q_{95}/q_{min}$ = 4.28/7.52/2.1, $\ell_i(3)$ = 0.63, $p(0)/\langle p(\rho)\rangle$ = 2.77 for the plasma of β_N = 4.5. The result is shown in Fig. I.3.2-2. In the figure, a curve marked with open squared corresponds to the passive stabilization only with the stabilizing plate. And the beta limit is β_N = 3.13. On the other hand, a curve marked with closed circles corresponds to the ideal wall limit. The beta limit is near 4.5. Other three lines correspond to cases with the sector coils feed-back with different three proportional gains. The result indicates that RWM can be stabilized up to β_N = 4.35.

Stabilization of NTM by the ECRF has also been investigated [3.2-1]. It was evaluated in a plasma based on the ITER-like plasma of I_p = 3.5 MA at B_t = 2.4 T with β_N = 1.8 but with reduced density (32% of n_{GW}). The strength of the toroidal field was scanned. In the scan, Ip, ne and Te were changed in order to keep the safety factor, the Greenwald density fraction and β_N. For a simple evaluation, amount of the locally driven EC current was compared to the bootstrap current at the q = 1.5 location, which corresponds to the m/n = 3/2 NTM resonance. It was found that with expected injection power of 3 MW for the 110 GHz ECRF and of 4 MW for the 140 GHz ECRF, the local driven current density exceeds the boot strap current density in a wide range of B_t from 1.6 to 2.4 T. This roughly indicates that the ECRF powers are enough to suppress the m/n = 3/2 NTM in this range of B_t. More detailed analysis using TOPICS at 2.1 T was also carried out. The result indicates that the m/n = 3/2 NTM can be stabilized with less than 2 MW of the 140 GHz ECRF and roughly agrees with the analysis mentioned above.

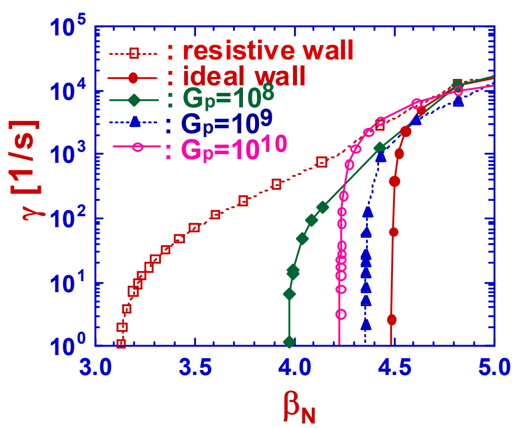

Fig. I.3.2-2 Growth rate versus normalized beta for different proportional gain G_p. A curve with open squares corresponds to the passive stabilization, while a curve with closed circles corresponds to the ideal wall limit. Active feedback and idealized passive structure allows stabilities at β_N = 4.35 for optimum feed-back gain $G_p = 10^9$.

3.2.3 Heat and Particle Control by the ITER like Lower Divertor

JT-60SA has both upper and lower divertors. The lower divertor is planed to be compatible the ITER-like equilibriums and similar to that foreseen in ITER [3.2-1]. That is vertical target plates and a V-shape corner at the outer divertor. Function of this ITER-like divertor has been investigated by the SOLDOR/NEUT-2D code. It is confirmed that with "V-shape corner", a dense plasma that is similar to one obtained without "V-shape corner" but with gas-puff can be formed at the outer divertor. And with "V-shape corner" and gas-puff, detachment can be induced and heat flux to the hit point can be reduced greatly. The results indicate effectiveness of "V-shape corner". It should be noted that another simulation indicates that by increasing X-pint height, attached divertor can be retrieved with the same gas-puff. These results indicate that with "V-shape corner", divertor detachment can be controlled.

Reference

3.2-1 Fujita, T., et al., *Proc. of the 21st IAEA Fusion Energy Conference (Chengdu, 2006)* CD-ROM file FT/P7-4.

3.3 Plant Description

JT-60SA has been designed aiming at the maximum utilization of the existing JT-60 facilities and hardware, such as buildings, plasma heating and current drive systems, some power supplies, diagnostics and cooling systems [3.1-1].

The cross sectional view of the tokamak is shown in Fig. I.3.3-1. A plasma aspect ratio down to about 2.6 was chosen in order to be able to survey optimum plasma shapes in view of the most cost effective DEMO reactor design. The major components of the tokamak will be installed into the inner space of a cryostat that has a diameter of about 14 m. The present design of divertor geometry was optimized to produce both high triangularity double-null/single-null plasmas and ITER-shape single-null plasmas within the same machine. A semi-closed vertical divertor with dome, rather than the ITER divertor configuration, was adopted to keep higher flexibility of plasma shaping capability.

The heating and current drive (H&CD) systems in JT60-SA will allow both power densities in excess of those expected in ITER as well as the capability to independently control heating, current and rotational profiles, a feature deemed as essential in order to be able to expand the understanding of advanced tokamak regimes. The high power plasma heating systems also bring about a substantial increase of the DD neutron yield to about 2×10^{19}/shot. In order to increase the nuclear shielding effectiveness, boric acid water will be introduced into the double walled space of the vacuum vessel. This will help to reduce the nuclear heating in the TF and EF coils under a narrow shielding space constraint. Boron doped concrete will also be filled between the double wall of the cryostat for bio-shielding of the torus hall and prevention of the air activation. Owing to the expected high dose rate inside the vacuum vessel, remote handling system will be necessary, and will be developed for the maintenance and repair of in-vessel components such as divertor modules and first wall.

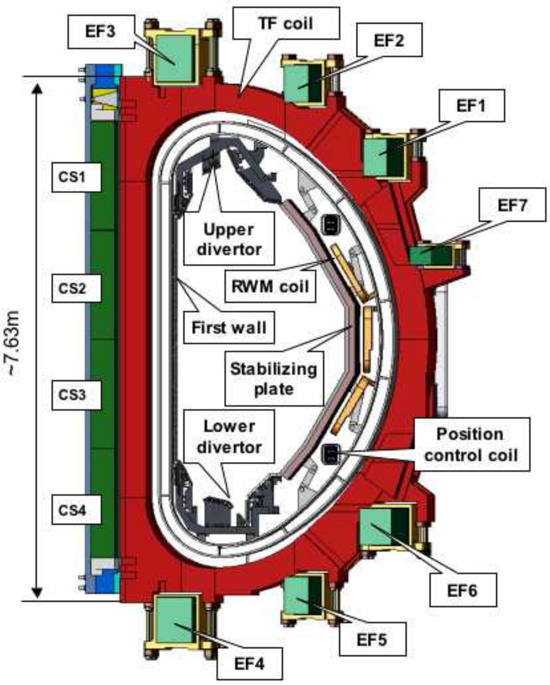

Fig. I.3.3-1 Cross sectional view of the JT-60SA tokamak. TF and PF magnets, vacuum vessel, upper and lower divertors, stabilizing plates, in-vessel position control coils and sector coils for RWM control are shown.

Figure I.3.3-2 shows the layout plan of the JT-60SA torus hall with all the major components. Four large ports have been devoted to remote handling. In addition, four beam towers of perpendicular injection positive ion based NBI (P-NBI), two beam tanks of tangential injection P- NBI, and a negative ion based NBI (N-NBI) located in the assembling hall will be reused. The waveguides of ECRF will be introduced from the upper neighboring room. Current lead boxes, valve boxes and other major equipments will be located nearby the cryostat. Plasma discharge operation is now planned to occur mainly during day time, as the regeneration of the divertor cryo-panels will be required every night in order to cope with plasma high density operation [3.3-1].

3.3.1 Superconducting Magnets

The superconducting magnets in JT-60SA consist of 18 toroidal field (TF) coils and 11 poloidal field (PF) coils, as shown in Fig. I.3.3-1. A NbTi superconducting conductor has been chosen for the TF coils owing to the limited maximum field strength of ~6.4 T. The choice of the final conductor design will be made on the basis of superconducting stability, manufacturing feasibility, optimal compatibility with the power supply, as well as cost.

PF coils consist of the Central Solenoid (CS) made of four identical coils (CS1, CS2, CS3, CS4) and seven equilibrium field (EF) coils (EF1-7). NbTi superconducting conductor has been chosen for all EF coils, including the divertor coils (EF3 and EF4), as

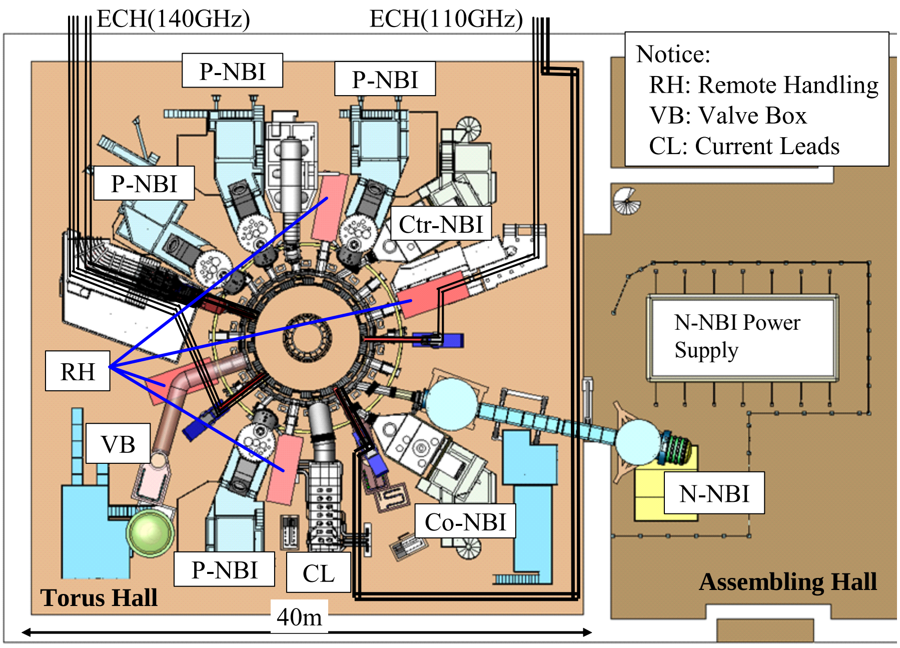

Fig. I.3.3-2 Layout plan of the JT-60SA torus hall.

their maximum field strength at the conductor surface of the EF coils is limited to ~6.2 T. Two kinds of NbTi conductor designs are expected for the EF coils, because the maximum magnetic field strength is quite different between the outer ring EF coils (EF1, EF2, EF5, EF6, EF7) with a large diameter, and the inner ring divertor coils (EF3, EF4).

For the CS a Nb_3Sn conductor has been chosen as a consequence of the maximum field strength (~9 T) needed to ensure a flux swing capability of about 40 Wb - necessary to sustain the flattop period of ~100 s with the rated plasma current of 5.5 MA under hybrid operation.

All TF coils are planned to be cooled down and cold-tested in advance to shipment to verify their functionality. Similar tests are also planned for the CS modules. The Japanese High Pressure Regulation Law will be applied for these superconducting magnets.

3.3.2 Vacuum Vessel

The vacuum vessel (VV) is a torus-shaped and double wall structure. The vacuum vessel is made of double-walled 316L stainless steel with low Co content (less than 0.05 wt%) to minimize induced activation. Filling up of the double-wall vacuum vessel with boric acid water is planned to enhance the neutron shielding capability of the vacuum vessel. A gravity support will be attached every 40 degree section with a pack of spring plates at the bottom of the vacuum vessel. Connecting plates between the neighboring vertical ports and/or gravity supports are introduced to increase the stiffness of the vacuum vessel against the twisting moment and seismic forces.

An 80 K thermal shield will be placed between the vacuum vessel and the cold structures of the superconducting magnets. The baking of the vacuum vessel, at 200°C, will be done by means of heated nitrogen gas. Plasma operation during VV baking is not being planned because the neutron shielding capability would be lost during the baking using nitrogen gas. In addition, it would not acceptable from the view point of the heat load to the cryogenic system. Also it must be taken into account that, during plasma operation, the temperature of in-vessel components such as divertor cassette will be limited to around 60°C.

3.3.3 In-vessel Components Including Divertor Cassette Module

The major in-vessel components of JT-60SA are the divertor cassettes, the inboard first wall, the stabilizing baffle plate, the fast plasma position control coils, and the sector coils for RWMs control.

The upper and lower divertor cassettes are asymmetric to allow ITER-shape plasmas and high triangularity plasmas. In the presently foreseen design, a mono-block type CFC divertor armor will be used for the outboard side to withstand a heat load of ~15 MW/m^2, while a flat tile type divertor armor is usable for the inboard side owing to the smaller expected heat load.

The CFC divertor armor will be connected to the divertor cassette in a way compatible with remote handling requirements. The cryo-pump can be installed behind the divertor cassettes in order to increase the pumping capability. On the basis of divertor performance simulations, the location of the cryo-panels will be finally decided considering the core and SOL plasma performances needed to contribute to the ITER experiments and to DEMO reactor design.

Two in-vessel field coils will be used for fast plasma position control. In order to control vertical and horizontal field at the same time using two coil blocks, independent power supplies will be connected to each coil block. The ampere turn of the fast plasma position control coils is ~80 kAturn**.** To suppress the excessive current and electromagnetic forces during plasma disruptions and VDEs, the insertion of external inductors in series to the coils and power supplies may be required.

The primary function of the stabilizing baffle plate is to enhance the ideal beta limit and to improve plasma positional stability. The stabilizing baffle plates are baked up to 200°C as well as the VV. They have been designed as a double-wall structure made of SS316L and covered with bolted first wall.

The 18 sector coils for the RWM control will be installed around the openings of the stabilizing baffle plate to minimize the control response time. Since each sector coil has its own current leads, the magnetic field mode of m/n = 3/1 or 3/2 can be controlled depending on the configuration of the power supply connections.

3.3.4 Cryostat

The vessel body of the cryostat is a spherical shaped structure of about 14 m diameter. The cryostat vessel has a big top plate shifted up by about 1 m to maximize the inner space for the assembly and maintenance of cryogenic devices such as in-cryostat feeder, insulation break and TF terminal joints. The cryostat vessel is made of double-walled SS304 (Co < 0.05wt%) filled with boron doped concrete. The inner skin has a structure to support the weight of all the ports and to withstand the vacuum pressure. Since the role of the outer skin is just to contain the boron doped concrete, it is much thinner in comparison with the inner skin. Also, thin outer metal skin has the advantage to decrease the activation level outside the cryostat.

Boron will efficiently reduce thermal neutron flux and hence the activation of Ar in the torus hall atmosphere.

The gravity support made of SS304 (Co < 0.05wt%) is designed as a robust structure to support the dead weight of superconducting coils and the VV, including in-vessel components, operational electromagnetic loads, thermal stress during baking and standard operational conditions, and seismic loads.

3.3.5 Remote Handling

The large foreseen annual neutron fluence of ~$4x10^{21}$ neutrons/year will prevent human access inside the vacuum vessel after extensive experimental campaigns. Therefore, most of the in-vessel components will have to be compatible with remote handling requirements. The remote handling system is planned to use a vehicle type system, such as the one adopted in ITER for its shielding blanket. Four large horizontal ports are used to extend and support a rail and bring in/out the maintained components as shown in Fig. I.3.3-2. The functions of the remote handling system of JT-60SA are as follows: repair and exchange of divertor cassettes, repair of first wall for the inboard side and the baffle plates, while in-vessel coils and stabilizing baffle plates are assumed as permanent components. The weight of one divertor cassette is expected to be about 500 kg, while one first wall element is only a few kg. The remote handling system will have two types of headers to handle these two different loads.

Reference

3.3-1 Matsukawa, M., et al., *Proc. of the 21st IAEA Fusion Energy Conference (Chengdu, 2006)* CD-ROM file FT/P7-5.

4. Domestic and International Collaborations

4.1 Domestic Collaboration

JT-60U was assigned as a core national device for joint research by the Nuclear Fusion Working Group of the Special Committee on Basic Issues of the Subdivision on Science in the Science Council of MEXT in January 2003. Using the JT-60 tokamak and other facilities, JAEA has performed research collaboration with the universities and NIFS. Accordingly, the joint experiments on JT-60 between JAEA and the universities by assigning university professionals as leaders of research task forces has been successful. The numbers of collaborators and research subjects had increased significantly since FY 2003 as shown in Fig. I.4.1-1.

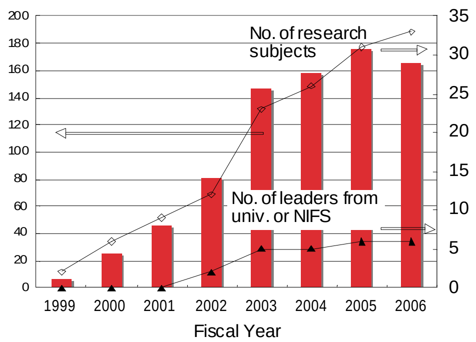

Fig. I.4.1-1 Evolution of the JT-60 joint research.

In FY2006, 165 persons participated, who came from 25 research organs in Japan. Each subtheme is occupied by two leaders, one from university or NIFS and one from JAEA. The number of research subjects of the joint research was in total 33 in FY 2006, categories of which are shown in Table I.4.1-1. Fourteen journal papers and 23 papers in conference proceedings were published as a result of the joint research in FY 2006.

Table I.4.1-1 Number of research subjects of the JT-60 joint research according to category in FY 2006.

Category	No. of research subjects
Performance improvement	2
Transport	5
Pedestal	3
MHD/High energy particles	8
Divertor/SOL	2
Plasma-material interaction	3
Diagnostics	7
Heating system	3
Total	33

4.2 International Collaboration

Status of collaborative research based on the IEA Implementing Agreement on cooperation on the Large Tokamak Facilities is described, following the annual progress report 2006 of the executive committee, which was presented at the 36th Meeting of the Fusion Power Coordinating Committee on Feb 27-28, 2007. This report covers from June 2005 to June 2006. In this period, there were personnel exchanges among the three Parties. The number of personnel exchanges, to which JAEA relates, is 8 in total. 3 personnel exchanges are from JAEA to EU, 1 from EU to JAEA, 0 from JAEA to US, and 4 from US to JAEA.

The exchanges from EU relate to the pedestal study titled "Participation to JET Ripple Experiments". After installation of ferritic steel tiles (FSTs) in JT-60U to reduce the toroidal field ripple, an improvement of pedestal performance was observed using large plasma configuration, where the ripple amplitude without FSTs was ~2%. In addition to this, previous JET/JT-60U similarity experiments indicated that the level of ripple amplitude is one of the differences between two devices. Therefore, to investigate in detail the role of toroidal field ripple on pedestal energy and ELM characteristics as well as the study of rotation effects, the "TF ripple campaign" including dedicated experiments using matched shape to the JT-60U plasma cross section was performed in JET with participations of N. Oyama and H. Urano. When the ripple amplitude increased, the pedestal density tends to decrease as well as the reduction of toroidal plasma rotation in co-direction to the plasma current. The change in the ELM characteristics was more obvious, where ELM frequency become higher as ripple amplitude increased and/or co-toroidal rotation decreased. This result is qualitatively similar to JT-60U. Detailed analysis is underway for the explanation of difference of pedestal structure between two devices.

The exchanges from US relate to the NNBI study titled “Experiments on negative ion systems”**.** Dr. Grisham made three trips to collaborate with the JT-60U negative ion beam group during the period covered by this agreement. During this period, this collaboration was primarily engaged in developing techniques to more reliably steer the many beamlets which comprise a beam, and in finding ways to compress the beam envelope. This will be incorporated into the upgraded accelerators for JT-60SA, and will be essential in designing the ITER beam accelerators. We also studied processes precipitating breakdown in the accelerator column, and the evolution of oxygen contamination in the source plasma.

From April 2006 to March 2007, 4 papers were published in journals and 3 papers in conference proceedings, as a result of the IEA Cooperation among Large Tokamak Facilities related to JT-60U.

II. THEORY AND ANALYSIS

Much progress was made in the analysis of ITB events and their triggers, plasma shape effect on edge stability, and driven magnetic island evolution in rotating plasmas. Progress was also made on the physics of X-point MARFE formation and dynamics, and on the modeling of divertor plasma after an ELM crash. Integrated simulation models of core, edge-pedestal, scrape-off-layer and divertors have been developed based on JT-60U experiments and first-principle simulations; the simulation succeeded in clarifying complex features of reactor-relevant plasmas. In the NEXT project, computer simulations were progressed on the plasma turbulence. Self-organization process of ETG turbulence is shown based on the first principle gyrokinetic model. The dependence of GAM region on the device size was investigated for the Global ITG turbulence. Statistical characteristics of ETG turbulent transport were also investigated in the slab gyro-fluid model. Cross section data for atomic and molecular collisions and spectral data relevant to fusion research have been produced, compiled and collected.

1. Confinement and Transport

Non-local transport bifurcations inside and around ITB (abrupt variations of transport in a ms timescale within 30-40% of minor radius) were found in various JT-60U reverse shear (RS) and normal shear (NrS) plasmas and called ITB-events. In low-power heated RS plasmas, ITB-events are observed at the crossing of q_{min}=3.5, 3, 2.5 values. Internal MHD n=1 activity has been reported earlier as ITB-events trigger. The present study shows the new MHD triggers of ITB-events in JT-60U. ITB-event is triggered by a series of small internal disruptions probably associated with q=2.5 surface in RS plasmas. ITB-event occurs in a ms timescale correlation with the start of ELMs series in high-β_p NrS shot. The total heat flux reduces abruptly in the zone 0.3<r/a<0.7 (by 3 times at the reduction maximum). The calculated radial electric field (with assumed neoclassical poloidal rotation) changes little at the ITB-event. The ms correlation between the start of ELMs series and the reduction of the heat flux gives possibility to control the ITB formation immediately and non-locally by inducing the ELM-like MHD activity.

We compare various types of instantaneous edge-core and core-edge interplay and transport bifurcations, which are illustrated in Fig. II.1-1. For all the cases we consider variations of transport occurred in a ms timescale. (a) At the time of global L-H transition, the transport coefficient is reduced instantaneously in the wide zone 0.3 <r/a<1. In RS and NrS shots with weak ITB, the reduction covers the zone of the ITB also. (b) Global L-H transition is sometimes triggered by a sawtooth crash. (c) ITB-event-improvements without trigger or with small internal MHD activity as a trigger are observed. (d) Similarly to the sawtooth crash, the ITB-event degradation can induce the L-H transition. (e) ITB-event occurs with external MHD as a trigger. (f) Central ITB-event is found for the off-axis ECRH cut-off in T-10, and the abrupt reduction of transport triggered by evaporation of small C_8H_8 pellet is found in LHD [1-1].

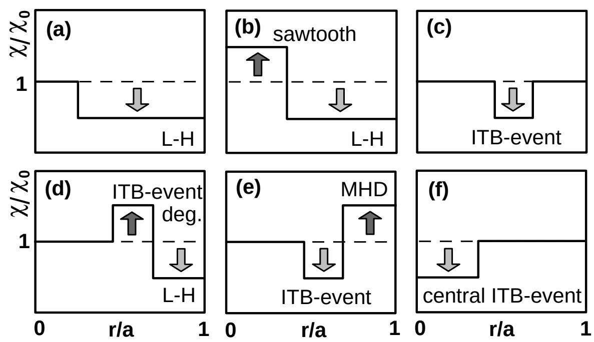

Fig. II.1-1 Cartoon view of transport variations.

Reference

1-1. Neudatchin, S.V., *et al*, *Proc. 21st IAEA Conf. Fusion Energy 2006*, CD-ROM IAEA-CN-149 (IAEA, Vienna, 2007) file EX/P1-8.

2. MHD Stability

2.1 Effect of the Plasma Shape on the Stability of Tokamak Edge Plasmas

We have introduced the new plasma shaping parameter 'sharpness' as $\sigma=(1/r_c)/(1/a)$, where r_c is the radius of the circle of curvature at the top or the bottom of the equilibrium and a is the plasma minor radius, and identify the effect of the shape at the top or the bottom of the equilibrium on the stability of tokamak edge plasma. The stability of an infinite-n ballooning mode and finite-n ideal MHD modes, whose n number is from 1 to 30, are analyzed numerically, where n is the toroidal mode number. Fig.II.2.1-1 shows (a) magnetic surfaces of the three kinds of equilibria whose σ_{up}=5.66, 3.19, 1.75 and (b) stability diagram of the different σ_{up} equilibria on the s-α plane at ψ_N=0.96. Here s is the magnetic shear defined as $s=r(dq/dr)/q$, r is the minor radius of each magnetic surface, q is the safety factor, α is the normalized pressure gradient defined as $\alpha=-2\mu_0 Rq^2(dp/dr)/B^2$, μ_0 is the permeability in the vacuum, R is the major radius, p is the pressure, B is the magnetic field, and ψ_N is the normalized poloidal flux. The stability limit of the pressure gradient becomes larger from 3.22 (σ_{up}=1.75) to 3.65 (3.19) and 4.38 (5.66) as σ_{up} increases. The result of this analysis have showed that the increase of the sharpness stabilizes the ballooning mode and the peeling-ballooning mode, though a current driven kink (peeling) mode is hardly stabilized. This stabilizing effect of the sharpness has an impact on the stability of the pressure driven ballooning mode mainly through multiplying the local shear near the top or the bottom of the equilibrium. These results have revealed that the plasma pressure at the pedestal can be improved by increasing the sharpness; in other words, the sharpness is an important factor for an H-mode operation with a high confinement performance [2.1-1].

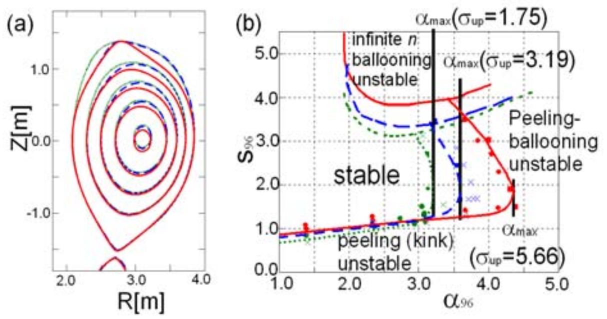

Fig. II.2.1-1 (a): Magnetic surfaces of the three kinds of equilibria whose σ_{up}=5.66 (solid line), 3.19 (broken line), 1.75 (dotted line). (b): Stability diagram of the different σ_{up} equilibria on the s-α plane at ψ_N=0.96.

Reference

2.1-1 Aiba, N., *et al.*, *Nucl. Fusion*, **47**, 297 (2007).

2.2 Rapid Evolution and Deformation of Magnetic Islands in Rotating Plasmas

Nonlinear numerical simulations based on the resistive reduced MHD model revealed novel features of the rapid growth and the nonlinear dynamics of driven magnetic islands in rotating plasmas. Between the rapid growth phase and the Rutherford-like phase, which are already known, the transition phase of the magnetic island evolution is found in the low resistivity regime. In the rapid growth phase, the X- and O-points of the magnetic island move in the poloidal direction with the different speed. This difference of the trajectory between the X-point and O-point causes the magnetic island deformation leading to the secondary magnetic reconnection at the original X-point as shown in Fig.II.2.2-1. In order to dissipate the piled up current near the resistive layer, the secondary reconnection continues for longer time as the resistivity becomes small [2.2-1].

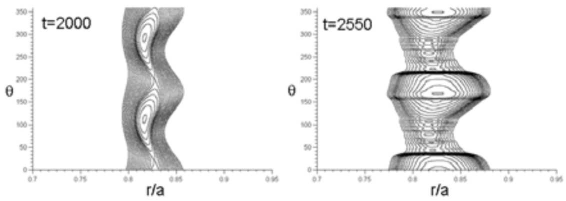

Fig. II.2.2-1 Magnetic island structures at the flow-suppressed phase, t=2000, and the transition phase, t=2550.

Reference

2.2-1 Ishii, Y., et al., *Proc. 21st Int. Conf. on Fusion Energy 2006 (Chengdu, 2006)* CD-ROM file TH/P3-05.

3. Divertor Physics

3.1 Self-Consistent Divertor Simulation of X-point MARFE with SONIC Code

A self-consistent modelling of divertor plasma and impurity transport has been developed. The key feature of this unified code, SONIC is to incorporate the elaborate impurity Monte Carlo (MC) code, IMPMC. The MC approach is superior to the fluid model from the aspect of flexibility of modelling. Interactions between impurities and walls, and kinetic effects can be easily included into the modelling. However, development of such divertor code coupled with impurity MC code is very difficult because of long computational time and noise in MC calculation. We resolve these problems by introducing the new diffusion model and optimizing with Message Passing Interface (MPI) on the massive parallel computer, SGI ALTIX 3900. Thereby combining the SOLDOR/NEUT2D code and the IMPMC code becomes possible. By using the early phase of this unified code, SONIC, we carry out the simulation of dynamic evolution of the X-point MARFE observed in JT-60U. Simulation results basically reproduced the dynamic evolution of X-point MARFE observed in JT-60U. It was found that the radiation near the X-point during MARFE originates in neutral carbons chemically sputtered from the private region. Figure II.3.1-1 shows that a remarkable narrow region appears inside the separatrix near the X-point. It is characterized by the extremely high density (4×10^{20} m^{-3}), and low temperature (2 ~ 3 eV) in spite of the core edge. [3.1-1].

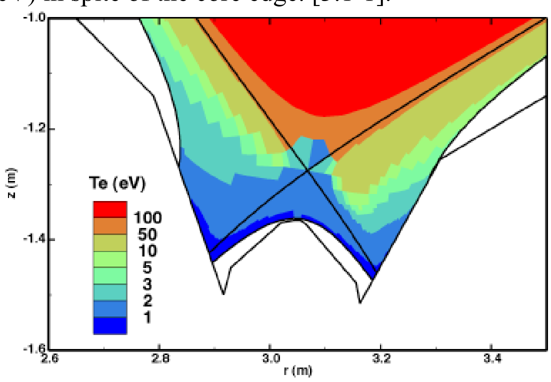

Fig. II.3.1-1 Electron temperature profile during X-point MARFE.

Reference

3.1-1 Shimizu, K., *et al.*, *J. Nucl. Mater.*, **363-365**, 426 (2007).

3.2 Dynamics of SOL-Divertor Plasmas after an ELM Crash in the Presence of Asymmetry

Dynamics of SOL-divertor plasmas after an ELM crash, especially in the presence of the asymmetry, is studied with a one-dimensional particle simulation code PARASOL. It is considered that in tokamaks the ELM-induced loss runs away mainly to the low-field-side SOL. The asymmetry in the heat flux is remarkable. The heat flux to the near plate Q_B is much larger than the heat flux to the far plate Q_A at the time of Q_B peak. In the latter phase, Q_A increases, Q_B decreases, and the asymmetry in Q is reversed. As a result total heat input to the near plate B is larger only by ~10% than that to the far plate A. The asymmetry in Q defined by the ratio of Q_B/Q_A (or Q_A/Q_B) is linearly dependent on the ratio of connection lengths L_A/L_B as shown in Fig. II.3.2-1. Electron heat propagation is governed by conduction, while majority of the heat is transported by convection with sound-speed time scale and its propagation time is linearly proportional to the parallel connection length [3.2-1].

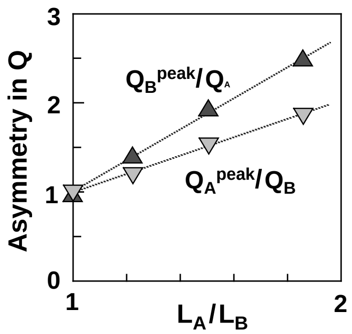

Fig. II.3.2-1 Asymmetry in Q (ratio of Q_B to Q_A) vs. L_A/L_B.

Reference

3.2-1. Takizuka, T., *et al*, *Trans. Fusion Sci. Technol.*, **51**, 271 (2007).

3.3 Modeling of Dynamic Response of SOL-Divertor Plasmas to an ELM Crash

A dynamic five-point model is developed to study responses of scrape-off layer (SOL) and divertor plasmas to a crash due to edge-localized modes (ELMs). The five-point model is beneficial to wide-ranging studies of SOL-divertor physics and to coupling with the core transport code in the integrated modeling. The five-point model can reproduce static and dynamic features obtained by usual fluid codes. The dynamic behavior obtained by the five-point model agrees fairly well with that by the particle code PARASOL. The influence of the ELM crash on the thermoelectric instability and the resultant asymmetry is investigated. The ELM crash transiently induces the thermoelectric instability and large SOL currents for asymmetric divertor plasmas before the ELM. The resultant currents drive convective heat flows and enhance the asymmetry on the fast time scale of electrons. The ELM crash is found to reverse the asymmetry before and after the ELM. Even for symmetric plasmas before the ELM, the asymmetry is induced on the slow time scale of ions by an ELM crash, because the transient formation of dense and cold divertor plasmas causes the thermoelectric instability [3.3-1].

Reference

3.3-1 Hayashi, N., *et al.*, *J. Nucl. Mater.*, **363-365**, 1044 (2007).

4. Integrated Simulation

4.1 Integrated Simulation for Burning Plasma Analysis

Based on the research in JT-60U experiments and first-principle simulations, integrated models of core, edge-pedestal, scrape-off-layer (SOL) and divertors were developed, and they clarified complex features of reactor-relevant plasmas. The integrated core plasma model indicated that the small amount of electron cyclotron (EC) current density of about half the bootstrap current density could effectively stabilize the neoclassical tearing mode by the localized EC current accurately aligned to the magnetic island center. The integrated edge-pedestal model clarified that the collisionality dependence of energy loss due to the edge-localized mode was caused by the change in the width of the unstable mode and the SOL transport. The integrated SOL-divertor model clarified the effect of the exhaust slot on the pumping efficiency and the cause of enhanced radiation near the X-point multifaceted asymmetric radiation from edge. Success in these consistent analyses using the integrated code indicates that it is an effective means to investigate complex plasmas and to control the integrated performance [4.1-1].

Reference

4.1-1 Ozeki, T. and JT-60 Team, *Phys. Plasmas*, **14**, 056114 (2007).

4.2 ELM Energy Loss Determined by Pedestal MHD and SOL Transport

An integrated simulation code TOPICS-IB based on a transport code (TOPICS) with a stability code for the peeling-ballooning modes (MARG2D) and a scrape-off-layer (SOL) model (five-point model) has been developed to clarify self-consistent effects of edge localized modes (ELMs) and the SOL on the plasma performance. The TOPICS-IB successfully simulates the transient behavior of the whole plasmas. Figure II.4.2-1 shows the time evolution of electron temperature profiles during an ELM crash. When an ELM crash occurs, the energy flows into the SOL and the SOL temperature rapidly increases. The increase of the SOL temperature lowers the ELM energy loss due to the flattening of the radial edge gradient. Experimentally observed collisionality dependence of the ELM energy loss is found to be caused by both the edge bootstrap current and the SOL transport. The bootstrap current decreases with increasing the collisionality and intensifies the magnetic shear at the pedestal region. The increase of the magnetic shear reduces the width of eigenfunctions of unstable modes, which results in the reduction of both the area of the ELM enhanced transport and the ELM enhanced transport near the separatrix. On the other hand, the parallel electron heat conduction determines how the SOL temperature increases. For higher collisionality, the conduction becomes lower and the SOL electron temperature increases more. By the above two mechanisms, the ELM energy loss decreases with increasing the collisionality as shown in Fig.II.4.2-2 [4.2-1].

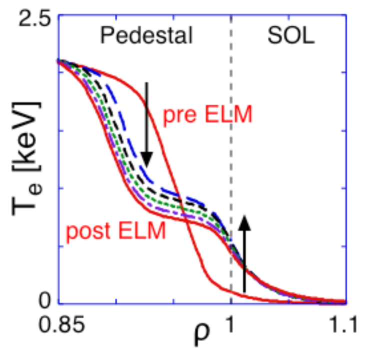

Fig. II.4.2-1 Time evolution of electron temperature profile of pedestal (ρ<1) and SOL plasmas (ρ>1) during an ELM crash (40 μs intervals).

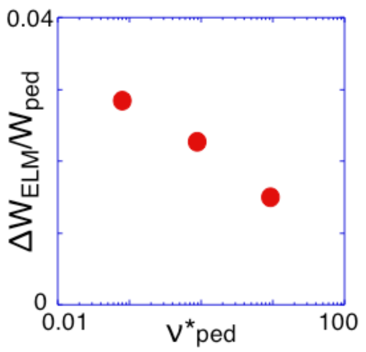

Fig. II.4.2-2 Dependence of ELM energy loss $\Delta W_{ELM}/W_{ped}$ on collisionality ν^*_{ped}.

Reference

4.2-1 Hayashi, N., *et al.*, *Nucl. Fusion*, **47**, 682 (2007).

5. Numerical Experiment of Tokamak (NEXT)

5.1 Self-organization in Electron Temperature Gradient Driven Turbulence

Based on first principle gyrokinetic calculations, a zonal flow generation mechanism in the slab electron temperature gradient driven (ETG) turbulence with weak magnetic shear is identified as the self-organization via the turbulent spectral cascade in the two dimensional rotating fluid turbulence. The inverse energy cascade and the scaling of a zonal flow wave number, which is consistent with the Rhines scale length, are confirmed. An impact of the scaling, which depends on the density gradient, on the turbulent structure and transport is demonstrated for the slab ETG turbulence. In Fig.II.5.1-1, two simulations with and without the density gradient are started from ETG instabilities with the same growth rates, their nonlinear turbulent structures are significantly different depending on the density gradient. Zonal flow structures are produced only in a simulation with the density gradient, and turbulent heat transport is significantly reduced [5.1-1].

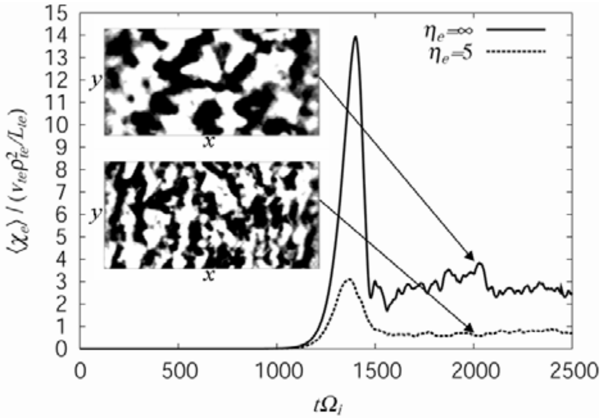

Fig.II.5.1-1 Electron Temperature Gradient driven (ETG) turbulence simulations with ($\eta_e = \infty$) and without (η_e=5) the density gradient. The figure shows time histories of the normalized turbulent heat diffusivity $<\chi_e>/(v_{te}\rho_{te}^2/L_{te})$ and snap shots of electrostatic potential f observed at $t\Omega_i$~2000.

Reference

5.1-1 Idomura, Y., *Phys. Plasmas* **13**, 080701 (2006)

5.2 Effects of ρ^* on Zonal Flow Behavior and Turbulent Transport in Tokamak Plasmas

Global ion temperature gradient (ITG) driven turbulence simulation has been performed for various ρ^* values, where $\rho_*=\rho_i/a$ is the ratio of an ion Larmor radius ρ_I to a minor radius a. It is found from the simulation that the radial width, in which oscillatory zonal flows called geodesic acoustic modes (GAMs) have the same frequency, is almost proportional to $(\rho_i a)^{1/2}$ and the radial wavelength of the GAMs is proportional to ρ_i. Turbulent ion heat transport is high in a GAM dominant region. It becomes clearer for smaller ρ_* as shown in Fig II. 5.2-1.

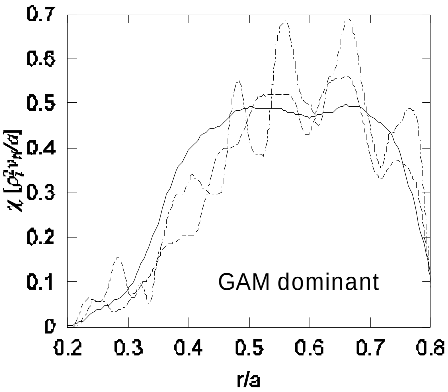

Fig. II.5.2-1 Radial profiles of normalized ion heat diffusivity for ρ_* =0.0125 (solid), 0.005 (dash) and 0.003 (dash dot).

References

5.2-1 Miyato, N., *et al.*, *Proc. 21st Int. Conf. on Fusion Energy 2006 (Chengdu, 2006*) CD-ROM file TH/P2-11.

5.2-2 Miyato, N., *et al.*, *Plasma Phys. Control. Fusion* **48**, A335 (2006).

5.3 Statistical Characteristics of Turbulent Transport Dominated by Zonal Flows

We investigated the ETG-driven turbulent transport in slab gyro-fluid simulations by measuring the cross spectrum between the pressure perturbation P and the poloidal electric field E_y. It is found that, the heat flux reduction by changing from the weak-ZF plasma to the ZF-dominated plasma has two origins at different radial positions. Fig. II.5.3-1(a) shows the radial profile of radial electric field in the ZF-dominated plasma, thus the direction of ZF is different at the "zone-A" and the "zone-B". In the zone-A, the heat flux is reduced by the decrease of the coherence between P and E_y, on the other hand, in the zone-B, that is reduced by the phase synchronization between P and E_y, as shown in Fig. II.5.3-1(b) and (c) [5.3-1].

Reference

5.3-1 Matsumoto, T., et al., *J. Plasma Physi.*, **72**, 1183 (2006).

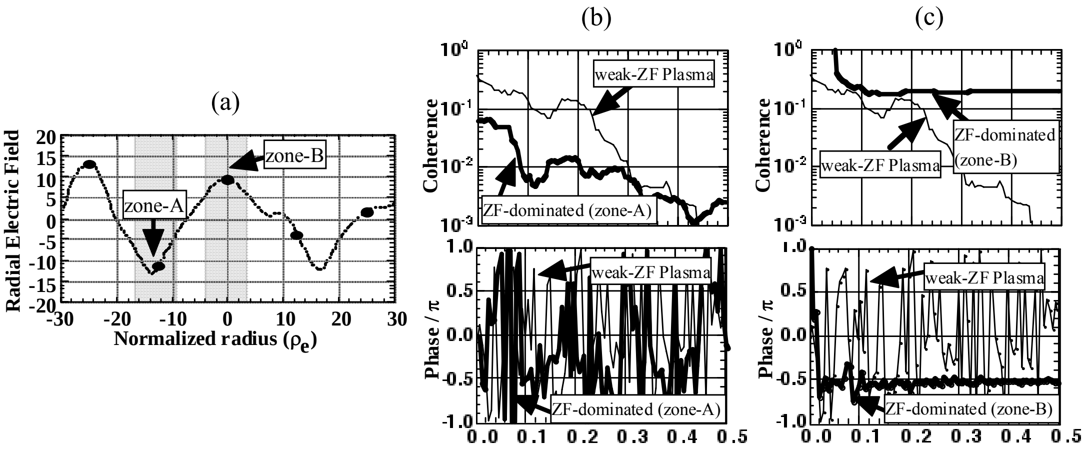

Fig. II.5.3-1 (a) Radial profile of the radial electric field in the ZF-dominated plasma. (b) Coherence and phase difference between P and E_y of a weak-ZF plasma (thin line), and the zone-A of the ZF-dominated plasma (thick line). (c) Coherence and phase difference between P and E_y of a weak-ZF plasma (thin line), and the zone-B of the ZF-dominated plasma (thick line).

6. Atomic and Molecular Data

We have been producing, collecting and compiling cross-section data for atomic and molecular collisions and spectral data relevant to fusion research.

The electron capture and the electron loss cross-section data of a singly ionized tungsten by collision with H_2, He, Ne, Ar and Kr have been measured at collision energies of 40.8 and 54.3 eV/amu. The relative cross-section data of the X-ray emission from Ne-line tungsten (W^{64+}) through di-electronic recombination have been measured [6-1]. The state selective charge transfer cross-section data of Be^{3+} and C^{6+} by collision with H* (n = 1, 2) in the collision energy range between 62 eV/amu and 6.2 keV/amu have been calculated with a molecular-bases close-coupling method. The cross-section data for 47 processes of collisions of He, He^{+} and He^{2+} with H, H_2, He, He^{+} and Li have been complied. The recommended cross-section data are expressed with analytic functions to facilitate practical use of the data. The compiled data are in preparation for the Web at the URL http://www-jt60.naka.jaea.go.jp/engish/JEAMDL/. The charge transfer data published in 2006 have been collected, and the database for the chemical sputtering yield data of graphite materials with hydrogen isotope collisions have been established.

Reference

6-1 Watanabe H., *et al*., *Plasma Fusion Res*., **2**, 027 (2007).

III. Fusion Reactor Design Study

1. Design Progress of DEMO Reactor

Fusion DEMO plant is requested to demonstrate 1) an electric power generation of 1GW level, 2) self-sufficiency of T fuel, 3) year-long continuous operation. From the economical aspect, the reactor size should be as compact as ITER. To meet these requirements, a DEMO reactor concept named SlimCS was proposed in 2005 [1-1]. Maintenance scheme was considered in 2006 [1-2].

The SlimCS plant is configured for quick replacement of the power core components and is designed for horizontal insertion and withdrawal of entire sectors. Each sector has its own horizontal port, allowing replacement of the entire sector without opening the cryostat or disassembling other components. The layout of reactor hall, storage hall and repair hall are shown in Fig.III.1-1. For higher reliability, the sector housing cask movement is limited a straight motion. For avoiding the reactor hall enlargement, the change of cask motion direction is carried out by the turn table system shown in Fig.III.1-1.

References

1-1 Tobita, K., *et al.*, *Fusion Eng. Des.*, **81**, 1151 (2006).

1-2 Nishio, S., *et al.*, *Fusion Eng. Des.*, **81**, 1271 (2006).

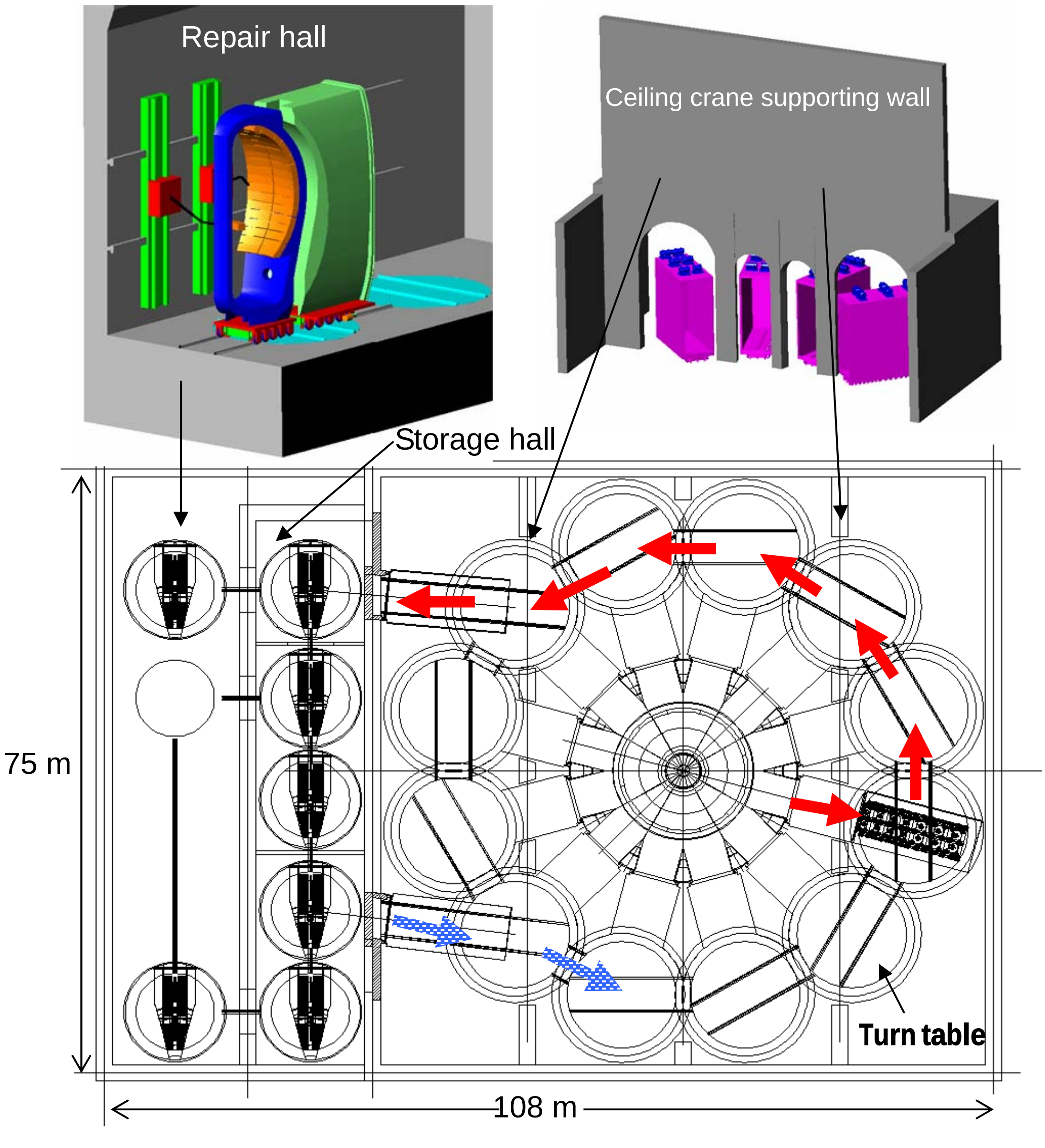

Fig. III.1-1 Conceptual view of Reactor hall and Hot cell

2. Current Ramp by Electron Cyclotron Wave

For the SlimCS reactor, the function of CS coil is limited to be plasma current (I_p) ramp-up to low current (~3.8MA) and shaping of plasma in the SlimCS. The heating and current drive (CD) are considered to be made by using neutral beam injection (NBI) [2-1] and electron cyclotron (EC) wave [2-2]. A large scale use of the EC wave have merits of high tritium breeding ratio (TBR), high locality of CD and a maintenance compared with the use of NBI. The high TBR is due to the following reasons: the transportation by a wave-guide, the easy equipment of a shield, the widely permitable location of port and small area of port ($30cm^2$/MW). So, feasibility of I_p ramp-up by the EC wave in the SlimCS reactor is considered [2-3].

The time evolution of I_p is evaluated using the circuit equation with particle and power balance equations. The current driven by the EC wave is estimated using a linearized Fokker Planck code with a ray trace code. The necessary power is 115 MW at the steady state of P_{fus} = 3 GW. The I_p can be ramped up from low I_p (= 2 MA) to state of P_{fus} = 3 GW using only EC wave. The two different n_e approaches are compared. The power needed in the case of low n_e approach is higher that in the case of high n_e approach. Although the power is low due to the high I_{EC}/I_p at the low I_p phase in the low n_e approach, the ECCD fraction of I_P is high at the close to the state of P_{fus} = 3 GW, then the necessary power is high compared with higher n_e approaches. The necessary power for the I_p ramp-up is 120 MW in the case of high n_e approach. The necessary power is almost the same as the power of 115 MW at the state of P_{fus} = 3 GW. The use of EC wave is compared the use of NBI from the points of the current driven efficiency and the constraints etc. The current driven efficiency by the EC wave is half that by neutral beam roughly as shown in Fig.III.2-1 [2-3]. Since the necessary power at the steady state in the case of EC wave is high compared with that in the case of NBI, the value of Q reduces to be 27. However, the value of Q is still high as acceptable for the power reactor.

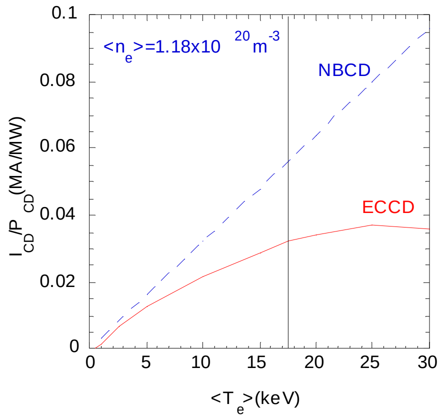

Fig. III.2-1 Current Drive Efficiencies of NBCD and ECCD

References

2-1 Inoue, T., *et al*., *Fusion Eng. Des.,* **81**, 1291 (2006).

2-2 Sakamoto, K., *et al*., *Fusion Eng. Des.,* **81**, 1263 (2006).

2-3 Sato, M., *et al*., *Proc. 14th Joint Workshop on ECE and ECRH (EC-14),* 205-210. (Santorini, Greece, 9-12 May 2006), Organized by the Research Unit, Association Euratom-Hellenic Republic.

3. External Control of Transport Barriers in Fully Non-Inductive Burning Discharge

A self-consistent simulation, including a model for improved core energy confinement, demonstrates that externally applied, inductive current perturbations can be used to control both the location and strength of internal transport barriers (ITBs) in a fully non-inductive tokamak discharge [3-1]. Time-evolutions of the plasma and bootstrap current profiles were simulated. The inductive current particularly perturbs the current density inside of the ITB with higher T_e than the edge, not affecting outside the ITB. The positive (negative) perturbation during 1700–1900 s (2100–2300 s) brings about the inward (outward) drift and corresponding decrease (increase) in the ITB-generated j_{BS}. We find that ITB structures formed with broad non-inductive current sources such as LHCD are more readily controlled than those formed by localized sources such as ECCD. Through this external control of the magnetic shear profile, we can maintain the ITB strength which is otherwise prone to deteriorate when the bootstrap current increases. The inductive current perturbation, which can be implemented by a weak Ohmic power, offers steady-state, advanced tokamak reactors an external means of efficient ITB control for regulating the fusion-burn net output and spatial profile.

Reference

3-1 Nakamura,Y., *et al*., *Nucl. Fusion* **46** S645 (2006).

Appendix

A.1 Publication List (April 2006 – March 2007)

A.1.1 List of JAERI/JAEA Report

1) Hamamatsu, K., "Modification of OFMC-code for JT-60U with ferritec steel," JAEA-Review 2006-025 (2006) (in Japanese).

2) Hatae, T., Kubomura, H., Matsuoka, S. , et al., "Design of single-longitudinal-mode laser oscillator for edge Thomson scattering system in ITER," JAEA-Technology 2006-021 (2006).

3) Hayashi, N., Ozeki, T., Aiba, N., "Integrated ELM simulation based on transport and MHD," JAEA-Review 2006-025 (2006) (in Japanese).

4) Ida, M., Nakamura, H., Yamamura, T., et al., "Investigation of IFMIF target assembly structure design," JAEA-Technology 2006-044 (2006).

5) Kakudate, S., Takeda, N., Nakahira, M., et al. "Design and rescue scenario of common repair equipment for in-vessel components in ITER hot cell," JAEA-Technology 2006-038 (2006).

6) Kobayashi, Y., Hamamatsu, K., "Study of toroidal rotation induced by alpha particles based on OFMC-code.," JAEA-Review 2006-025 (2006) (in Japanese).

7) Miyashita,M.,Yutani,T.,Sugimoto,M., "Investigation of high flux test module for the International Fusion Materials Irradiation Facilities (IFMIF)," JAEA-Technology 2007-016 (2007).

8) Mohri, K., Suzuki, S., Enoeda, M., et al., "Preliminary investigation on welding and cutting methods for first wall support leg in ITER blanket module," JAEA-Technology 2006-042 (2006).

9) Nakamura, H., Ida, M., Shimizu, K., et al., "Thermo-structural analysis of backwall in IFMIF lithium target," JAEA-Technology 2007-008 (2007).

10) Nakao, M., Hori, J., Ochiai, K., et al., "Evaluation of deuteron-induced activation for IFMIF accelerator structural materials," JAEA-Research 2006-071 (2006).

11) Ogawa, H., Sugie,T., Kasai, S. et al., "Design of impurity influx monitor (Divertor) for ITER," JAEA-Technology 2006-015 (2006).

12) Takizuka, T., "Simulation of SOL-divertor plasmas using advanced particle code PARASOL," JAEA-Review 2006-025 (2006) (in Japanese).

13) Tsuchiya, K., Kawamura, H., "Fabrication and characterization of Li-6 enriched Li2TiO3 pebbles for a high Li-burnup irradiation test," JAEA-Techology 2006-047 (2006).

14) Yamaki, D., Tanifuji, T., Aruga, T., et al., "Observation of microstructural changes and irradiation damages in Li2TiO3 caused by multi ion beam irradiation," JAEA-Review 2006-042, 26 (2006).

A.1.2 List of papers published in journals

1) Abe, K., Nakajima, H., Hamada, K., et al., “Manufacturing study and trial fabrication of radial plate for ITER toroidal field coil,” IEEE Trans. Appl. Supercond., **16**, pp.807 (2006).

2) Aiba, N., Tokuda, S., Ishizawa, T., “Analysis of an aspect ratio effect on the stability of external MHD modes in tokamaks with the Newcomb equation,” J. Plasma Phys., **72**, pp.1127 (2006).

3) Aiba, N., Tokuda, S., Ishizawa, T., et al., “Extension of the Newcomb equation into the vacuum for the stability analysis of tokamak edge plasmas,” Comput. Phys. Commun., **175**, pp.269 (2006).

4) Aoki, S., Wada, M., (Mohri, K.), et al., “Effect of the heat treatment conditions onto characteristics of chromium-zirconium copper,” J. Jpn Res. Inst. Adv. Copper-Base Mater. and Technol., **45**, pp.125 (2006).

5) Asai, K., Naoi, N., (Nishitani, T.), et al., “Novel concept of time-of-flight neutron spectrometer for measurement of the D/T burning ratio in the ITER,” Rev. Sci. Instrum., **77**, 10E721 (2006).

6) Baylor, L.R., Parks, P.B., (Maruyama, S.), et al. “Pellet fueling and control of burning plasmas in ITER,” Nucl. Fusion, **47**, pp.443 (2007).

7) Fujita T., and the JT-60 team “Advanced tokamak research on long time scales in JT-60 Upgrade,” Phys. of Plasmas, **13**, pp.56112 (2006).

8) Hamada, K., Nakajima, H., Kawano, K. et al., “Optimization of JK2LB chemical composition for ITER Central Solenoid conduit material,” Cryogenic, **47**, pp.174 (2007).

9) Hamada, K., Nakajima, H., Kawano, K., et al., “Demonstration of JK2LB Jacket Fabrication for ITER Central Solenoid,” IEEE Trans. Appl. Supercond., **16**, pp.787 (2006).

10) Hatae, T., Naito, O., Nakatsuka, M. , et al., “Applications of phase conjugate mirror to Thomson scattering diagnostics,” Rev. Sci. Instrum., **77**, 10E508 1 (2006).

11) Hatae, T., Naito, O., Kitamura, S., “Applications of stimulated Brillouin scattering phase conjugate mirror to Thomson scattering diagnostics in JT-60U and ITER,” J. Korean Phys. Soc., **49**, S160 (2007).

12) Hayashi, N., Takizuka, T., Sakamoto, Y., et al., “Physics of strong internal transport barriers in JT-60U reversed-magnetic-shear plasmas,” Plasma Phys. Control. Fusion, **48**, A55 (2006).

13) Hirata, M., Cho, T., (Kondoh, T.), et al., “Study of the effects of plasma-confining potentials using end-loss analysing systems,” Trans. Fusion Sci. Tech. **51**, pp.183 (2007).

14) Hirata, M., Miyake, Y., (Kondoh, T.), et al., “A novel position-sensitive ion-current detector array using a self-collection method for secondary-electro suppression,” Nucl. Instrum. Meth. Phys. Res. A, **573**, pp.34 (2007).

15) Hirata, M., Miyake, Y., (Kondoh, T.), et al., “Simultaneous measurements of ion and electron currents using a novel compact electrostatic end-loss-current detector,” Rev. Sci. Instrum. **77**, 10E719 (2006).

16) Hirohashi, M., Murakami, H., Ishiyama, H., et al., “Numerical simulation of the critical current and n-value in Nb3Sn strand subjected to bending strain,” IEEE Trans. Appl. Supercond., **16**, pp.1721(2006).

17) Ida, M., Nakamura, H. and Sugimoto, M., “Estimation and control of beryllium-7 behavior in liquid lithium loop of IFMIF,” 24th Symposium on Fusion Technology, to be published in Fusion Eng. Des..

18) Imai, T., Tatematsu, Y., (Sakamoto, K.), et al., “Upgrade program of ECRH system for GAMMA10,” Fusion Sci. Tech., **51**, pp.208 (2007)

19) Imai, M., Shirai,T., (Kubo, H.), et al., "Production and compilation of charge changing cross sections of ion-atom and ion-molecule collisions," J. Plasma and Fusion Res. Series

20) Ioki, K., Elio, F., (Enoeda, M.,) et al., "Six-party qualification program of FW fabrication methods for ITER blanket module procurement," Fusion Eng. Des., 15-24, pp.1774 (2007).

21) Isayama, A., Oyama, N., Urano, H., et al., "Control of growth of neoclassical tearing by central co-ECCD in JT-60U," Plasma and Fusion Research, **1** , 030-1 (2006)

22) Ishikawa, M., Itoga, T., Okuji, T., et al., "Fast collimated neutron flux measurement using Stilbene scintillator and Flash-ADC in JT-60U," Rev. Sci, Instrum., **77**, 10E706 (2006).

23) Ishikawa, M., Takechi, M., Shinohara, K., et al., "Observation of confinement degradation of energetic ion due to Alfvén eigenmodes in weak shear plasmas on JT-60U," Nucl. Fusion **46**, S898 (2006)

24) Isono, T., Hamada, K., Okuno, K., "Design optimization of a HTS current lead with large current capacity for fusion application," Cryogenic, **46**, pp.683 (2006).

25) Itoh, K., Itoh, T., (Ida, M.), et al., "Two-dimensional optical measurement of waves on liquid lithium jet simulating IFMIF target flow," 14th Inter. Conf. on Nuclear Engineeing (DVD).

26) Shimizu, K., Takizuka, T., Kawashima, H., "A new fast velocity-diffusionmodelling for impurity transport in integrated edge plasma simulation," J. Nucl. Mater., **363-365**, pp.426 (2007).

27) Watanabe, K., Kashiwagi, M., Kawashima, S., "Development of a dc 1 MV power supply technology for NB injectors," Nucl. Fusion, **46**, S332-S339 (2006).

28) Kakudate, S., Shibanuma, K., "Kinematic analysis on rail deployment into vacuum vessel for ITER blanket maintenance," J. Plasma Fusion Res., **82**, 9, pp.628 (2006) (in Japanese).

29) Kamada,Y., Oyama,N., Ide, S., et al., "Impact of the edge pedestal characteristics on the integrated performance in advanced tokamak operation modes on JT-60U," Plasma Phys. Control. Fusion, **48**, A419 (2006).

30) Kamata, Y., Imai, T., (Sakamot, K.), et al., "Characteristics of 28GHz gyrotron for ECRH on GAMMA10," Fusion Sci. Tech., **51**, pp.412 (2007).

31) Kamiya, K., Urano, H., Koide, Y., et al., "Characterization of Type-I ELMs in tangential co-, balanced- and counter- plus perpendicular NBI heated plasmas on JT-60U," Plasma Phys. Control. Fusion, **48**, A131 (2006).

32) Kanemura, T., Kondo, H., (Ida, M.), et al., "Investigation of free-surface fluctuations of liquid lithium flow for IFMIF lithium target by using an electro-contact probe," 24th Symposium on Fusion Technology, to be published in Fusion Eng. Des..

33) Kariya, T., Mitshinaka, Y., (Sakamoto, K.)., et al, "Optimization of 28GHz gyrotron output performance for ECRH experiment of the GAMMA10," Fusion Sci. Tech., **51**, pp.397 (2007).

34) Kashiwa, Y., Saigusa, M., Takahashi, K., et al., "Study of Ohmic loss of high power polarizaers at 170GHz for ITER," Fusion Eng. Des., **81**, pp.2249 (2006).

35) Kasugai, A., Minami, R., Takahashi, K., et al., "Long pulse operation of 170GHz ITER gyrotron by beam current control," Fusion Eng. Des., **81**, pp.2791 (2006).

36) Kasugai, A., Minami, T., Takahashi, K., et al., "High power and high efficiency operation of 170GHz gyrotron," Fusion Sci. Tech., **51**, pp.213 (2007).

37) Kawamura, Y., Isobe, K., Yamanishi, T., "Mass transfer process of hydrogen via ceramic proton conductor membrane of electrochemical hydrogen pump," Fusion Eng. Des., **82**, pp.113 (2007).

38) Kawashima, H., Shimizu, K., Takizuka, T., et al., “Development of integrated SOL/Divertor code and simulation study in JAEA,” Plasma and Fusion Research, **1**, 031-1 (2006).

39) Kaye, S. M., Valovic, M., (Takizuka, T.), et al., “The role of aspect ratio and beta in H-mode confinement scalings,” Plasma Phys. Control. Fusion, **48**, A429 (2006).

40) Kikuchi, K., Nakamura, H., Tsujimoto K., et al., “Evaluation of residual tritium in stainless steel irradiated at SINQ target 3,” J. Nucl. Mater., **356**, pp.157 (2006).

41) Kikuchi, M., Tamai, H., (Akiba, M.), et al., “Overview of the National Centralized Tokamak programme,” Nucl. Fusion, **46**, S29 (2006).

42) Koizumi, N., Nunoya, Y., Okuno, K., “A new model to simulate critical current degradation of a large CICC by taking into account strand bending,” IEEE Trans. Appl. Supercond., **16**, pp.831 (2006).

43) Kondo, K., Murata, I., Ochiai, K., et al., “Charged-particle sepctrometry using a pencil-beam DT neutron source for double-differential cross-section measurement,” Nucl. Instrum. Methods Phys. Res. A, **568**, pp.723 (2006).

44) Kondo, H., Kanemura, T., (Ida, M.), et al., “Measurement of free surface of liquid metal lithium jet for IFMIF target,” 24th Symposium on Fusion Technology, to be published in Fusion Eng. Des..

45) Kondoh, T., Hayashi, T., Kawano, Y., et al., “CO_2 laser for collective Thomson scattering diagnostic of a-particles in burning plasmas,” Trans. Fusion Sci. Tech. **51**, pp.62 (2007).

46) Kondoh, T., Hayashi, T., Kawano, Y., et al., “High-repetition CO_2 laser for collective Thomson scattering diagnostic of a particles in burning plasmas,” Rev. Sci. Instrum., **77**, 10E505 (2006).

47) Kramida, A. E., Shirai,T., “Compilation of wavelengths and energy levels of tungsten, W III through W LXXIV,” J. Plasma and Fusion Res., Series, **7**, pp.334 (2006).

48) Kubo, H., Sataka, S., Shirai, T., “Atomic and molecular data activities for fusion research at JAERI,” J. Plasma and Fusion Res. Series, **7**, pp.352 (2006).

49) Kusakabe, T., Shiota, K., Kubo, H., et al., “Cross sections of charge transfer by slow doubly-charged carbon ions from various carbon containing molecules,” J. Plasma and Fusion Res. Series, **7**, pp.237 (2006).

50) Leonard, A. W., Asakura, N., (Oyama, N.), et al., “Survey of Type I ELM dynamics measurement,” Plasma Phys. Control. Fusion, **48**, A149 (2006).

51) Liu, D., Heidbrink, W. W., (Shinohara, K.), et al., “Performance of solid state neutral particle analyzer array on NSTX,” Rev Sci Instrum, **77**, 10F113-1 (2006).

52) Hanada, M., Seki, T., Takado, N., “The origin of beam non-uniformity in a large Cs-seeded negative ion source,” Nucl. Fusion, **46**, S318-S323 (2006).

53) Hanada, M., Seki, T., Takado, N., et.al., “Improvement of beam uniformity by magnetic filter optimization in a Cs-seeded large negative-ion source,” Rev. Sci. Instrum., **77**, 03A515 (2006).

54) Sugihara, M., Shimada, M., Fujieda, H., et al., “Disruption Scenarios, their mitigation and operation windows in ITER,” Nucl. Fusion, **47**, pp.337 (2007).

55) Taniguchi, M., Inoue, T., Kashiwagi, M., et.al., “Acceleration of MeV-class energy, high-current-density H--ion beams for ITER neutral beam system,” Rev. Sci. Instrum., **77**, 03A514 (2006).

56) Maebara, S., Moriyama, S., (Sugimoto, M.), et al., “Beam dynamics of a 175 MHz RFQ for an IFMIF project,” 10th European particle Accelerator Conference (CD-ROM).

57) Matsukawa, M., Tamai, H., Fujita, T., et al., “Poloidal Field Coil Configuration and Plasma Shaping Capability in NCT,” IEEE Transactions on Applied Superconductivity, **16**, pp.914 (2006)

58) Matsunaga, G., Takechi, M., Kurita, G., et al., “Effect of plasma-wall separation on the stability of resistive wall modes in the JT-60U tokamak,” Plasma Physics and Controlled Fusion, **49**, pp.95 (2006)

59) Matsunaga, G., Takechi, M., Toi, K., “Fast data acquisition system based on digital oscilloscopes for fluctuation measurements in a long pulse JT-60U tokamak plasma,” Fusion Eng. Des., **2**, pp.207 (2007).

60) McDonald, D. C., Cordey, J. G., (Takizuka, T.), et al., “Recent Progress on the Development and Analysis of the ITPA Global H-mode Confinement Database,” Nucl. Fusion, **47**, pp.147 (2007).

61) McDonald, D. C., Meakins, A. J., (Takizuka, T.), et al., “The impact of statistical models on scalings derived from multi-machine H-mode threshold experiments,” Plasma Phys. Control. Fusion, **48**, A439 (2006).

62) Kashiwagi, M., Hanada, M., Yamana, T., “Suppression of fast electron leakage from large openings in a plasma neutralizer fro N-NB systems,” Fusion Eng. Des., **81**, pp.2863 (2006).

63) Minami, T., Kasugai, A., Takahashi, K., et al., “The designs of high efficiency launcher of quasi-optical mode converter for high power gyrotrons,” Int. J. Infrared and millimeter waves., **27**, pp.13 (2006).

64) Miyato, N., Kishimoto, Y. and Li, J. Q., “Nonlocal behaviour of zonal flows in tokamak plasmas,” Plasma Phys. Control. Fusion, **48**, A335 (2006).

65) Takei, N., Nakamura, Y., Ushigome, M., et al., “Intermittent β collapse after NBCD turn-off in JT-60U fully non-inductive reversed shear discharges,” Plasma Phys. Control. Fusion, **49**, pp.335 (2007).

66) Takado, N., Hanatani, J., Mizuno, T., et.al., “Numerical analysis of the spatial nonuniformity in a Cs-seeded H-ion source,” Rev. Sci. Instrum., **77**, 03A533 (2006).

67) Umeda, N., Ikeda, Y., Hanada, M., et.al., “Beam deflection by plasma grid filter current in the negative-ion source for JT-60U neutral beam injection system,” Rev. Sci. Instrum. **77**, 03A529 (2006).

68) Nagashima, Y., Hoshino, K., Nagaoka, K., et al., “Experimental Study of Nonlinear Processes in Edge Turbulence of Toroidal Plasmas,” Plasma and Fusion Research, **1**, pp.41 (2006).

69) Nagshima, Y., Itoh, K., (Hoshino, K.), et al., “Convergence study of bispectral analysis in experiments of hirh temperature plasmas,” Rev. Sci. Instrum., **77**, 045110-1 (2006).

70) Nakamura, Y., Tobita, K., Fukuyama, A., et al., “A simulation study on inductive ITB control in reversed shear tokamak discharges,” Nucl. Fusion, **46**, S645 (2006).

71) Nakamura, H., Ida, M., Chida, T., et al., “Design of a lip seal-replaceable backwall for IFMIF liquid lithium target,” 24th Symposium on Fusion Technology, to be published in Fusion Eng. Des..

72) Naoi, N., Asai, K., (Nishitani, T.), et al., “Design consideration for high-energy-resolution neutron spectrometer based on associated particle detection using proton recoil telescope and time-of-flight technique for ITER,” Rev. Sci. Instrum., **77**, 10E724 (2006).

73) Ochi, A., Kiyamura, H., (Ochiai, K.), et al., “Thin gap chamber performance tests under several MeV neutron sources,” Rev. Sci. Instrum., **77**, 10E709 (2006).

74) Ochiai, K., Kubota,N., Taniike, A., et al., “Confined alpha particle diagnostics for ITER based on measurements of gamma rays emitted from D(α,γ)6Li reaction,” Rev. Sci. Instrum., **77**, 10E730 (2006).

75) Oda, Y., Komurasaki, K., Takahashi, K., et al., “Atomospheric pressure dependence of the microwave rocket's performance powered by a high power gyrotron,” J. Plasma Fusion Res., **83**, pp.296 (2007).

76) Oda, Y., Komurasaki, K., Takahashi, K., et al., “Plasma generaton using high-power millimeter-wave beam and its application for thrust generation,” J. Appl. Phys., **100**, pp.113307 (2006).

77) Okada, K., Kondo, K., Sato, S., et al., “Development of neutron measurement system for nd/nt fuel ratio measurement in ITER experiments,” Rev. Sci. Instrum., **77**, 10E726 (2006).

78) Okuno, K., Nakajima, H., Sugimoto, M., et al., “Japanese contributions to the procurement of the ITER superconducting magnet,” Fusion Eng. Des., **81**, pp.2341 (2006).

79) Okuno, K., Nakajima, H.,Koizumi, N., “From CS and TF model coil to ITER: Lessons learnt and further progress,” IEEE Trans. Appl. Supercond., **16**, pp.880 (2006).

80) Oyama, N., Kamada, Y., Isayama, A., et al., “ELM frequency dependence on toroidal rotation in the grassy ELM regime in JT-60U,” Plasma Phys. Control. Fusion, **49**, pp.249 (2007).

81) Oyama, N., Gohil, P., Horton, L. D., et al., “Pedestal Conditions for small ELM regimes in tokamaks,” Plasma Phys. Control. Fusion, **48**, A171 (2006).

82) Ozeki, T., Aiba, N., Hayashi, N., et al., “Integrated Simulation Code for Burning Plasma Analysis,” Fusion Sci. Technol., **50**, pp.68 (2006).

83) Parchamy, H., Peterson, B. J., Konoshima, S., et al., “Detailed In-situ Laser Calibration of the Infrared Imaging Video Bolometer for the JT-60U Tokamak,” Rev. Sci. Instrum., **77**, 10E515 (2006).

84) Sakamoto, Y., Ide, S., Yoshida, M., et al., “Response of toroidal rotation velocity to electron cyclotron wave injection in JT-60U,” Plasma Phys. Control. Fusion, **48**, A63 (2006).

85) Sakata, S., Totsuka, T., Kiyono, K., et al., “Progress of data processing system in JT-60 -Development of remote experiment system,” Fusion Eng. Des., **81**, pp.1775 (2006).

86) Sasao, M. and Steering Commitee members of MEXT Sci. Res. of Priority Areas "Advanced Diag. for Burning Plasmas", “Advanced diagnostics for burining plasma experiments,” Trans. Fusion Sci. Tech., **51**, pp.41 (2007).

87) Sataka, M., Kubo, H., “Atomic and Molecular Data Base and Data Activities for Fusion Research in Japan Atomic Energy Agency,” Trans. Fusion Sci. Tech., **51**, pp.135 (2007).

88) Sato, S., Iida, H., Nishitani, T., “Development of CAD/MCNP interface program prototype for fusion reactor nuclear analysis,” Fusion Eng. Des., **81**, pp.2767 (2006).

89) Sato, S., Wada, M., Nishitani, T., et al., “Impact of Reflector on Tritium Production in DT Neutron Experiment Evaluated by Monte Carlo Calculation,” Plasma Fusion Res., **2**, pp.002 (2007).

90) Shibama, Y., Sawai, Y., Sakurai, S., et al., “Fabrication of 8Cr-2W Ferritic Steel Tile for Reduction in Toroidal Magnetic Field Ripple on JT-60U,” J. Korean Phys. Soc., **49**, pp.297 (2006).

91) Shimakura, N., Honnma, M. , Kubo, H., et al., “Electron capture processes in low-energy collisions of C4+ ions with excited H atoms using molecular-bases close-coupling method,” J. Plasma and Fusion Res. Series,**7**, pp.199 (2006).

92) Shinohara, K. and JT-60 Team “Review of Recent Steady-State Advanced Tokamak Research and its Further Pursuit by Reduction of TF Ripple on JT-60U,” J. Korean Phys. Soc., **49**, S56 (2006).

93) Shinohara, K., Isobe, M., Darrow, D., et al., “Escaping ion measurement with high time resolution on CHS,” Rev. Sci. Instrum., **77**, 110E521-1 (2006).

94) Shinohara, K., Suzuki, Y., Sakurai, S., et al., “Orbit following calculation of energetic ions for design of ferritic insertion on JT-60U,” Plasma and Fusion Research, **1**, pp.007 (2006).

95) Shu, W. M., Kawasuso, A., Miwa, Y., et al., “Microstructure dependence of deuterium retention and blistering in the near-surface region of tungsten exposed to high flux deyterium plasmas of 38eV at 315K,” Phys. Scr., **T128**, pp.96 (2007).

96) Shu, W. M., Waki, E., Yamanishi, T., “Blister bursting and deuterium bursting release from tungsten expesed to high fluences of high flux and low energy deuterium plasma,” Nucl. Fusion, **47**, pp.201 (2007).

97) Smirnov, R., Tomita, Y., (Takizuka, T.), et al., “Two-Dimensional Simulation Study on Charging of Dust Particle on Plasma-Facing Wall,” Contrib. Plasma Phys., **46**, pp.623 (2006).

98) Sugihara, M., Shimada, M., Fujieda, H., et al., “Disruption scenarios, their mitigation and operation window in ITER,” Nucl. Fusion, **47**, pp.337 (2007).

99) Suzuki, T., Fujita, T., Oyama, N., et al., “Density fluctuation measurement using motional Stark effect optics in JT-60U,” Rev. Sci. Instrum., **77**, 10E914 (2006).

100) Inoue, T., Kashiwagi, M., Taniguchi, M., “1 MeV, ampere class accelerator R&D for ITER,” Nucl. Fusion, **46**, S379-S385 (2006).

101) Tabata, T. , Shirai, T., (Kubo, H.), et al., “Analytic cross sections for elecron impact collisions with nitrogen molecules,” Ato. Data Nucl. Data Tables, **92**, pp.375 (2006)

102) Takahashi, Y., Yoshida, K., Nabara, Y., et al., “Simulation of quench tests of the central solenoid insert coil in the ITER central solenoid model coil,” IEEE Trans. Appl. Supercond., **16**, pp.783 (2006).

103) Takenaga, H., Kubo, H., Kamada, Y., et al., “Study of impurity injection scenario in burning plasmas,” Fusion Sci. Technol., **50**, pp.503 (2006).

104) Takenaga, H., Miura, Y., Kubo, H., et al., “Burn control study using burning plasma simulation experiments in JT-60U,” Fusion Sci. Technol., **50**, pp.76 (2006).

105) Takenaga, H., Oyama, N., Asakura, N., “Transient response of divertor plasma during transition to ELM free H-mode phase in JT-60U,” Plasma Fusion Res., **1**, pp.46 (2006).

106) Takenaga, H., Oyama, N., Bruskin, L. G., et al., “Temporal variation of density fluctuation and transport in reversed shear plasmas on JT-60U,” Plasma Phys. Control. Fusion, **48**, A401 (2006).

107) Takenaga, H., Oyama, N., Isayama, A., et al., “Observation on decoupling of electron heat transport and long-spatial-scale density fluctuations in a JT-60U reversed shear plasma,” Plasma Phys. Control. Fusion, **49**, pp.525 (2007).

108) Takizuka, T., Hosokawa, M., “Dynamics of SOL-divertor plasmas after an ELM crash in tokamak H-mode plasma,” Trans. Fusion Sci. Technol., **51**, pp.271 (2007).

109) Takizuka, T., Hosokawa, M., “Particle simulation of the transient behavior of one-dimensional SOL-divertor plasmas after an ELM crash,” Contrib. Plasma Phys., **46**, pp.698 (2006).

110) Takizuka, T., Urano, H., Takenaga, H., et al., “Origin of the various beta dependences of ELMy H-mode confinement properties,” Plasma Phys. Control. Fusion, **48**, pp.799 (2006).

111) Toh, K., Shikama, T., (Yamauchi, M.), et al., “Effect of photobleaching on radiation-induced transmission loss of fused-silica-core optical fibres under gamma-ray and 14 MeV neutron irradiation,” Meas. Sci. Technol., **17**, pp.955 (2006).

112) Tomita, Y., Smirnov, R., Takizuka, T., et al., “Charging of a spherical dust particle on a plasma-facing wall,” J. Plasma Phys., **72**, pp.1015 (2006).

113) Tomita, Y., Smirnov, R., Takizuka, T., et al., “Gravitational effect on released conditions of dust particle from plasma-facing wall,” Contrib. Plasma Phys., **46**, pp.617 (2006).

114) Tsuchiya, K., Kizu,K., Takahashi, H., et al., “Stress analyses of the support structure and winding pack of the superconducting TF coil in National Centralized Tokamak,” IEEE Trans. Appl. Supercond., **16**, pp.922 (2006).

115) Uehara, K., Tsuzuki, K., Amemiya, H., et al., “Direct identification of magnetic surface by a differential double probe in JFT-2M,” Jpn. J. Appl. Phys., **45**, L630 (2006).

116) Urano, H., Kamiya, K., Koide, Y., et al., “Roles of plasma rotation and toroidal field ripple on H-mode pedestal structure in JT-60U,” Plasma Phys. Control. Fusion, **48**, A193 (2006).

117) Urano, H., Takizuka, T., Takenaga, H., et al., “Confinement degradation with beta for ELMy H-mode plasmas in JT-60U tokamak,” Nucl. Fusion, **46**, pp.781 (2006).

118) Verzilov, Y., Sato, S., Ochiai, K., et al., “The integral experiment on beryllium with D-T neutrons for verification of tritium breeding,” Fusion Eng. Des., **82**, 1, pp.1 (2007).

119) Yagai, T., Nunoya, Y., Takahashi, Y., et al., “Irregular loops with long time constants in CIC conductor,” IEEE Trans. Appl. Supercond., **16** , pp.835 (2006).

120) Yamada, H., Kawamura, Nagao, Y., et al., “Mechanical properties of weldments using irradiated stainless steel welded by the laser method for ITER blanket replacement,” J. Nucl. Mater., **355**, pp.119 (2006).

121) Yoshida, H., Yokoyama, K., Suzuki, S., et al., “Development of a 100 eV, high-flux ion beam acceleration system,” Rev. Sci. Instrum., **77**, 043502 (2006).

122) Yoshida, K., Takahashi, Y. and Iida, H., “Control and instrumentation for the ITER magnet system,” IEEE Trans. Appl. Supercond., **16**, pp.775 (2006).

123) Yoshida, M., Kobayashi, S., Urano, H., et al., “Observations of the collapse and recovery of the temperature pedestal using diagnostics with the fast temporal resolution in JT-60U,” Plasma Phys. Control. Fusion, **48**, A209 (2006)

124) Yoshida, M., Koide, Y., Takenaga, H., et al., “Effects of ripple loss of fast ions on toroidal rotation in JT-60U,” Plasma Phys. Control. Fusion, **48**, pp.1673 (2006).

125) Z, Li., Tanaka, T., (Sato, S.), et al., “Activation experiment with D-T neutrons on materials relevant to liquid blankets,” Fusion Eng. Des., **81**, pp.2893 (2006).

126) Zanino, R., Mitchell, N., Takahashi, Y., et al., “Implications of NbTi short-sample test results and analysis for the ITER poloidal field,” IEEE Trans. Appl. Supercond., **16**, pp.886 (2006).

127) Idomura, Y., “Self-organization in electron temperature gradient driven turbulence,” Phys. Plasmas, 13, 080701 (2006).

128) Li, J. Q., Kishimoto, Y., (Matsumoto, T.), et al., “Dynamics of secondary large-scale structure in ETG turbulence simulations,” Plasma Sci. Technol., **8**, 1, pp.110 (2006).

129) Li, J. Q., Kishimoto, Y., (Matsumoto, T.), et al., “Large-scale structures and electron transport in gyrofluid simulations of ETG turbulence in tokamak plasmas,” J. Plasma Phys., **72**, pp.1173 (2006).

130) Matsumoto, T., Kishimoto, Y., Li, J. Q., “Statistical characteristics of turbulent plasmas dominated by zonal flows,” J. Plasma Phys., **72**, pp.1183 (2006).

A.1.3 List of papers published in conference proceedings

1) Aiba, N., Tokuda, S., Takizuka, et al., “Effects of 'Sharpness' of the plasma cross-section on the stability of peeling-ballooning modes in tokamaks,” Proc. 21st IAEA Fusion Energy Conf., TH/P8-1 (CD-ROM) (2006).

2) Asakura, N., “Understanding of the SOL plasma flow in tokamaks, and influence on the plasma transport,” Proc. 17th Inter. Conf. on Plasma-Surface Interactions in Controlled Fusion Devices (2007).

3) Asakura,N., Ohno,N., Kawashima,H., et al., “ELM propagation and fluctuations characteristics in H- and L-mode SOL plasmas on JT-60U,” Proc.21st IAEA Fusion Energy Conf., EX/9-2 (CD-ROM) (2006).

4) Bonoli, P. T., Harvey, R. W., Oikawa, T., et al., “Benchmarking of lower hybrid current drive codes with application to ITER-relevant regimes,” Proc. 21st IAEA Fusion Energy Conf., IT/P1-2 (CD-ROM) (2006).

5) Costley, A. E., Walker, C., (Sugie, T.), et al., “The design and implementation of diagnostic systems on ITER,” Proc. 21st IAEA Fusion Energy Conf., IT/1-5 (CD-ROM) (2006).

6) Donné, A. J. H., Costley, A.E., (Kawano, Y.), et al., “High priority R&D topics in support of ITER diagnostic development,” Proc. 21st IAEA Fusion Energy Conf., IT/P1-24 (CD-ROM) (2006).

7) Enoeda, M., Hirose, T., Tanigawa, H., et al., “Test strategy and development achievements of ITER solid breeder test blanket modules in Japan,” Proc. 21st IAEA Fusion Energy Conf., FT/P5-19 (CD-ROM) (2006).

8) Ezato. K., Suzuki. S., Sato. K., et al., “Development of DEMO divertor with reduced activation ferritic/martensitic steel (F82H) in JAEA,” Proc. 21st IAEA Fusion Energy conf., FT/P5-37 (2006) (CD-ROM).

9) Fujisawa, A., Ido, T., (Hoshino, K.), et al., “Experimental progress on zonal flow physics in toroidal plasmas,” Proc. 21st IAEA Fusion Energy Conf., OV/4-4 (2006) (CD-ROM).

10) Fujita, T., Tamai, H., Matsukawa, M., et al., “Design optimization for plasma control and assessment of operation regimes in JT-60SA,” Proc.21th IAEA Fusion Energy Conf., FT/P7-4 (CD-ROM) (2006).

11) Hayashi, N., Takizuka, T., Ozeki, T., et al., “Integrated simulation of ELM energy loss determined by pedestal MHD and SOL transport,” Proc. 21st IAEA Fusion Energy Conf., TH/4-2 (CD-ROM) (2006).

12) Hayashi, T., Isobe, K., Kobayashi, K., et al., “Recent activities on tritium technologies for ITER and fusion reactors at JAEA,” Proc. 17th Topical Meeting on the Technol. of Fusion Energy (2006).

13) Hayashi, T., Nakamura, H., Isobe, K., et al., “Tritium behavior on the water-metal boundary for the permeation into cooling watrer through metal piping,” Proc. 17th Topical Meeting on the Technol. of Fusion Energy (2006).

14) Hayashi, T., Suzuki, T., Shu, W. M., et al., “Isotope effect of hydrogen rapidly supplied from the metal storage bed,” Proc. 17th Topical Meeting on the Technol. of Fusion Energy (2006).

15) Horiike, H., Kondo, H., Nakamura, H., et al., “Free-surface fluctuation at high speed lithium flow for IFMIF,” Proc. 21st IAEA Fusion Energy Conf., FT/P5-35 (2006) (CD-ROM).

16) Hoshino, K. and the JT-60 Team, “Application of ECW to the JT-60U Tokamak,” Proc. 14th Joint Workshop on Electron Cyclotron Emission and Electron Cyclotron Resonance Heating 26-36 (2006).

17) Hoshino, K., Ido, T., Nagashima, Y., et al., “Measurement and Analysis of the Fluctuations and Poloidal Flow on JFT-2M Tokamak,” Proc. 21st IAEA Fusion Energy Conf., EX/2-2 (2006) (CD-ROM).

18) Ida, K., Sakamoto, Y., Inagaki, S., et al., “Dynamic transport study of the plasmas with transport improvement in LHD and JT-60U,” Proc. 21st IAEA Fusion Energy Conference, P4-39 (CD-ROM) (2006).

19) Ide, S., Takenaga, H., Isayama, A., et al., “Studies on impact of electron cyclotron wave injection on the internal transport barriers on JT-60U,” Proc. 21st IAEA Fusion Energy Conf., P1-5 (CD-ROM) (2006).

20) Ioki, K., Chuyanov, V., Elio, P., et al., “ITER limiters moveable during plasma discharge and optimization of ferromagnetic inserts to minimize toroidal ripple,” Proc. 21st IAEA Fusion Energy Conf., IT/P2-9 (CD-ROM) (2006).

21) Isayama, A., Oyama, N., Urano, H., et al., “Active control of neoclassical tearing modes toward stationary high-beta plasmas in JT-60U,” Proc. 21st IAEA Fusion Energy Conf., EX/4-1Ra (CD-ROM) (2006).

22) Ishii, Y., Azumi, M., Smolyakov, A., “Nonlinear evolution and deformation of driven magnetic islands in rotating plasmas,” Proc. 21st IAEA Fusion Energy Conf., TH/P3-5 (CD-ROM) (2006).

23) Ishikawa, M., Takechi, M., Shinohara, K., et al., “Confinement degradation of energetic ions due to Alfvén eigenmodes in JT-60U negative-ion-based neutral beam injection plasmas,” Proc. 21st IAEA Fusion Energy Conf., EX/6-2 (CD-ROM) (2006).

24) Isobe, K., Yamanishi, T., Uzawa, M., “Development of ceramic electrolysis method for processing high-level tritiated water,” Proc. 8th IAEA Technical Meeting on Fusion Power Plant Safety, (2006).

25) Itoh, T., Hayashi, T., Isobe, K., et al., “Self-decomposition behavior of high concentration tritiated water,” Proc. 17th Topical Meeting on the Technol. of Fusion Energy (2006).

26) Kamada, Y., Leonard, A. W., Bateman, G., et al., “Edge pedestal physics and its implications for ITER,” Proc. 21st IAEA Fusion Energy Conf., IT/1-3 (CD-ROM) (2006).

27) Kasugai, A., Takahashi, K., Kobayashi, N., et al., “Development of 170GHz gyrotron for ITER,” Proc. 31st Int. Conf. on Infrared and Millimter waves and 14th Int. Conf. on Terahertz Electronics (CD-ROM) (2006).

28) Kawano, Y., Kondoh, T., Hatae, T., “Diagnostics of relativistic runaway electrons in a tokamak plasma based on laser inverse Compton scattering,” Proc. 33rd EPS Conf. on Plasma Physics, P4.138 (CD-ROM) (2006).

29) Kawashima, H., Shimizu, K., Takizuka, T., et al., “Simulation of divertor pumping in JT-60U with SOLDOR/NEUT2D code,” Proc. 17th Inter. Conf. on Plasma-Surface Interactions in Control. Fusion Devices, 786 (2007).

30) Kessel, C. E., Girruzi, G., Oikawa, T., et al., “Simulation of the hybrid and steady state advanced operating modes in ITER,” Proc. 21st IAEA Fusion Energy Conf., IT/P1-7 (CD-ROM) (2006).

31) Kikuchi, M., JA-EU satellite tokamak working group and JT-60SA design team, “Overview of modification of JT-60U for the satellite tokamak program as one of the Broader Approach projects and national program,” Proc. 21st IAEA Fusion Energy Conf., FT/2-5 (CD-ROM) (2006).

32) Kobayashi, K., Hayashi, T., Nakamura, H., et al., “Study for the behavior of tritiated water vapor on organic materials,” Proc. 17th Topical Meeting on the Technol. of Fusion Energy (2006).

33) Kobayashi, K., Isobe, K., Iwai, Y., et al., “Studies on behavior of tritium in components and structure materials of tritium confinement and detritiation system of ITER,” Proc. 21st IAEA Fusion Energy Conf., IT/P1-18 (CD-ROM) (2006).

34) Kobayashi, K., Miura, H., Hayashi, T., et al., “Oxidation performance test of detritiation system under existence of SF6,” Proc. 17th Topical Meeting on the Technol. of Fusion Energy (2006).

35) Kondoh, T., Hayashi, T., Kawano, Y., et al., “Collective Thomson scattering for alpha-particle diagnostics in burning plasmas,” Proc. 16th Inter. Toki conf. Advanced Imaging and Plasma Diagnostics, to be published in Plasma Fusion Res..

36) Konishi, S., Nakamura, H., Isobe, K., et al., “Light elements behavior in fusio devices studied with JT-60 and oxygen discharge,” Proc. 17th Topical Meeting on the Technol. of Fusion Energy (2006).

37) Kubo, H., Nakano, T., Asakura, N., et al., “Particle control under wall saturation in long-pulse high-density H-mode plasmas of JT-60U,” Proc. 21st IAEA Fusion Energy Conf., EX/P4-11 (CD-ROM) (2006).

38) Kubo, H., Sasaki, A., Moribayashi, K. , et al., “Study of highly ionized Xe spectra with 3s-3p and 3p-3d transitions in JT-60U reversed shear plasmas,” Proc. 17th Inter. Conf. on Plasma-Surface Interactions in Control. Fusion Devices, 1441 (2007).

39) Li, J. Q., Uzawa, K., (Matsumoto, T.), et al., “Simulations on the nonlinear mode coupling in multiple-scale drift-type turbulence with coherent flow structure,” Proc. 21st IAEA Fusion Energy Conf., TH/2-3 (CD-ROM) (2006).

40) Lipshultz, B., Asakura, N., Bonnin, X., et al., “Plasma-surface interaction, scrape-off layer and divertor physics: Implications for ITER,” Proc. 21st IAEA Fusion Energy Conf., IT/1-4 (CD-ROM) (2006).

41) Liu, Y., Tamura, N., (Konoshima, S.), et al., “Application of Tomographic imaging to multi-pixel bolometric measurements,” Proc. 16th Inter. Toki Conf. on Advanced Imaging and Plasma Diagnostics (2006), to be published in Journal of Plasma and Fusion Research.

42) Matsui, H., Sugimoto, M., Takatsu, H., et al., “Next phase activity of the International Fusion Materials Irradiation Facility under a new framework,” Proc. 21st IAEA Fusion Energy Conf., FT/1-3 (CD-ROM) (2006).

43) Matsumoto, T., Kishimoto, Y., Li, J. Q., “Characteristics of turbulent fluctuations in the presence of zonal flows,” Proc. 5th Burning Plasma Simulation Initiative Annual Meeting (2006).

44) Matsumoto, T., Kishimoto, Y., Li, J. Q., “Statistical characteristics of turbulent transport dominated by zonal flow dynamics,” Proc. 21st IAEA Fusion Energy Conf., TH/P2-9 (CD-ROM) (2006).

45) Matsunaga, G., Takechi, M., Kurita,G., et al., “Stabilization effects of wall and plasma rotation on resistive wall mode in JT-60U,” Proc. 33rd Eur. Conf. on Plasma Physics (2006), ECA 30I (EPS) O2.003(2006).

46) McDonald, D. C., Elbeze, D., (Takizuka, T.), et al., “Multi-machine dimensionless transport experiments,” Proc. 21st IAEA Fusion Energy Conf., EX/P3-5 (CD-ROM) (2006).

47) Medley, S. S., Andre, R., (Shinohara, K.), et al., “Investigation of collective fast ion instability-induced redistribution or loss in the National Spherical Torus Experiment,” Proc. 21st IAEA Fusion Energy Conf., EX/P6-13 (CD-ROM) (2006).

48) Miyato, N., Kishimoto, Y. and Li, J. Q., “Interplay between zonal flows/GAMs and ITG turbulence in tokamak plasmas,” Proc. 21st IAEA Fusion Energy Conf., TH/P2-11 (CD-ROM) (2006).

49) Morimoto, M., Ioki, K., Terasawa, A., et al., “Design progress of the ITER in-wall shielding,” Proc. 17th ANS Topical Meeting on Technol. of Fusion Energy (TOFE) (2006), to be published in Fusion Sci. Technol..

50) Motojima, O., Yamada, H., (Isayama, A.), et al., “Extended steady-state and high-beta regimes of net-current free heliotron plasmas in the Large Helical Device,” Proc. 21st IAEA Fusion Energy Conf., OV/2-1 (CD-ROM) (2006).

51) Takei, N., Ushigome, M., Suzuki, T., et al., “A simulation study on stable current shutdown in non-inductive reversed shear tokamak discharges,” Proc. 33rd Eur. Conf. on Plasma Physics, (CD-ROM) (2006).

52) Nagashima, Y., Itoh, K., (Hoshino, K.), et al., “Observation of nonlinear processes between coherent fluctuations and turbulent fluctuations in the edge regions of JFT-2M and CHS,” Proc. 33rd Eur. Conf. on Plasma Physics, (2006), ECA Vol.30I (EPS) P-4.135 (2006).

53) Nakamura, H. and Higashijima S., “Hydrogen isotopes removal from the vacuum vessel using discharges,” J. Vac. Sci. Jpn. 49 pp.62 (2006) (In Japanese).

54) Nakamura, H., Kobayashi, K., Yokoyama, S., et al., “Tritium release behavior from steels irradiated by high energy proton,” Proc. 17th Topical Meeting on the Technol. of Fusion Energy (2006).

55) Nakano, T., Kubo, H., Asakura, N., et al., “Radiation processes of impurities and hydrogen in detached plasmas of JT-60U,” Proc. 21st IAEA Fusion Energy Conf., EX/P4-19 (CD-ROM) (2006).

56) Nakano, T., Asakura, N., Takenaga, H., et al., “Particle control under wall saturation in long-pulse discharges in JT-60U,” Proc. 17th Inter. Conf. on Plasma-Surface Interactions in Control. Fusion Devices, 1315 (2007).

57) Neudatchin, S. V., Takizuka, T., Sakamoto, Y., et al., “ITB-events and their triggers in T-10 and JT-60U,” Proc. 21st IAEA Fusion Energy Conf., EX/P1-8 (CD-ROM) (2006).

58) Ochiai, K., Kubota, N., Taniike, A., et al., “Application of gamma rays from $D(\alpha,\gamma)^{6}Li$ and $^{19}F(\alpha,n)^{22}Na$ to alpha particle diagnostics,” Trans. Fusion Sci. Technol., 51, pp.262 (2007)

59) Oda, Y., Komurasaki, K., Takahashi, K., et al., “A multi pulse experiment of a microwave-beaming thruster,” Proc. 25th Int. Symp. on Space Tech. Sci., pp.177 (2006).

60) Oda, Y., Komurasaki, K., Takahashi, K., et al., “A plasma and shockwave observation with pulse repetition in a microwave booseted thruster,” Proc. 42nd AIAA/ASME/SAE/ASEE, (2006).

61) Ohya, K., Inai, K., (Takenaga, H.), et al., “Modeling of asymmetric redeposition distribution between inner and outer regions of the W-shaped divertor in JT-60U,” Proc. 17th Inter. Conf. on Plasma-Surface Interactions in Control. Fusion Devices, pp.78 (2007).

62) Oikawa, T., Shimada, M., Polevoi, A. R., et al., “Study on current drive capability of lower hybrid waves and neutral beam in a ITER steady state scenario,” Proc. 21st IAEA Fusion Energy Conf., IT/P1-4 (CD-ROM) (2006).

63) Okamoto, M., Takamura, S., (Kawano, Y.), et al., “Integrated view of disruption dynamics on internal electromagnetic and plasma structures in the small tokamak HYBTOK-II,” Proc. 21st IAEA Fusion Energy Conf., EX/P8-14 (CD-ROM) (2006).

64) Okuno, K., Nakajima, H., Sugimoto, M., et al., “Technology development for the construction of ITER superconducting magnet system,” Proc. 21st IAEA Fusion Energy Conf., (CD-ROM) (2006), to be published in Nucl. Fusion.

65) Oyama, N. and JT-60 Team “Enhanced ELMy H-mode performance with reduced toroidal field ripple in JT-60U,” Proc. 33rd Eur. Conf. on Plasma Physics (2006), ECA Vol.30I (EPS)O2.001 (2006).

66) Oyama, N., Isayama, A., Suzuki, T., et al., “Improved performance in long-pulse ELMy H-mode plasmas with internal transport barrier in JT-60U,” Proc. 21st IAEA Fusion Energy Conf., EX/1-3 (CD-ROM) (2006).

67) Parchamy, H., Peterson, B. J., Konoshima, S., et al., “Spatial variation of the foil parameters from in situ calibration of the JT-60U imaging bolometer foil,” Proc. 16th Int. Toki Conf. on Advanced Imaging and Plasma Diagnostics (2006), to be published in J. Plasma and Fusion Research.

68) Peterson, B. J., Konoshima, S., Kostryukov, A. Y., et al., “Research and development of imaging bolometers,” Proc. 16th Int. Toki Conf. on Advanced Imaging and Plasma Diagnostics (2006), to be published in J. Plasma and Fusion Research.

69) Peterson, B. J., Konoshima, S., Parchamy, H., et al., “Observation of divertor and core radiation in JT-60U by means of bolometric imaging,” Proc. 17th Int. Conf. Plasma Surface Interactions in Control. Fusion Device (2006), to be published J. Nucl. Mater..

70) Polevoi, A., Zvonkov, A., Oikawa, T., et al., “Assessment of current drive efficiency and synergetic effect for ECCD and LHCD in ITER steady state and hybrid scenario,” Proc. 21st IAEA Fusion Energy Conf., IT/P2-13 (CD-ROM) (2006).

71) Prater, R., La Haye , R. J. , (Isayama, A.), et al., “Prevention of the 2/1 neoclassical tearing mode in DIII-D,” Proc. 21st IAEA Fusion Energy Conf., EX/4-2 (CD-ROM) (2006).

72) Rice, J. E., Ince-Cushman, A., (Koide, Y.), et al., “Inter-machine comparison of intrinsic toroidal rotation,” Proc. 21st IAEA Fusion Energy Conf., P3-12 (CD-ROM) (2006).

73) Roberto, Z., Takahashi, Y., Nunoya, Y., et al., “The ITER Poloidal Field Conductor Insert (PFCI) test program and predictive analysis,” Proc. 2006 Appl. Supercond. Conf., (2006), to be published in IEEE Trans. ASC.

74) Sakamoto, K., Kasugai, A., Takahashi, K., et al., “Development of 170GHz gyrotron and equatorial launcher for ITER,” Proc. 21st IAEA Fusion Energy Conf., IT/2-4Rc (CD-ROM) (2006).

75) Sakamoto, K., Kasugai, A., Takahashi, K., et al., “Development of high power and long pulse 170GHz gyrotron,” Proc. 14th Workshop on Electron Cyclotron Emission and Electron Cyclotron Resonance Heating (2006).

76) Sakamoto, Y., Takenaga, H., Fujita, T., et al., “Controllability of large bootstrap current fraction plasmas in JT-60U,” Proc. 21st IAEA Fusion Energy Conf., EX/P1-10 (CD-ROM) (2006).

77) Sato, M., Isayama, A., “Evaluation of ECE spectra on the oblique propagation and application to electron temperature measurement in a reactor grade tokamak,” Proc. 14th Joint Workshop on ECE & ECH (2006).

78) Sato, M., Nishio, S., Tobita, K., et al., “Feasibility of current ramp-up by electron cyclotron wave in DEMO reactor at JAEA,” Proc. 14th Joint Workshop on ECE & ECH (2006).

79) Sato, S., Verzilov, Y., Ochiai, K., et al., “Experimental study on nuclear properties of water cooled pebble bed blanket,” Proc. 21st IAEA Fusion Energy Conf., FT/P5-13 (CD-ROM) (2006).

80) Shaaban, N., Masuda, F., (Sato, S.), et al., “A new developed interface for CAD/MCNP data conversion,” Proc. 14th Inter. Conf. on Nucl. Eng., (CD-ROM) (2006).

81) Shikama, T., Toh, K., (Yamauchi, M.), et al., “Detection of 14-MeV neutrons by optical system with radioluminescence material and optical fiber,” Proc. 18th Inter. Conf. on Optical Fiber Sensors, (CD-ROM) (2006).

82) Shimada, M., Sugihara, M., (Kawano, Y.), et al., “Disruption scenarios, their mitigation and operation window in ITER,” Proc. 21st IAEA Fusion Energy Conf., IT/P1-19 (CD-ROM) (2006).

83) Shinohara, K., Sakurai, S., Ishikawa, M., et al., “Ferritic insertion for reduction of toroidal magnetic field ripple on JT-60U,” Proc. 21st IAEA Fusion Energy Conf., FT/P5-32 (CD-ROM) (2006).

84) Suzuki, T., Ide, S., Fujita, T., et al., “Off-axis current drive and current profile control in JT-60U,” Proc. 21st IAEA Fusion Energy Conf., EX/6-4 (CD-ROM) (2006).

85) Takahashi, K., Kobayashi, M., Kasugai, A., et al., “Recent progress on design and development of the ITER equatorial EC launcher,” Proc. 14th Workshop on Electron Cyclotron Emission and Electron Cyclotron Resonance Heating (2006).

86) Takahashi, Y., Yoshida, K., Nabara, K., et al., “Stability and quench analysis of toroidal field coils for ITER,” Proc. 2006 Appl. Supercond. Conf. (2006), to be published in IEEE Trans. ASC.

87) Takase, Y., Ide, S., Kamada, Y., et al., “Evolution of bootstrap-sustained discharge in JT-60U,” Proc.21st IAEA Fusion Energy Conf., EX/1-4 (CD-ROM) (2006).

88) Takenaga, H. and the JT-60 team “Overview of JT-60U results for development of steady-state advanced tokamak scenario,” Proc. 21st IAEA Fusion Energy Conf., OV/1-2 (CD-ROM) (2006).

89) Takenaga, H., Oyama, N., Urano, H., et al., “Impacts of particle fuelling on confinement and pedestal parameter in JT-60U,” Proc. 33rd Eur. Conf. on Plasma Physics (2006), ECA Vol.30I (EPS) P-4.112 (2006).

90) Tobita, K., Nishio, S., Sato, M., et al., “Concept of low aspect ratio demo reactor, SlimCS,” Proc. 21st IAEA Fusion Energy Conf., FT/P5-22 (CD-ROM) (2006).

91) Tsuchiya, K., Hoshino, T., Kawamura, H., et al., “Development of advance tritium breeders and neutron multipliers for DEMO solid breeder blankets,” Proc. 21st IAEA Fusion Energy Conf., FT/P5-10 (CD-ROM) (2006).

92) Urano, H., Takizuka, T., Kamada, Y., et al., “Characterization of H-mode pedestal width based on hydrogen and deuterium discharges in JT-60U,” Proc. 33rd Eur. Conf. on Plasma Physics (2006), ECA Vol.30I (EPS) P-4.111 (2006).

93) Utin, Yu., Alekseev, A., Ioki, K., et al., “Design progress of the ITER VV sectors and port structures,” Proc. 24th Symp. on Fusion Technol. (2006), to be published in Fusion Eng. Des..

94) Vlad, G., Briguglio, S., (Shinohara, K.), et al., “Particle simulation analysis of energetic-particle and Alfven-mode dynamics in JT-60U discharges,” Proc. 21st IAEA Fusion Energy Conf., TH/P6-4 (2006) (CD-ROM).

95) Wesley, J. C., Hyatt, A. W., (Kawano, Y.), et al., “Disruption characterization and database activities for ITER,” Proc. 21st IAEA Fusion Energy Conf., IT/P1-21 (CD-ROM) (2006).

96) Yamada, H., Takenaga, H., .Suzuki, T., et al., “Density limit in discharges with high internal inductance on JT-60U,” Proc. 21st IAEA Fusion Energy Conf., EX/P8-8 (CD-ROM) (2006).

97) Yamaguchi, T., Kawano, Y., Kusama, Y., “Sensitivity study for the optimization of the viewing chord arrangement of the ITER poloidal polarimeter,” Proc. 16th Inter. Toki Conf., to be published in Plas. Fusion Res..

98) Yamamoto, Y. , Yamamoto, Y., (Yamanishi, T.), et al., “Fundamental study on purity control of the liquid metal blanket using solid electrolyte,” Proc. 17th Topical Meeting on the Technol. of Fusion Energy (2006).

99) Yoshida, K.,Takahashi, Y., Jong, C., et al., “Updating the design of the poloidal field coils for the ITER magnet system,” Proc. 24th Symp. on Fusion Technol. (2006), to be published in Fusion Eng. Des..

100) Yoshida, M., Koide, Y., Takenaga, H., et al., “Driving mechanism of toroidal rotation and momentum transport in JT-60U,” Proc. 21st IAEA Fusion Energy Conf., EX/P3-22 (CD-ROM) (2006).

101) Yoshida, M., Koide, Y., Takenaga, H., et al., “Investigation of toroidal rotation as a result of reduction of toroidal magnetic field ripple by installing ferritic steel in JT-60U,” Proc. 33rd Eur. Conf. on Plasma Physics (2006), ECA Vol.30I (EPS) P-4.123 (2006).

102) Zohm, H., Hayashi, (Isayama. A.), et al., “The physics base for NTM stabilisation by ECCD in ITER,” Proc. 14th Joint Workshop on Electron Cyclotron Emission and Electron Cyclotron Resonance Heating, 334 (2006).

A.1.4 List of other papers

1) Higuchi, M., “Codes and standards in my life,” Japan Society of Maintenogy, **5**, 4 (2006).

2) Imai, T., Kasugai, A., Higaki, H., et al., “Prospect for technologies making fusion reactor attractive,” The 2007 Annual Meeting Record I.E.E. Japan (2007).

3) Kasugai, A., Takahashi, K., Kajiwara, K., et al., “Present status of gyrotron development for ITER and prospect of advanced gyrotron for fusion,” The 2007 Annual Meeting Record I.E.E. Japan (2007).

4) Kasugai, A., Takahashi, K., Kobayashi, N., et al., “Operation with high power, long pulse and high efficiecny of 170GHz gyrotron for ITER,” Inst. Elec. Info.Comm. Engineers Techinical Report (2006).

5) Kawamura, H., Sawai, Y., Tsuchiya, K., “Materials for fusion reactor,” Eco-Material Handbook, 647-648 (2007) (in Japanese).

6) Kawano, K., Hamada, K., Okuno K., et al., “Development of a vacuum leak test method for large-scale superconducting magnet test facilities,” J. Cryo. Soc. Jpn., **41**, 105 (2006) (in Japanese).

7) Kimura, H., Inutake, M., Kikuchi, M., et al., “Progress in JT-60 joint research,” J. Plasma Fusion Res., **83**, 81 (2007) (in Japanese).

8) Mori, M., “Information on ITER project (1),” J. Plasma Fusion Res., **83**, 1 (2006).

9) Maekawa, T., Umetsu, T., (Sato, S.), et al., “14MeV neutron irradiation experiment for low activation concrete,” Cement & Concrete, **719**, 26 (2007) (in Japanese).

10) Mizuguchi, N., Ozeki, T., “Special Topic Article, Edge Localized Mode(ELM), 5. ELM from Viewpoint of MHD Analysis,” J. Plasma Fusion Res., **82**, pp.590 (2006) (in Japanese).

11) Nakahira, M., “Comprehending the structute of a vacuum vessel and in-vessel components of fusion machines 1. Comprehending the vacuum vessel structure,” J. Plasma Fusion Res., **82**, 9, pp.599 (2006) (in Japanese).

12) Oda, Y., Komurasaki, K., Takahashi, K., et al., “Production of microwave plasma by millimeter wave and its application to rocket propulsion,” IEEJ Trans. FM, **126**, pp.810 (2006).

13) Okuno, K., “How is ITER going forward,” Superconductivity Web21 (http://www.istec.or.jp/), Sep. 22 (2006) (in Japanese).

14) Okuno, K., “Recent progress in ITER and advanced technologies in large-scale superconducting magnet,” National Convention Record I.E.E. Japan, [5]-S7(3) (2007) (in Japanese).

15) Okuno, K., Koizumi, N., Hamada, K., et al., “Superconducting magnet technologies for magnetic confinement nuclear fusion reactor,” J. Plasma Fusion Res., **83**, pp.44 (2006) (in Japanese).

16) Sato, S., Nishitani, T., “A study on variance reduction of Monte Carlo calculation with weight window generated by density reduction method,” Nihon-Genshiryoku-Gakkai Shi (J. Ato. Energy Soc. Jpn.), **6**, 5 (2007) (in Japanese).

17) Sato, S., Verzilov, Y., Ochiai, K., et al., “Progress of the neutronics study on the ITER test blanket,” J. Plasma Fusion Res., **82**, pp.306 (2006) (in Japanese).

18) Shimamoto, S., Takahashi, Y., Okuno, K., “ITER' International Thermonuclear Experimental Reactor -from the Engineering Design Activity to the Construction Phase-,” J. Cryo. Soc. Jpn., **41**, pp.542 (2006) (in Japanese).

19) Suzuki. S., Akiba. M., Saito. M., “Comprehending the blanket structure,” J. Plasma Fusion Res., **82**, pp.768 (2006) (in Japanese).

20) Suzuki. S., Akiba. M., Saito. M., “Comprehending the divertor structure,” J. Plasma Fusion Res., **82**, pp.699 (2006) (in Japanese).

21) Takahashi, Y., Okuno, K., “International Thermonuclear Experimental Reactor (ITER) status,” J. Cryo. Association Jpn., **1**, 40 (2006) (in Japanese).

22) Tsuchiya, K., Kawamura, H., Mishima, Y., et al., “Development of beryllides as advanced neutron multipliers for fusion blankets,” J. Plasma Fusion Res., **83**, 3, pp.207 (2007) (in Japanese).

23) Yamada, H., Tsuchiya, K., “An examination into weldability of irradiated material by a laser welding method for repair of ITER blanket,” FAPIG, **173**, pp.16 (2006) (in Japanese).

A.2 Organization of Fusion Research and Development Directorate

- Director General
  - Research and Development Co-ordination and Promotion Office
  - ITER Project Promotion Group
  - Broader Approach Promotion Group
  - Research Coordination Group
  - Division of Advanced Plasma Research
    - JT-60 Advanced Program Group
    - Collaborative Research Group
    - Tokamak Analysis Group
    - Tokamak Experimental Group
    - Plasma Theory & Simulation Group
    - Tokamak Diagnostics Grooup
  - Division of Tokamak System Technology
    - Tokamak Control Group
    - Tokamak Device Group
    - RF Heating Group
    - NBI Heating Group
  - Division of Fusion Energy Technology
    - Blanket Technology Group
    - Plasma Heating Technology Group
    - Tritium Technology Group
    - Fusion Structural Materials Development Group
    - IFMIF Development Group
    - Fusion Neutronics Group
    - Blanket Irradiation and Analysis Group
  - Division of ITER Project
    - ITER Project Management Group
    - ITER International Coordination Group
    - ITER Plant System Group
    - ITER Tokamak Device Group
    - ITER Diagnostic Group
    - ITER Superconducting Magnet Technology Group

For more information on JAEA organization, please see the following URL:
http://www.naka.jaea.go.jp/english/link/sosiki-aisatsu/sosiki.html

A.3 Personnel Data

A.3.1 Scientific Staff in Fusion Research and Development Directorate of JAEA

Fusion Research and Development Directorate

TSUNEMATSU Toshihide	(Director General)
SEKI Shogo	(Deputy Director General)
SHIMOMURA Yasuo	(Scientific Consultant)
MATSUI Hideki	(Invited Researcher)
KOHYAMA Akira	(Invited Researcher)
IDA Katsumi	(Invited Researcher)
KISHIMOTO Yasuaki	(Invited Researcher)

Research and Development Co-ordination and Promotion Office

NINOMIYA Hiromasa	(General Manager)	
GUNJI Masato	HAGA Junji	KATOGI Takeshi
KAWASAKI Minoru	KIMURA Shoko	KUROSAWA Hiroshi
MATSUMOTO Hiroyuki	NEMOTO Tetsuo	OHNAWA Tetsuya
SOGA Yoriko	TERAKADO Yuichi	YOSHINARI Shuji

ITER Project Promotion Group

OKUMURA Yoshikazu (Group Leader)

DOI Kenshin	EJIRI Shintaro	MATSUMOTO Hiroshi
NAKAMURA Kazuyuki	OGAWA Toshihide	

Fusion Research Coordination Group

USHIGUSA Kenkichi (Group Leader)

ISEI Nobuaki	OOHARA Hiroshi

Broader Approach Promotion Group

Shigeru O'hira (Group Leader)

Hidetoshi Yoshida	Mayumi Tomioka

Division of Advanced Plasma Research

KIKUCHI Mitsuru	(Unit Manager)
NAGAMI Masayuki	(Supreme Researcher)
TANI Keiji	(Senior Principal Researcher)

JT-60 Advanced Program Group

FUJITA Takaaki (Group Leader)

IDE Shunsuke	KOIDE Yoshihiko	KURITA Gen-ichi
OGURI Shigeru (*5)	OIKAWA Akira	SAKAMOTO Yoshiteru

SHIINA Tomio SUKEGAWA Atsuhiko YAMAZAKI Takeshi (*5)

JT-60SA Design Integration Group (from Oct. 1, 2006.)

MATSUKAWA MAKOTO (Group Leader)
YOSHIDA Kiyoshi (Deputy Group Leader)
TAMAI Hiroshi SAKURAI Shinji TSUCHIYA Katsuhiko
HIGASHIJIMA Satoru TAKECHI Manabu KIZU Kaname
SHIBAMA Yusuke

Collaborative Research Group

KIMURA Haruyuki (Group Leader)
HOSHINO Katsumichi KONOSHIMA Shigeru SHINOHARA Kouji

Tokamak Analysis Group

OZEKI Takahisa (Group Leader)
AIBA Nobuyuki (*21) HAMAMATSU Kiyotaka HAYASHI Nobuhiko
KIYONO Kimihiro KAMATA Isao (*23) NAITO Osamu
OHASA Kazumi OHSHIMA Takayuki SAKATA Shinya
SATAKA Masao SATO Minoru SUZUKI Mitsuhiro (*30)
TAKIZUKA Tomonori

Tokamak Experimental Group

KAMADA Yutaka (Group Leader)
ASAKURA Nobuyuki CHIBA Shinichi FUJIMOTO Kayoko (*21)
HAMANO Takashi (*18) HAYASHI Toshimitsu (*16) HATAE Takaki
HOSHINO Katsumichi IDE Shunsuke INOUE Akira (*18)
ISAYAMA Akihiko KAMIYA Kensaku KASHIWA Yoshitoshi
KAWASHIMA Hisato KITAMURA Shigeru KOIDE Yoshihiko
KOJIMA Atsushi (*21) KUBO Hirotaka MATSUNAGA Go(*21)
MIYAMOTO Atsushi (*17) NAKANO Tomohide NAGAYA Susumu
OYAMA Naoyuki SAKUMA Takeshi (*18) SUNAOSHI Hidenori
SUZUKI Takahiro TAKECHI Manabu TAKENAGA Hidenobu
TSUKAHARA Yoshimitsu TSUTSUMI Kazuyoshi (*17) UEHARA Kazuya
URANO Hajime YOSHIDA Maiko (*21)

Plasma Theory & Simulation Group

KISHIMOTO Yasuaki (Group Leader, till Oct. 31)
TOKUDA Shinji (Group Leader, from Nov. 1)
IDOMURA Yasuhiro ISHII Yasutomo KAGEI Yasuhiro
MATSUMOTO Taro MIYATO Naoaki SUGAHARA Akihiro (*23)
TUDA Takashi

Fusion Reactor Design Group

TOBITA Kenji (Group Leader)

NAKAMURA Yukiharu	NISHIO Satoshi	SATO Masayasu

Division of Tokamak System Technology

HOSOGANE Nobuyuki	(Unit Manager)
YAMAMOTO Takumi	(Senior Principal Researcher)
MIYA Naoyuki	(Senior Principal Researcher)

Tokamak Control Group

KURIHARA Kenichi (Group Leader)

AKASAKA Hiromi	HOSOYAMA Hiromi (*6)	KAWAMATA Youichi
MATSUKAWA Tatsuya (*17)	OHMORI Yoshikazu	OKANO Jun
SATO Tomoki (*30)	SEIMIYA Munetaka	SHIBATA Kazuyuki (*18)
SHIMADA Katsuhiro	SUEOKA Michiharu	TERAKADO Hiroyuki (*5)
TERAKADO Tsunehisa	TOTSUKA Toshiyuki	WADA Kazuhiko (*18)

Tokamak Device Group

SAKASAI Akira (Group Leader)

ARAI Takashi	HAGA Saburo(*17)	HAYASHI Takao
HONDA Masao	ICHIGE Hisashi	ISHIGE Youichi (*18)
KAMINAGA Atsushi	KIZU Kaname	MASAKI Kei
MATSUZAWA Yukihiro (*17)	MIYO Yasuhiko	NISHIYAMA Tomokazu
NOBUTA Yuji (*21)	SASAJIMA Tadayuki	SASAKI Shunichi
SHIBAMA Yusuke	SUZUKI Yutaka(*14)	TAKAHASHI Ryukichi(*2)
YAGISAWA Hiroshi(*2)	YAGYU Jun-ichi	YAMAMOTO Masahiro

RF Heating Group

FUJII Tsuneyuki (Group Leader)

HIRANAI Shinichi	HASEGAWA Koichi	IGARASHI Koichi (*17)
ISHI Kazuhiro(*18)	MORIYAMA Shinichi	SATO Fumiaki(*17)
SAWAHATA Masayuki	SEKI Masami	SHIMONO Mitsugu
SUZUKI Sadaaki	TERAKADO Masayuki	WADA Kenji (*17)
YOKOKURA Kenji		

NBI Heating Group

IKEDA Yoshitaka (Group Leader)

AKINO Noboru	EBISAWA Noboru	GRISHAM Larry(*22)
HANADA Masaya	HONDA Atsushi	KAWAI Mikito
KAZAWA Minoru	KIKUCHI Katsumi(*18)	KOMATA Masao
MOGAKI Kazuhiko	NOTO Katsuya(*17)	OKANO Fuminori
OSHIMA Katsumi(*17)	TAKENOUCHI Tadashi (*28)	TANAI Yutaka(*18)
USUI Katsutomi		

Division of Fusion Energy Technology

TAKATSU Hideyuki	(Unit Manager)
NISHITANI Takeo	(Senior Principal Researcher)

Blanket Technology Group

AKIBA Masato (Group Leader)

ENOEDA Mikio	EZATO Koichiro	HATANO Toshihisa
HIROSE Takanori	HOMMA Takashi	MOHRI Kensuke (*8)
NISHI Hiroshi	NOMOTO Yasunobu (*8)	SUZUKI Satoshi
TANIGAWA Hisashi	TANZAWA Sadamitsu	TSURU Daigo
YOKOYAMA Kenji		

Plasma Heating Group

SAKAMOTO Keishi (Group Leader)

DAIRAKU Masayuki	IKEDA Yukiharu	INOUE Takashi
KASHIWAGI Mieko	KASUGAI Atsushi	KAJIWARA Ken (*1)
KOBAYASHI Noriyuki (*29)	KOMORI Shinji (*18)	MINAMI Ryutaro (*32)
ODA Yasuhisa (*31)	TAKAHASHI Koji	TANIGUCHI Masaki
TOBARI Naoyuki (*21)	WATANABE Kazuhiro	

Tritium Technology Group

YAMANISHI Toshihiko (Group Leader)

ARITA Tadaaki(*24)	HAYASHI Takumi	HOSHI Shuichi(*18)
ISOBE Kanetsugu	KAWAMURA Yoshinori	KOBAYASHI Kazuhiro
NAKAMURA Hirofumi	SHU Wataru	SUZUKI Takumi
YAMADA Masayuki		

Fusion Structural Materials Development Group

TAKATSU Hideyuki (Acting Group Leader)

TANIGAWA Hiroyasu (Deputy Group Leader, from July 1)

ANDO Masami	KIM Sa-woong (*12)	NAKATA Toshiya (*15)
OGIWARA Hiroyuki (*12)	SAWAHATA Atsushi (*4)	

Fusion Neutronics Group

KONNO Chikara (Group Leader)

ABE Yuichi	<u>IIDA Hiromasa</u>	KAWABE Masaru (*18)
KONDO Keitaro (*20)	KUTSUKAKE Chuzo	OCHIAI Kentaro
OKADA Kouichi (*27)	SATO Satoshi	TAKAKURA Kosuke(*17)
TANAKA Shigeru	YAMAUCHI Michinori (*29)	

IFMIF Development Group

SUGIMOTO Masayoshi (Group Leader)

CHIDA Teruo (*3)	IDA Mizuho (*5)	MAEBARA Sunao
NAKAMURA Hiroo	KUBO Takashi (*11)	MIYASHITA Makoto (*29)

Blanket Irradiation and Analysis Group

HAYASHI Kimio (Group Leader)

HOSHINO Tsuyoshi	ISHIDA Takuya (*18)	NAKAMICHI Masaru
NAMEKAWA Yoji (*18)	TSUCHIYA Kunihiko	

Division of ITER Project

YOSHINO Ryuji	(Unit Manager)
SUGIHARA Masayoshi	(Senior Principal Researcher)
KOIZUMI Koichi	ODAJIMA Kazuo

ITER Project Management Group

MORI Masahiro (Group Leader)

ITAMI Kiyoshi	SUGIE Tatsuo	YOSHIDA Hidetoshi
HIGUCHI Masahisa(*26)	TAKEI Nahoko	

ITER International Coordination Group

ANDO Toshiro (Group Leader)

HONDA Tsutomu (*29)	IDE Toshiyuki	IOKI Kimihiro (*14)
KATAOKA Yoshiyuki (*2)	MARUYAMA So	MATSUMOTO Hiroshi
MATSUMOTO Yasuhiro (*29)	MITA Yoshiyuki (*19)	MORIMOTO Masaaki (*14)
OIKAWA Toshihiro	SATO Kouichi (*30)	SHIMADA Michiya
TAKAHASHI Yoshikazu	TERASAWA Atsumi (*13)	

ITER Plant System Group

NEYATANI Yuzuru (Group Leader)

OHMORI Junji (*29)	SATO Kazuyoshi	SHIMANE Hideo (*9)
SUGIHARA Masayoshi	TAKAHASHI Hideo (*25)	YAGUCHI Eiji (*9)

ITER Tokamak Device Group

SHIBANUMA Kiyoshi (Group Leader)

KAKUDATE Satoshi	KITAMURA Kazunori (*29)	OYAKE Noriyuki (*18)
NAKAHIRA Masataka	TAKEDA Nobukazu	

ITER Diagnostics Group

KUSAMA Yoshinori (Group Leader)

HAYASHI Toshimitsu (*16)	ISHIKAWA Masao	KAJITA Shin
KASAI Satoshi	KAWANO Yasunori	KONDOH Takashi
OGAWA Hiroaki	YAMAGUCHI Taiki(*21)	

ITER Superconducting Magnet Technology Group

OKUNO Kiyoshi (Group Leader)

HAMADA Kazuya	ISONO Takaaki	KAMIKADO Takeshi (*10)
KAWANO Katsumi	KOIZUMI Norikiyo	MATSUI Kunihiro
NABARA Yoshihiro	NAKAJIMA Hideo	NIIMI Kenichiro (*7)
NUNOYA Yoshihiko	OSHIKIRI Masayuki (*18)	TAKANO Katsutoshi (*18)
TSUTSUMI Fumiaki (*30)		

Collaborating Laboratories

Tokai Research and Development Center
Nuclear Science and Engineering Directorate
Irradiation Field Materials Research Group
JITSUKAWA Shiro (Group Leader)
FUJII Kimio
OKUBO Nariaki
TANIFUJI Takaaki
WAKAI Eiichi
YAMAKI Daiju

Research Group for Corrosion Damage Mechanism
MIWA Yukio

Quantum Beam Science Directorate
Nanomaterials Synthesis Group
TAGUCHI Tomitsugu

Accelerator Group
HIROKI Seiiji

Industrial Collaboration Promotion Department
Administration Section
NEMOTO Masahiro

Oarai Research and Development Center
Advanced Nuclear System Research and Development Directorate
Innovative Technology Group,
ARA Kuniaki

Technology Development Department
Advanced Liquid Metal Technology Experiment Section
YOSHIDA Eiichi, HIRAKAWA Yasushi

*1 Fixed-Term Researcher
*2 Hitachi, Ltd.
*3 Hitachi Engineering & Services Co., Ltd.
*4 Ibaraki University
*5 JP HYTEC Co., Ltd.
*6 Japan EXpert Clone Corp.
*7 Kawasaki Heavy Industries, Ltd.
*8 Kawasaki Plant Systems, Ltd.
*9 KCS Corporation
*10 Kobe Steel, Ltd.
*11 Kumagai Gumi Co., Ltd.
*12 Kyoto University
*13 Mitsubishi Electric Corporation
*14 Mitsubishi Heavy Industries, Ltd.
*15 Muroran Institute of Technology
*16 NEC Corporation
*17 Nippon Advanced Technology Co., Ltd.
*18 Nuclear Engineering Co., Ltd.
*19 Obayashi Corporation
*20 Osaka University
*21 Post-Doctoral Fellow
*22 Princeton Plasma Physics Laboratory (USA)
*23 Research Organization for Information Science & Technology
*24 Sumitomo Heavy Industries, Ltd.
*25 Taisei Corporation
*26 The Japan Atomic Power Company
*27 Tohoku University
*28 Tomoe Shokai Co., Ltd.
*29 Toshiba Corporation
*30 Total Support Systems
*31 University of Tokyo
*32 University of Tsukuba